BUSEK 1CM MICRO RADIO-FREQUENCY ION THRUSTER EMPIRICAL PERFORMANCE DETERMINATION

THESIS

Brian D. Couch, Captain, USAF

AFIT-ENY-MS-17-M-253

DEPARTMENT OF THE AIR FORCE
AIR UNIVERSITY

AIR FORCE INSTITUTE OF TECHNOLOGY

Wright-Patterson Air Force Base, Ohio

AFIT-ENY-MS-17-M-253

BUSEK 1CM MICRO RADIO-FREQUENCY ION THRUSTER EMPIRICAL PERFORMANCE DETERMINATION

THESIS

Presented to the Faculty

Department of Aeronautics and Astronautics

Graduate School of Engineering and Management

Air Force Institute of Technology

Air University

Air Education and Training Command

In Partial Fulfillment of the Requirements for the

Degree of Master of Science in Astronautical Engineering

Brian D. Couch, BS

Captain, USAF

March 2017

AFIT-ENY-MS-17-M-253

BUSEK 1CM MICRO RADIO-FREQUENCY ION THRUSTER EMPIRICAL PERFORMANCE DETERMINATION

Brian D. Couch, BS
Captain, USAF

Commmittee Membership

Carl Hartsfield, PhD
Chair

Maj. David Liu, PhD
Member

William Hargus, PhD
Member

AFIT-ENY-MS-17-M-253

Abstract

Empirical performance quantification was attempted on a Busek 1-centimeter Radio Frequency Ion Thruster (BIT-1) to characterize thruster performance across a full range of operating conditions. Several experimental setups were attempted in order to operate the specific thruster utilized for this experiment. All troubleshooting steps are documented leading up to successful operation of the BIT-1 for a total of 15 minutes. Further testing is required to fully quantify the BIT-1 thrust profile, exact divergence angle, and efficiency. In addition, the Busek torsional thrust stand's calibration force equation was evaluated. The current calibration equation was found to overestimate applied forces. A modification was added to the thrust stand's equation enabling more precise thrust measurements for future experiments.

To all who seek to advance knowledge and understanding, whether your domain is science, philosophy, art, or any other field of discovery, by examining the wonders of creation you worship God. This work is dedicated for the glory of the God of the Bible.

Acknowledgments

I would like to express my sincere appreciation to Dr. Carl Hartsfield for his guidance and support throughout the course of this thesis effort. I would also like to thank Dr. Mike Tsay for his help in troubleshooting numerous issues with the BIT-1 thruster and setup. I would like to thank Capt. Nick Hyatt for his collaboration and teamwork in sharing the AFIT vacuum chamber. Special thanks go to Matt "Sofa" Couch, who provide immense support and encouragement and Capt. Ken Stuart who helped significantly throughout my time at AFIT. Finally, I would like to thank Mr. Jamie Smith, Mr. Josh Dewitt, Mr. Michael Ranft, and Mr. Keith Long for their laboratory assistance and incredible expertise.

Brian D. Couch

Table of Contents

Page

List of Figures

Page

List of Tables

Page

List of Symbols

Symbol	Definition
B	Magnetic field vector (Tesla)
d	Sheath Thickness
d	Electrode Separation Distance (mm)
∇	Vector Differential operator
e	Electron Charge Constant ($1.602 \cdot 10^{-19}$ C)
ϵ_o	Permittivity of Free Space Constant ($8.854 \cdot 10^{-12}$ F/m)
η_e	Electrical Efficiency
η_m	Mass Utilization Efficiency
η_T	Total Efficiency
E	Electric field vector (V/M)
E_{accel}	Acceleration Grid Electric Field
E_{ave}	Average Three-dimensional Kinetic Energy
E_{screen}	Screen Grid Electric Field
F	Force of Thrust (N)
F	Force vector of Thrust (N)
F_{accel}	Force on Acceleration Grid (N)
F_{cal}	Calibration Force (N)
F_{screen}	Force on the Screen Grid (N)
g_0	Earth's Gravitational Acceleration Constant (9.807 m/s^2)
k	Boltzmann's Constant ($1.38065 \cdot 10^{-23}$ J/K)

I_b	Ion Beam Current (mA)
I_{sp}	Specific impulse (s)
J	Current Density (mA/m^2)
$\dot{m}$	Mass Flow Rate (kg)
m_d	Delivered Mass (kg)
m_p	Propellant Mass (kg)
μ_o	Permeability of Free Space Constant ($1.2566 \cdot 10^{-6}$ T · m/A)
M	Mass of the Particle (kg)
n_e	Electron Number Density
n_i	Ion Number Density
n_s	Number Density of Species s
N	Newton
P_0	Additional Power (w)
P_{in}	Input Power (w)
P_{jet}	Jet Power (w)
ϕ	Electric Potential
q	Particle Charge
q_s	Charge State of Species s
ρ	Plasma Charge Density (C/m^2)
sccm	Standard Cubic Centimeters per Minute
t	time (s)

T	Temperature (K)
v	Particle Velocity (m/s)
$\overline{v}$	Average Particle Speed (m/s)
v_e	Electron Velocity (m/s)
v_{ex}	Particle Exit Velocity (m/s)
v_i	Ion Velocity (m/s)
v_s	Velocity of Species s
V	Voltage
V_b	Ion Beam Voltage (volts)
V_{cal}	Calibration voltage (volts)
γ	Total Thrust Correction
Z	Charge State

BUSEK 1CM MICRO RADIO-FREQUENCY ION THRUSTER EMPIRICAL PERFORMANCE DETERMINATION

I. Introduction

Background

Electric propulsion, in general, provides small to moderate quantities of thrust with exceptionally high exhaust velocities, approaching 10^3 km/s. This combination results in high-efficiency thrusters. In the electron propulsion world, ion thrusters provide some of the lowest thrust combined with the highest exhaust velocities, translating to thrusters with the highest efficiencies, 60 to 80 percent [1:4]. The first successful space flight of ion thrusters was a pair on Space Electric Rocket Test 1 in 1964, by NASA Glenn Research Center, in which only one ion thruster worked for 34 minutes. Experimental testing continued through the 1990's, mostly through military funding. However, in 1997, the realization of commercial applications came to fruition through PanAmSat 5, the Hughes Research Laboratories' communications satellite. This satellite used an ion thruster for station keeping. Soon after, Deep Space 1 (DS1), the first launch of NASA's New Millennium Program missions, was launched in 1998 for testing advanced technologies. One of the objectives was to validate low-power ion propulsion.

This goal was accomplished through DS1's xenon ion thruster which provided primary propulsion, two-axis attitude control, and operated for 16,246 hours [2:1].

In combination with high efficiency and exhaust velocity, an ion thruster's range of specific impulse–2500 to 3600 seconds–is the premier among the electric propulsion thrusters [1:5]. These operational parameters are ideally suited for a broad range of extended sustained thrust missions. Orbit transition, station-keeping, and interplanetary travel are a few of the currently active missions for which ion thrusters are being utilized. The variety of commercial and defense applications along with the continued research of organizations such as NASA establishes the importance of ion thrusters in future space missions [3:2].

Motivation

Until the early 2000s, larger sized gas and electric space propulsion dominated research areas. Micro, nano, and cube satellites have become increasingly popular as they offer a significant reduction in cost, improve reliability, and have a broad range of utility. With the development of these small satellites, miniaturization of thrusters became an area of focus and a critical need. However, miniaturization of current electric propulsion designs came with limitations. The size of the power processing unit, the space-charge effect (particles of like charge repelling each other), and vacuum breakdown limit for electrostatic fields are a few of the limiting factors for scaling down ion thrusters [4:24;1:200].

NASA/JPL funded the Busek 1CM Radio-Frequency Ion Thruster (BIT-1) as a thruster for the Laser Interferometer Space Antenna (LISA) mission. The LISA mission

employs a triangular constellation of three spacecraft, uniformly separated, designed to study gravitational waves. These three spacecraft require unprecedented positional and pointing accuracy to maintain their dual five million kilometer separation. This requirement necessitated the development of a sub-30 μN micro-thruster capable of precision control [5:2]. The radio-frequency (RF) ion thruster design was selected for development due to the simplicity and ability to scale down the physical dimensions.

Unlike standard ion thrusters, RF ion thrusters generate plasma by energizing a helical coil at a low megaHertz frequency in a dielectric chamber. This helical coil also produces an electromagnetic field which contains the plasma. Due to this design, an external magnetic field and internal cathode are not required, which in turn, allows the thruster to be scaled down significantly. Through extensive experimental work by Busek, an optimal 1 cm thruster was developed to balance size, performance, and efficiency [5:3]. The overall combination of size, high efficiency, and small precise thrust capabilities cause RF thrusters to be particularly desirable within both the DOD and commercial space missions.

Scope

Busek estimated the thruster performance by measuring current and propellant flow. However, based on their prior experience with ion thruster thrust calculations being 95% accurate, they decided not to measure the thrust directly [5:5]. The objective of this research is to fully characterize the BIT-1 ion thruster at nominal operation conditions and across the flight envelope. The thrust is determined using a torsional thrust stand designed to accurately measure micro-newton forces. The specific impulse is calculated

from the thrust and propellant mass flow data. By varying thruster propellant mass flow rate, radio-frequency power, and screen voltage independently, the thrust envelope is quantified. A Faraday probe is used to produce a map of the current density which is used to determine the divergence angle of the thrust plume. Lastly, using an E-cross-B (ExB) probe, quantify the species distribution in the ion plume (singly-, doubly-, and triply-ionized xenon).

Research Objectives

The objectives of this research are to:

1. measure thrust at the nominal operating condition;
2. determine the specific impulse at the nominal operating condition;
3. determine the specific impulse across the flight envelope;
4. quantify the thrust envelope for varying thruster propellant mass flow rate, radio-frequency power, and screen voltage;
5. determine the divergence angle of the thrust plume;
6. quantify the species distribution in the ion engine plume (singly-, doubly-, and triply-ionized xenon).

II. Background

Chapter Overview

The purpose of this chapter is to review general electrostatic theory and plasma physics, and explore the types and operations of ion thrusters. Furthermore, the topics concerning fully characterizing ion thrusters, species ionization, and plasma current density are explained. Additionally, neutralizing cathodes, which are an essential component for proper thruster operation, are described. This chapter will also explore the impacts of size scaling on the performance of an ion thruster. Lastly, the previous experimental work on the ion thruster used in this experiment will be discussed.

Electrostatic Theory and Plasma Physics

A basic synopsis of electrostatic theory and plasma physics is required to understand the basics of RF ion thrusters. Electric propulsion produces thrust by accelerating charged particles to extremely high velocities, approaching 1000 km/s [1:37]. The charged particles are generated by ionizing a propellant gas, forming a mixture of positively charged ions, negatively charged electrons, and excited neutral propellant. This combination of particles is called a plasma. The plasma has sufficient electrical conductivity to be affected by magnetic and electric forces [7:125]. On average, the ratio of ion to electron densities is approximately equal, a state commonly referred to as quasi-neutral. Effectively, the plasma, as a whole, is neutrally charged. This condition holds true throughout the ionized gas and can be applied to the analysis of plasma

behavior, except two situations. These situations are along the boundary of the plasma volume and the separation distance of charged particles, defined by the Debye length.

The plasma-generated electric and magnetic fields found in electric propulsion systems in a vacuum follow Maxwell's equations, which are shown in Equations 1 - 4:

$$\nabla \cdot \boldsymbol{E} = \frac{\rho}{\epsilon_o} \tag{1}$$

$$\nabla \times \boldsymbol{E} = -\frac{\partial \boldsymbol{B}}{\partial t} \tag{2}$$

$$\nabla \cdot \boldsymbol{B} = 0 \tag{3}$$

$$\nabla \times \boldsymbol{B} = \mu_o \left(\boldsymbol{J} + \epsilon_o \frac{\partial \boldsymbol{E}}{\partial t} \right) \tag{4}$$

Where $\boldsymbol{E}$ and $\boldsymbol{B}$ are the electric and magnetic field vectors, respectively; ρ is the plasma charge density; ϵ_o and μ_o are the permittivity and permeability of free space constants; and $\boldsymbol{J}$ is the current density [1:38]. The plasma charge density is defined by the equation:

$$\rho = \sum_s q_s n_s = e(Zn_i - n_e) \tag{5}$$

Where q_s and n_s are the charge state and number density of species *s*; *e* is the electron charge constant; Z is the charge state; and n_i and n_e are the ions and electron number densities, respectively. Similarly, the current density is defined by the equation:

$$J = \sum_s q_s n_s \, v_s = e(Zn_i v_i - n_e v_e) \tag{6}$$

Where v_s is the velocity of species s and v_i and v_e are correspondingly the ion and electron velocities. Lastly, the electric field for ion thrusters and similar electric propulsion thrusters with static magnetic fields is defined by the equation:

$$\boldsymbol{E} = -\nabla\phi \tag{7}$$

where ϕ is the electric potential [1:39]. These equations, applied to the propellant plasma, give the foundation for assumptions and further equations for the ion thruster.

The Lorentz force equation describes the equation of motion for a charged particle in a typical electric thruster:

$$\boldsymbol{F} = q(\boldsymbol{E} + v \times \boldsymbol{B}) \tag{8}$$

Where v is charge particle velocity and $\boldsymbol{F}$ is the thrust. It is assumed ion thrusters provide thrust by using only an electric field since the other constituents provide small contributions. Therefore, Equation 8 can be rewritten as:

$$\boldsymbol{F} = q\boldsymbol{E}. \tag{9}$$

Using the initial set of equations and the assumption of thermal equilibrium, a Maxwellian distribution of particles in the plasma can be assumed. This assumption provides the average three-dimensional kinetic energy and average particle speed equations:

$$E_{ave} = \frac{3}{2}kT \tag{10}$$

$$\overline{v} = \left(\frac{2kT}{\pi m}\right)^{\frac{1}{2}} \tag{11}$$

Where k is Boltzmann's constant, T is the temperature, and m is the mass of the particle [1:45].

The last topic for basic plasma physics is sheaths. Sheaths are regions of electric potential changes and density changes which occur at the boundaries of the plasma where, as stated earlier, the quasi-neutrality breaks down. At the boundary of the plasma are the two physical interfaces where energy and particles enter and exit. As a result, understanding these sheath behaviors and formations is essential for ion thruster understanding and modeling [1:71].

The simplest but most important case of a plasma sheath is called a Child-Langmuir sheath. These are generated when the potential across the sheath is much larger than the electron temperature causing electrons to be repelled away from the plasma; essentially causing electron density to go to zero. An equation called Child-Langmuir law, originally derived independently by Child in 1911 and Langmuir in 1913, describes this sheath. Their law for a nonspecific propellant states:

$$J_{\mathrm{i}} = \frac{4\epsilon_{\mathrm{o}}}{9}\left(\frac{2\mathrm{e}}{M}\right)^{\frac{1}{2}}\left(\frac{V^{\frac{3}{2}}}{d^2}\right) \tag{12}$$

Where J_i is the current per unit area, M is the mass of the particle, V is the voltage, and d is the sheath thickness. As this equation is based off the propellant type, the equation can be conveniently written for singly-charged xenon ions as [1:81]:

$$J_i = 4.75 \times 10^{-9}\frac{V^{\frac{3}{2}}}{d^2}\ . \tag{13}$$

Ion Thruster Operation and Equations

A standard ion thruster is comprised of three main components: the plasma generator, the acceleration grids, and the neutralizing cathode. Plasma is typically generated through ionization via electron bombardment of the inert gas as it enters the thruster, which creates a mass of electrons and positively charged ions. Electrons are produced by an internal cathode typically using the propellant gas. Once formed into a plasma, ions flow through two grids. These ions are lined up by passing through the first positively charged extraction grid which aligns the ions in the proper orientation for exiting the thruster. Next, they are accelerated towards the second negatively charged acceleration grid by the electric potential between the girds. Then the ions pass through the acceleration grid and expelled at very high velocity, creating the thrust beam. Simultaneously, the neutralizing cathode, outside the thruster, is introducing electrons back into the positively charged ion cloud, thereby neutralizing the ions to atoms. An example of a simple ion thruster is shown in Figure 1.

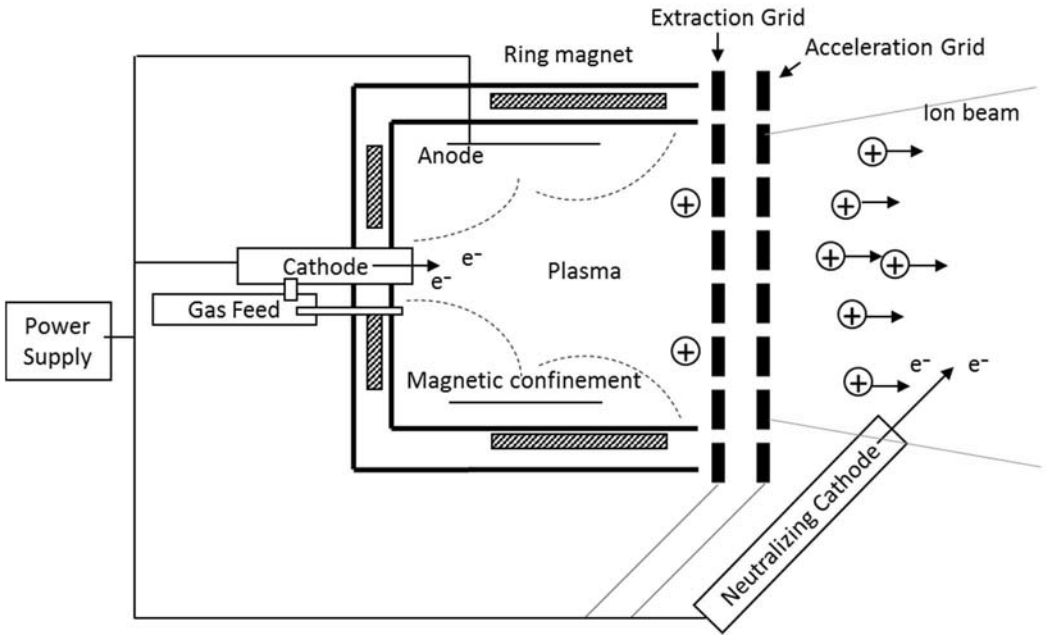

Figure 1. Illustration of Ring-Cusp Ion Thruster

An ion thruster follows the same basic principles as a chemical rocket with similar equations but specific to electrostatics. To create thrust, mass is ejected out of the spacecraft in the opposite direction of the desired velocity vector. Using the conservation of momentum, the spacecraft's change in velocity multiplied by the spacecraft's mass is equal to the ejected propellant mass multiplied by the propellant's velocity. This relationship results in the ideal rocket equation and is one of the foundational equations:

$$\Delta \mathrm{v} = \mathrm{Isp} \cdot g_0 \cdot \ln\left(\frac{\mathrm{m_d} + \mathrm{m_p}}{\mathrm{m_d}}\right) \tag{14}$$

Where Δv is the change in the spacecraft's velocity, Isp is the thruster's specific impulse, g_0 is the gravitational acceleration constant, m_d and m_p are the delivered and propellant mass respectively [1:17].

Specifically for ion thrusters, thrust is determined by the sum of the forces applied by the electrostatic force of the extraction and acceleration grids to the ions. Therefore the net thrust can be calculated using these equations:

$$F_{screen} = \frac{1}{2}\epsilon_o E_{screen}^2 \tag{15}$$

$$F_{accel} = -\frac{1}{2}\epsilon_o E_{accel}^2 \tag{16}$$

$$F = F_{screen} + F_{accel} = \frac{1}{2}\epsilon_o (E_{screen}^2 - E_{accel}^2) \tag{17}$$

Where F_{screen} and F_{accel} are the forces on the screen grid and acceleration grid respectively, and F is the thrust [1:19]. The resulting thrust is equal and opposite of electric field forces on the ions. The thrust can be further defined by time rate of change of the momentum:

$$F = \frac{d}{dt}(m_p v_{ex}) = \dot{m}_p v_{ex} \tag{18}$$

Where $\dot{m}_p$ is the propellant mass flow rate and v_{ex} is the velocity of the particles exiting the thruster. Therefore, the thrust of an ion thruster is dependent on the electrostatic forces in-between the ions, in-between the grids, and additionally on the propellant mass flow rate and the exit velocity [1:21]. In a typical thermal rocket, there would be a pressure term in this equation, but the densities are in ion thrusters are so low the pressure term can be neglected. In addition, particles which are drifting out of the thruster with thermal speeds around 100-300 m/s are ignored.

To accelerate the ions and produce thrust, the potential energy of the propellant must be converted to kinetic energy. The kinetic thrust power contained in the rocket exhaust is called jet power and is defined as:

$$P_{jet} = \frac{1}{2}\dot{m}_p v_{ex}^2 . \tag{19}$$

Using Equation 18, the jet power can be further defined as:

$$P_{jet} = \frac{T^2}{2\dot{m}_p}. \tag{20}$$

These equations show the inherent relationship between jet power, thrust, and propellant mass flow [1:22; 7:23].

Ion thrusters produce thrust by accelerating ions to high velocities by means of electrical power sources. Any other propellant exiting the thruster un-ionized will do so at a significantly reduced velocity compared with the ion exit velocity. This means the thrust can be defined directly by the ion components as:

$$F = \dot{m}_i v_i \tag{21}$$

Where $\dot{m}_i$ is the mass flow rate of the ions and v_i is the exhaust velocity of those ions. Using the conservation of energy theory, the ion exhaust velocity is defined by:

$$v_i = \sqrt{\frac{2eV_b}{M}} \tag{22}$$

Where V_b is the net voltage through the ion was accelerated (beam voltage) and M is the mass of one propellant ion. The mass flow rate of the ions is defined by:

$$\dot{m}_i = \frac{I_b M}{e} \tag{23}$$

Where I_b is the ion beam current [1:22]. Substituting Equations 22 and 23, into Equation 21 results in a final thrust equation:

$$F = \sqrt{\frac{2M}{e}}\, I_b \sqrt{V_b}\,. \tag{24}$$

This is the most common thrust equation, in use and appearance, for ion thrusters and can be further simplified by the propellant type. Xenon is the propellant used for this research with an atom mass of $2.18 \cdot 10^{-1}$ kg and the electron charge constant of $1.602 \cdot 10^{-19}$ C. Thus, Equation 24 can be simplified to:

$$F = 1.65\, I_b \sqrt{V_b}\ [\text{mN}] \tag{25}$$

Where I_b and V_b are in amps and volts, respectively [1:23].

The next set of equations needed to be defined are the thruster efficiencies, which includes the specific impulse. Specific impulse, or Isp, is a measure of mass utilization performance and is defined to be:

$$\text{Isp} = \frac{F}{\dot{m}_p g} = \frac{\gamma \eta_m}{g} \sqrt{\frac{2eV_b}{M}} \tag{26}$$

Where γ is the total thrust correction factor and η_m is the mass utilization efficiency [1:26]. The mass utilization efficiency is for singly charged ions, which accounts for difference in ionized vs un-ionized propellant, is given by

$$\eta_m = \frac{\dot{m}_i}{\dot{m}_p} = \frac{I_b}{e}\frac{M}{\dot{m}_p}. \tag{27}$$

The thruster's electrical efficiency is defined as the ratio of output, P_b, to total power, P_T [1:25]. This is written as

$$\eta_e = \frac{P_b}{P_T} = \frac{I_b V_b}{I_b V_b + P_0} \tag{28}$$

Where P_0 is the additional power required to create the thrust beam which includes the power for ionization, gird currents, and power to the cathode. Lastly, the total thruster efficiency is

$$\eta_T = \frac{P_{jet}}{P_{in}} = \frac{F^2}{2\dot{m}_p P_{in}} \tag{29}$$

Where P_{in} is the input power into the thruster [1:28].

The last section required for understanding ion thruster operation is the function of ion grids. As discussed before, conventional ion thrusters have two grids, the extraction grid and the acceleration grid. These two grids make up the acceleration assembly–often called ion optics–and are designed to extract the ions from the plasma, align the ions, and then accelerate them. Therefore the overall performance of the ion thruster is significantly affected by the grid design, with trade-offs between lifetime, performance, and size [1:189].

The lifetime of the grids and, correspondingly, the ion thruster is highly dependent on the grid transparency. Transparency is a grid's measured ability to allow ions to pass through the grid rather than impinging of the ion flow. This flow is required to function through the range of plasma ion densities and over the full throttle range of the thruster. Thus, the design of the ion optics is driven to high ion transparency,

resulting in a large grid hole in the extraction grid and smaller holes in the acceleration grid. This size relationship directly correlates to the optical focusing of the ions resulting in the beam divergence, discussed later. The figure below illustrates a simplified thruster design and the transition from the plasma cloud to the ion beam.

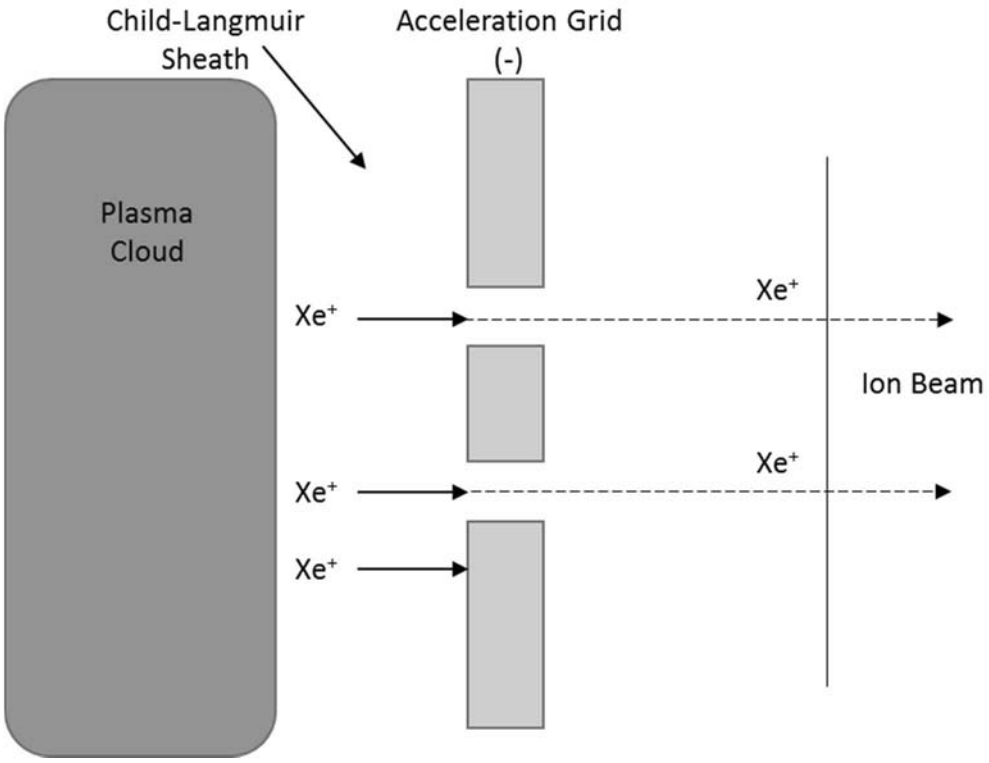

Figure 2. Simplified 1-D View of Interaction Plasma and an Ion Grid

As seen in Figure 2, a xenon ion (Xe^+) misses the aperture and is accelerated into the grid, causing erosion of the grid. This highlights the requirement of the extraction grid to align the ions and prevent grid erosion. Even with an extraction grid, the ions will still impact the extraction grid. However, due to the positive charge applied to the grid, the postively charged ion's impact energy will be reduced because of repelling forces

[1:191]. Ideally, the aperture sizes of the two-grid design will ensure beam focusing while minimizing erosion, as shown below in Figure 3.

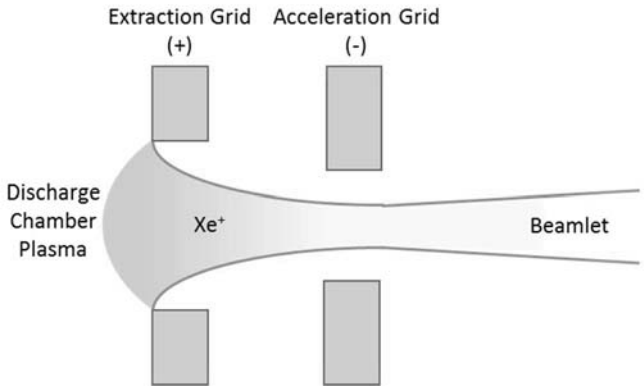

Figure 3. Beam Focusing and Beamlet Formation for Two-Grid Design

An additional consideration for grid lifetime is the addition of a third, neutrally charged deceleration grid, positioned after the acceleration grid. After the positively charged ions leave the thruster and before the full ion beam is formed, radial electric forces, such as like-charges repelling, can push ions into the gaps between the beamlets. From there, the ions are attracted to the negatively charged acceleration grid. Figure 4 shows a simplified cross-section of ion beamlets.

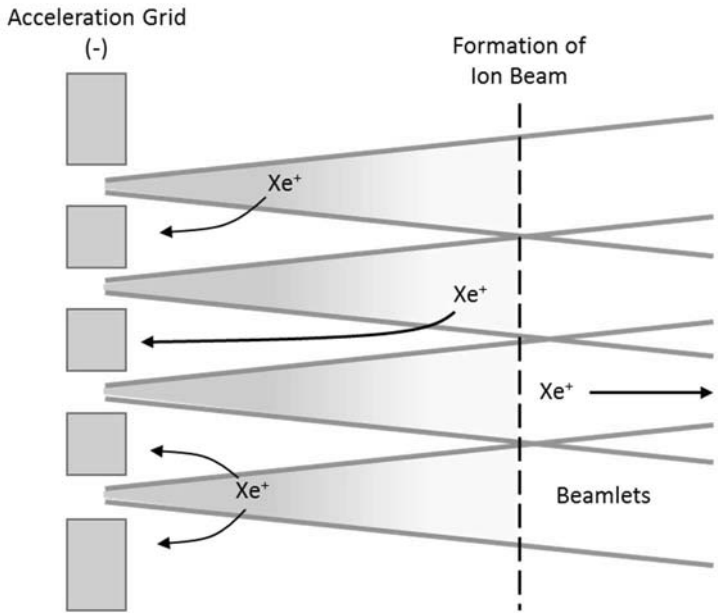

Figure 4. Xenon Beamlets with Escaping Ions

As seen in Figure 4, positive xenon ions are occasionally forced out of the beamlets. These positively-charged free-floating ions are then attracted back to the negatively charged acceleration grid. Over the lifetime, typically on the order of ten thousand hours, the erosion caused by the backflow of positive ions can completely destroy the structural integrity of the acceleration grid. As the erosion builds, the grid's effectiveness at beam focusing and acceleration is reduced. Figure 5 illustrates the two ion optic designs.

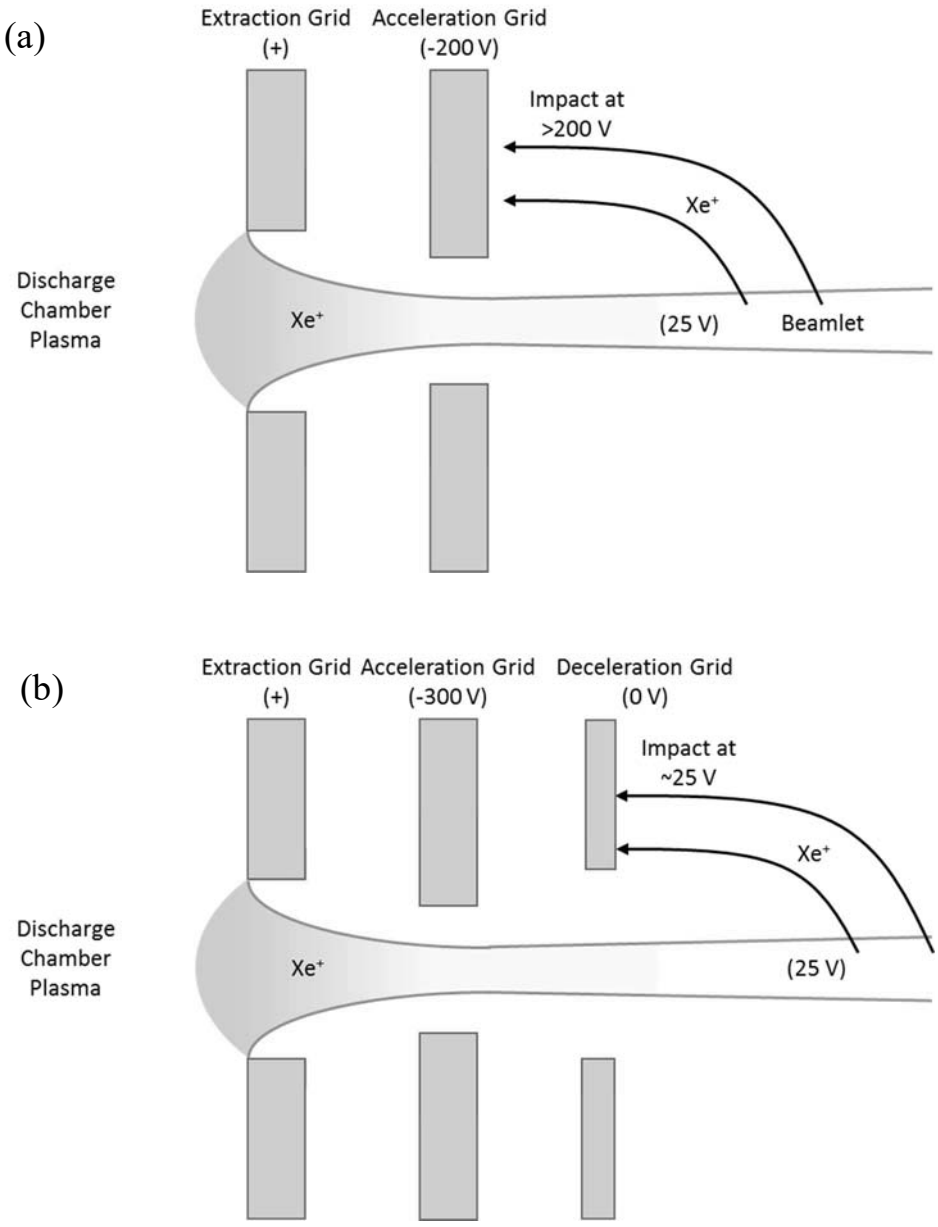

Figure 5. Grid Cross-Section Comparing Two-Grid and Three-Grid Ion Optics Designs

The neutral deceleration grid design shown in Figure 5 (b) inhibits any escaping ions from eroding the acceleration grid while reducing their impact energy. However, the addition of the deceleration grid slightly reduces the velocity of the ions and therefore

reduces the thrust. Overall, ion optics are a core component of an ion thruster, extracting the ions from the plasma, aligning them to prevent erosion, and then accelerating them to produce thrust.

Ion Thruster Types

Ions used to produce thrust are created by means of plasma generators. For ion thrusters, there are three widely used types of plasma generators, direct current (DC) electron discharge, RF discharge, and microwave discharge [1:91]. The BIT-1 thruster uses RF discharge to generate plasma. To understand how RF discharge plasma generation differs from other designs, DC and microwave discharge will be briefly discussed.

Figure 1 illustrates a classic DC electron discharge plasma generator used in an ion thruster. DC electron discharge plasma generators employ an anode potential discharge chamber along with a hollow cathode [1:100]. During operation, propellant gas is injected into the chamber along with a small amount of propellant into the hollow cathode. In the cathode, electrons are extracted from the propellant and are then injected into the chamber. These electrons bombard the neutral propellant in the chamber. In simplest terms, high energy electrons bounce around the chamber and impact a neutral propellant atom which releases an electron from the atom [8:71]. This process is called electron collision ionization. Once ionized, the quasi-neutral plasma is confined by a magnetic field surrounding the chamber. The magnetic field is produced by several ring magnets which surround the chamber. In collaboration with anode-cathode voltage differential, the magnetic field is optimized to maximize ionization efficiency and ion

extraction while minimizing the production of doubly-charged ions [7:131]. The charge state of ions is discussed in the next section. Essentially, the magnetic field encourages ionization to occur by keeping the density of neutral and electron particles high, while forcing ionized particles toward the grids. Last, similar to other designs, ions in the plasma flow toward the ion optics which extract and accelerate them to form the thrust beam.

Microwave discharge and RF designs are cathodeless concepts [7:132]. These designs do not require an internal cathode producing electrons to create the plasma state inside the chamber. Figure 6 is a simplified schematic of an ion thruster using microwave discharge.

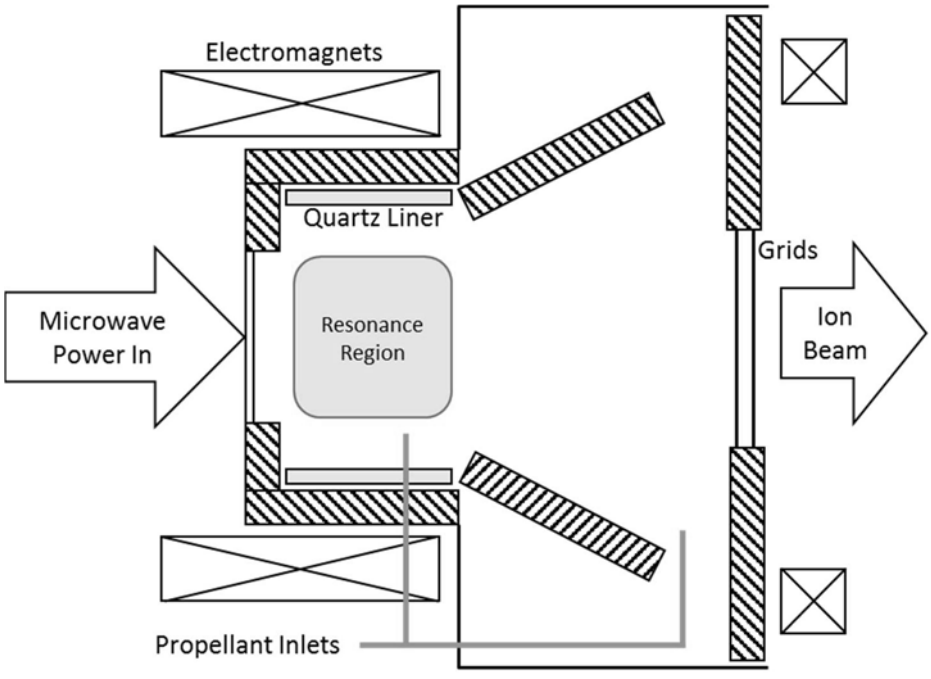

Figure 6. Illustration of Ion Thruster using Microwave Discharge

First, propellant is injected into the resonance region in front of a microwave generator. In the presence of particle collisions, microwave energy combined with a strong magnetic field will cause resonant heating of the electrons [1:158]. This effect produces the plasma. The plasma is then guided towards the grids, contained along the magnetic field lines. Ions are then extracted, accelerated, and allowed to diverge which, in total, generates the ion beam. A neutralizing cathode, not shown in Figure 6, is still required to neutralize the ion beam. This design removes some of the difficulties in plasma production by producing plasma without solid electrodes, thermionic emissions, or a large potential gap [9:1022]. However, the electromagnetic wave can only affect the plasma under certain conditions. For example, the microwave radiation can be reflected if the plasma density is low. This low density can cause issues for initial plasma generation [1:159].

The remaining plasma generation method is RF discharge ionization and results in one of the simplest ion thruster designs. Typical RF ion thrusters are designed with an axisymmetric cylindrical or conical discharge chamber made of dielectric material. The chamber is wrapped by a helical RF antenna coil. This coil is energized at a low megahertz radio frequency and is used to generate and sustain the plasma inside the chamber, known as the inductively-coupled plasma (ICP) discharge region [10:15]. For this design, an applied magnetic field is not required to produce the plasma, although one can be used to improve the ion discharge performance [1:148]. Figure 7 presents an example cross-section of a two-grid ion thruster.

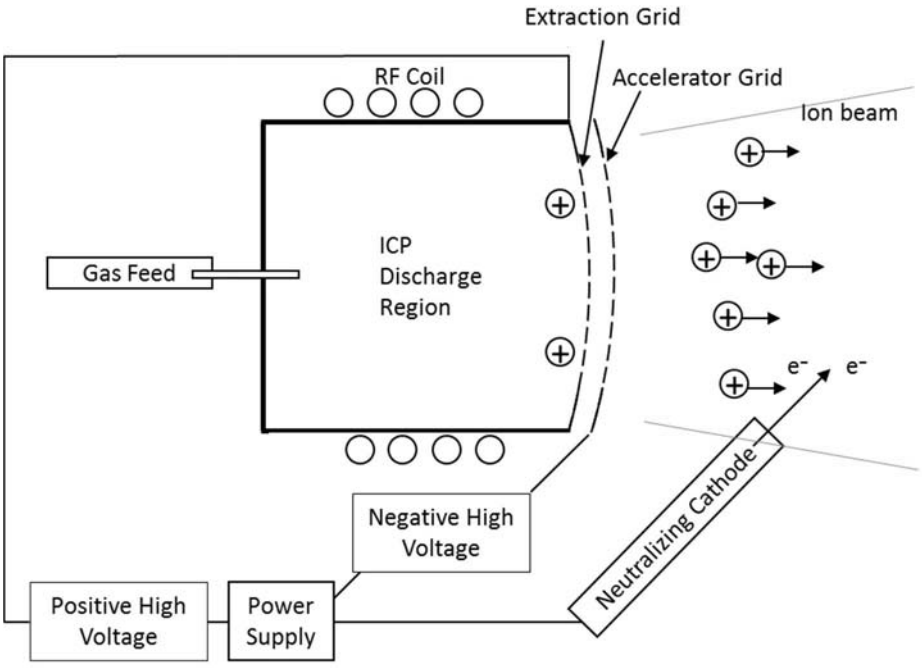

Figure 7. Illustration of Ion Thruster using Radio Frequency Discharge

To start an RF ion thruster, electrons, also called seed electrons, are first produced by the neutralizing cathode. Next, the electrons are drawn into the chamber by activating the acceleration grid's positive charge. Propellant flow can begin once the chamber reaches the required electron density and the negative extraction grid is turned on. Then, activating the RF coil produces an oscillating electromagnetic field which accelerates the electrons azimuthally in the chamber. Electrons then collide with the propellant, ionizing it. This process generates the plasma. Similar to other designs, the ions are extracted and accelerated by the ion optics, producing the thrust beam [10:16]. Finally, the thrust beam is neutralized by the external cathode. Due to the plasma generation design, an external magnetic structure and internal cathode are not required. This combined design aspect

reduces the size and mass of the thruster, which in turn allows for miniaturization [10:17].

Ion thrusters can use a variety of propellant types, including mercury, krypton, and argon. The most common use in RF ion thrusters is the noble gas xenon. Xenon has favorable characteristics including high atomic weight (131.3 g/mole) and low first ionization energy (12.1 eV). The mass of the xenon helps prevent ions from being magnetized while inside magnetic fields. Therefore the ions can be electrostatically accelerated without being affected by the RF generated magnetic fields. The low ionization energy subsidizes efficient energy usage by reducing the power required to ionize the gas. Lastly, since xenon is a noble gas, it is chemically inert, permitting easy handling. Overall, these characteristics make xenon the primary propellant for ion thrusters [10:17].

Species Ionization

During the process of ionization, electrons collide with neutral particles, releasing an electron from the particle to create an ion. This process can also happen to ions if electrons are still present within the ion. When an electron with sufficient energy collides with an ion, a second electron can be released, creating doubly ionized particle. Likewise, a triply ionized particle can be formed. These charge states of ions are called ion species. With each increase of ion species, more energy is required. The thrust efficiency directly relates to the ratio of doubly- and triply-charged ions to singly charged ions [11:1]. In addition, as more of the higher ion species are created the thrust is lowered and the Isp

increases. Overall, the velocity of the doubly-charged ion faster than the singly-charged ion velocity but the additional power required to ionize reduces the thruster efficiency.

Species fraction is assessed by using a device called an ExB probe. From the species fraction, thruster efficiencies can be determined. Placed inside the ion beam of the thruster, the ExB probe is designed to determine the species distribution of ions between single, double, or triple ionization levels. An ExB probe is one application of the Lorentz force, Equation 8 on page 7. This equation indicates a particle will be forced in a direction perpendicular to both its velocity and an applied magnetic field. However, using an electric field, the particle can be redirected to its original path. Therefore, the magnetic and electric field can be configured to force particles with the desired characteristics to remain on their undeflected, original path while deflecting all others [11:2]. Figure 8 illustrates a cross-section of a standard ExB probe.

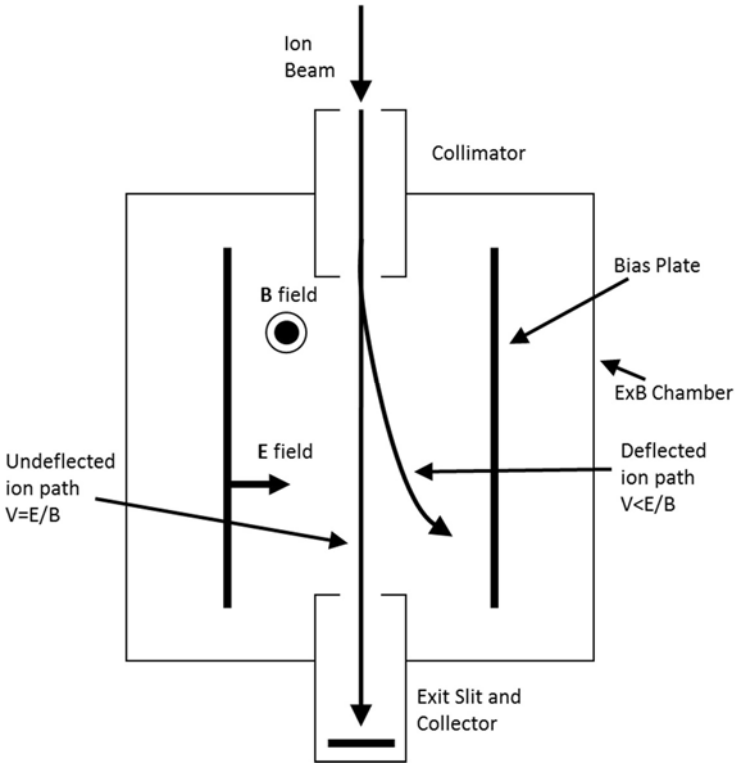

Figure 8. Generic Cross-section of an ExB Probe

The main components of an ExB probe are the collimator, magnets, electrodes, and the collector. The collimator focuses the incoming ions. An electric field is created by applying a bias voltage to the two electrodes. Finally, the collector measures the current of undeflected ions. To pass through undeflected, the net force on the ion must be approximately zero. Setting the force equal to zero, in equation 8, and solving for the Electric field yields:

$$\boldsymbol{E} = -v \times \boldsymbol{B} \tag{30}$$

Ion velocity is determined by Equation 22 and is based on ion beam voltage and charge state. Thus, when the voltage is swept on the electric field and the other variables remain

constant, only ions with a particular charge state will allow to pass undeflected. This process identifies the species ionization distribution.

Plasma Current Density

A constituent of fully characterizing an ion thruster's capabilities includes understanding the impact of plasma inside the ion beam. There are several instruments designed for plasma data collection, including Faraday probes, single and double Langmuir probes, emissive probes, and retarding potential analyzers [12:55]. The Faraday probe was used in this research due to its availability and ease of use with the vacuum chamber translational stand capability. This instrument is used to record the data and allows the determination of the beam divergence, θ, beam current, I_b, and total ion current, I_i.

A Faraday probe is a plasma diagnostic tool and is used to measure the ion current density. The family of Faraday probes includes nude, cupped, collimated, gridded and magnetically filtered probes. The standard Faraday probe is called a nude probe [13]. Figure 9 shows a cross-section of a nude probe.

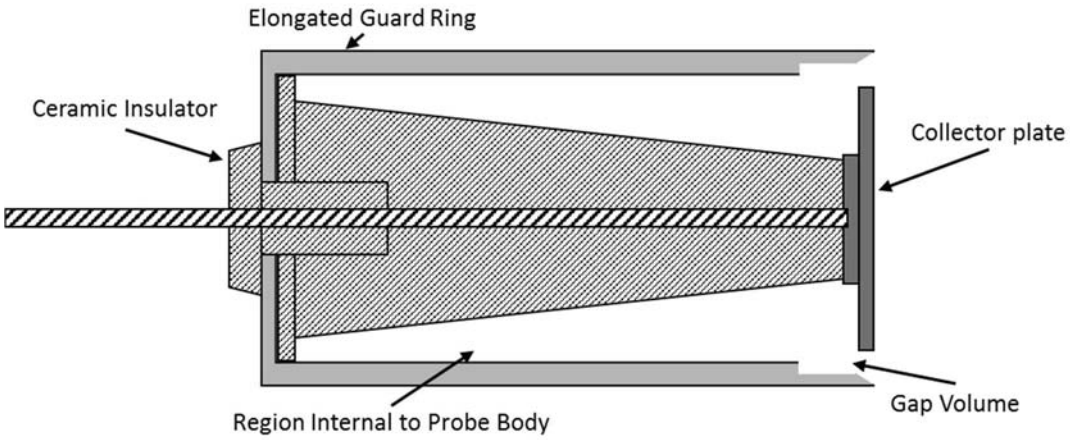

Figure 9. Cross-section of Jet Propulsion Laboratory Nude Faraday Probe

The probe consists of a collector plate, the guarded ring, and a ceramic insulator. The collector and guard ring are both biased to a negative potential to minimize edge effects around the collector and ensure proper ion collection [14:4]. During data collection, the probe is placed behind the thruster and inside the thruster's plasma beam. The ions impact the collector and generate a current that is measured to find the current density. To fully characterize the thrust data, multiple points through the full range of the thrust beam have to be measured. The result provides the ion distribution in the thrust beam.

Only the axial component of the thrust beam ion velocity results in effective thrust. Therefore, the beam divergence angle is an important unit to describe how efficient a thruster is at producing usable thrust. The beam divergence can be found using the ion distribution. Figure 10 illustrates the general thrust plume geometry of an ion thruster [15].

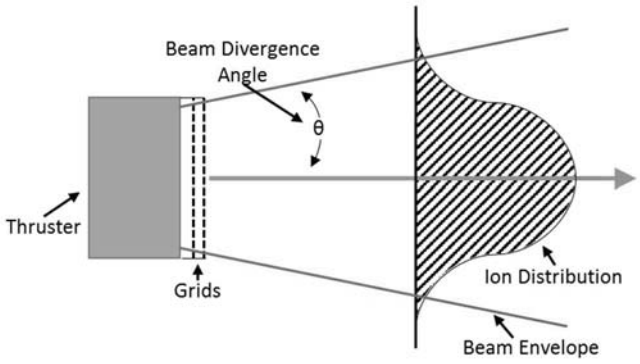

Figure 10. Diagram of Thrust Plume Geometry

Neutralizing Cathode

Cathodes are utilzed in ion thrusters for two purposes, both of which utilize electron discharge. The first, always required for proper thruster function, is using the electrons to neutralize the ion beam leaving the thruster. The second, required only for some thruster designs, ionizes the propellant gas inside the chamber to produce the plasma. The cathodes are essential components of ion thrusters. Thus, the properties of the cathodes influence the lifetime of the ion thruster [1:243]. Two different types of cathodes will be used in this experiment: a hollow cathode and a propellant-less carbon nanotube (CNT) field emission (CNTFE) cathode.

Hollow cathodes consist of a hollow refractory tube ending in a plate with a small centered hole. Inside the tube is a cylindrical insert, placed against the plate. The insert is an active electron emitter which can be comprised of several different materials. The hollow tube is wrapped by a sheathed heater which is designed to raise the temperature of the insert to emissive temperatures. The keeper electrode facilitates starting, maintains the cathode temperature, and protects the internal components from environmental

damage. When the insert reaches the proper temperature, a small amount of electrons are emitted from the insert. After the insert is heated, a small portion of the propellant gas is injected into the center tube. These electrons from the insert impact the incoming gas particles, ionizing the gas to a plasma. A large electron field inside the cathode keeps the plasma in place. The electrons are then accelerated out of the cathode by same electron field, creating an electron plume outside the cathode [1:247]. Figure 11 shows a cross-section of a standard hollow cathode.

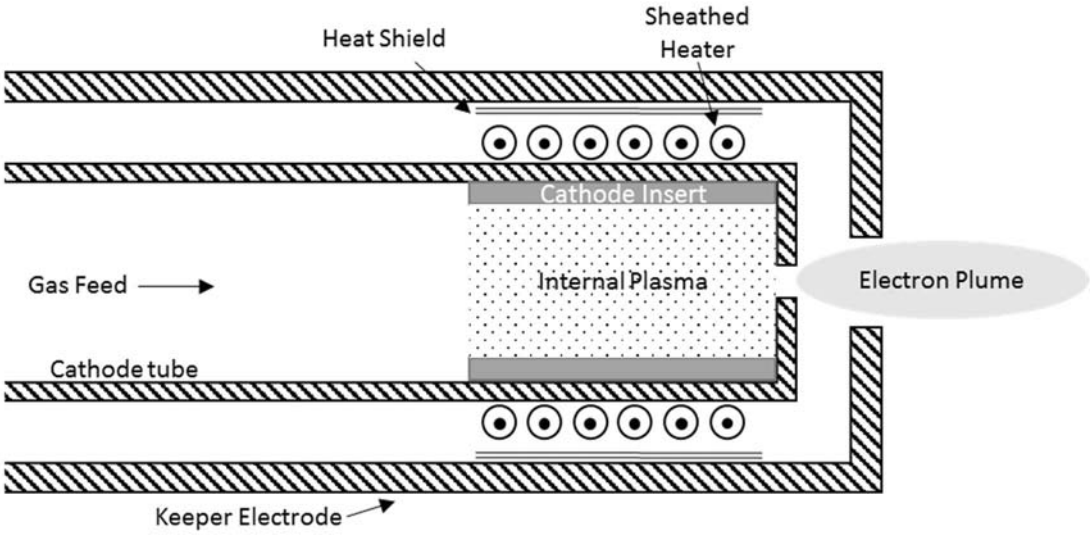

Figure 11. Generic Hollow Cathode Schematic

The other type of cathode that will be used in this experiment is a CNTFE cathode. This cathode differs from most other cathodes because it is designed to be propellant-less and heater-less. These are extremely useful features because the cathode will not consume any propellant, nor will it consume power for heating. CNTs have unique emission characteristics resulting from their electrical conductivity and high

aspect ratio [16:394]. Using these characteristics and an array of CNTs, a CNTFE cathode can be manufactured. As seen in Figure 12, CNTs are lined up below a focusing gate [17:10]. When the correct electric field is applied to the cathode, the CNTs emit electrons. The electrons are then aligned and forced out through the gate.

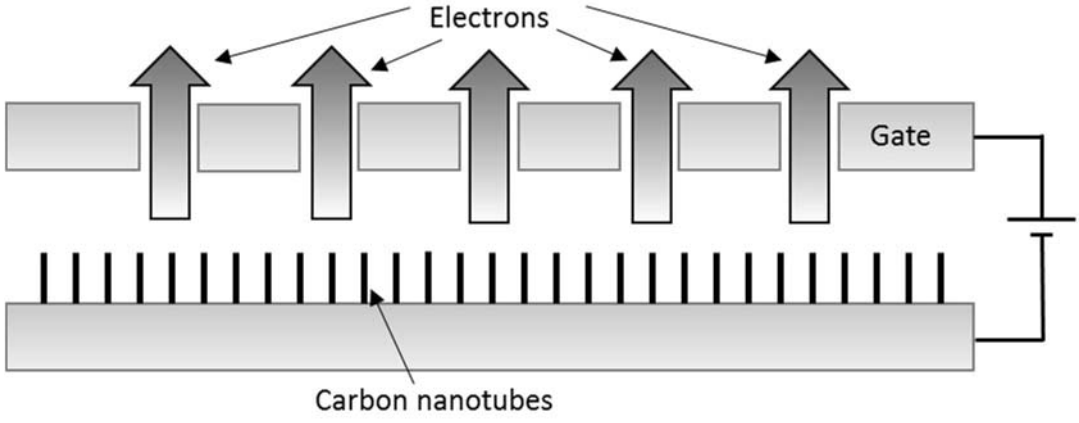

Figure 12. Generic CNTFE Cathode Design

Ion Thruster Sizing

Due to the simplicity of ion thruster design, ion thrusters can be scaled to be both larger and smaller in size. There are limiting factors in both directions. Larger ion thrusters require more power which in turn increases the size of the power processing unit. Additionally, the thrust produced is proportional to grid area. Therefore, the size of the ion thruster is limited by the spacecraft and launch vehicle capabilities as well as manufacturing capabilities. Smaller ion thrusters are limited by the power processing unit, the space charge effect, and the vacuum voltage breakdown limits [1:200]. For this experiment, the impacts of reducing the size are investigated.

There are few unique aspects of RF ion thrusters supporting size reduction. First, an ion thruster does not require an internal cathode to produce the plasma cloud. Second, the radio-frequency plasma generation design replaces the need for a permanent magnet [5:3]. Third, the holes in the ion optics scale inversely with the size of the thruster. Therefore as the thruster decreases in size, fewer holes will be required for the smaller grids [4:29].

Research completed by Dr. Tsay for Busek Co. Inc. indicated the most challenging aspect of scaling down an RF ion thruster is in regards to the diminishing coil inductance due to geometrical constraints. The overall desire for size reduction is to reduce the thruster's size while maintaining the preferred performance and efficiency characteristics. An issue occurs due to increased ohmic heating losses as size and overall power scale down. Ohmic heating, also known as electrical resistance heating, occurs when electric current passes through a conductor, thereby releasing heat. To scale down the thruster efficiently, Tsay compiled a list of guidelines based on experimental [5:3]. These guidelines are found below in Table 1.

Table 1. A General Guideline for Scaling Down an RF Ion Thruster from Busek Co. Inc. [5:3]

Design Parameter	Preference	Issue
Grid Diameter	An ideal grid diameter is based on a target thrust, assuming high grid transparency and known beamlet current.	None, but may need to increase the grid diameter to match the actual chamber size. The grid's open fraction will then be reduced to meet the target thrust.
Discharge Chamber Diameter	Matching the ideal grid diameter.	If the chamber is too small, the coil inductance will be too low and the ohmic heating loss will be very severe.
Discharge Chamber Length	As short as possible for minimizing ion wall loss.	A short chamber limits the number of coil turns and its inductance value.
Operating Frequency	Producing a skin depth that is 1/2-2/3 of the chamber radius.	The coil's effective series resistance and ohmic heating loss increase with increasing frequency.
Number of Coil Turns	As high as possible for maximizing coil inductance.	A longer coil translates to a higher ion wall loss. It also increases the coil resistance and ohmic heating.
Coil Cross-Section Diameter	As large as possible for minimizing coil resistance and ohmic heating loss.	A larger cross-section translates to fewer coil turns, which reduces the inductance.

Previous Thesis Work

In 2016, Lieutenant Muilenburg performed an thesis experiment on the same BIT-1 ion thruster with similar research objectives at the Air Force Institute of Technology (AFIT). Lt. Muhlenberg did not fully meet his thesis objectives because he was unable to get the thruster to successfully operate at AFIT. Therefore, his research was relocated to one of Busek's laboratories where he was able to operate the thruster with help from Busek Engineers. The vacuum chamber at Busek was too small for a thrust stand. Consequently, the thrust data was instead calculated using the estimated relationship of the beam current, screen voltage, and the type of propellant used. The divergence angle data was also acquired by manually positioning the Faraday probe during several tests.

The neutralizing cathode component of the ion thruster was the cause of additional issues during operation, resulting from excessive wear. The calcium aluminate insert in the cathode produces electrons when power is applied. The power applied heats the insert, producing electrons. Consequentally, the size of the insert is reduced. As the insert becomes smaller, more power is required to produce enough electrons to neutralize the beam. This waterfall effect significantly reduced the lifetime of the cathode. Therefore, Muilenburg suggested using a different cathode design for proper testing [6].

III. Methodology

Chapter Overview

Initially, AFIT purchased the BIT-1 ion thruster and the associated power-control tower from Busek. This tower provided the hardware for three power supplies and the RF generation requirements. In addition to the hardware, a software program was provided for starting, operating, and controlling the power and RF inputs to the thruster. In previous work, this tower was damaged beyond repair. Consequently, for this research, the thruster operational requirements were met with several individual equipment components. This chapter outlines the methodology, the setup process and utilization of equipment, and the order of data collection. Three experimental setups were developed to start the thruster and record data, the initial setup, the intermediate setup, and the thrust stand setup. A few issues which arose during the experiment and the troubleshooting steps implemented are also discussed.

Vacuum Chamber

AFIT's Space Propulsion Application Simulation System (SPASS) Laboratory provided the location and hardware for this research. The major component required to perform the research was a high capacity vacuum chamber. The cylindrical chamber is 2.5 meters long and 1.8 meters in diameter with curved doors on each side, equating to an approximate internal volume of 6.5 cubic meters. Employing a two-stage pump down system, the vacuum chamber is capable of reaching and maintaining pressures on the order of 10^{-7} torr (10^{-5} Pa). The first stage of pumping, reaching approximately 10^{-4} torr

(0.01 Pa), was performed by a Leybold Screwline SP 250 dry vacuum pump. Once the pressure reduces to the limit of the SP 250, the system automatically switches to four 20-inch CVI Torr Master 500 and two 8-inch CVI Torr Master 150 cryogenic pumps. These cryogenic pumps use liquid helium at about 20 K to condense gasses inside the chamber, thereby reducing the internal pressure to 10^{-7} torr. Figure 13 shows a picture of the vacuum chamber in the AFIT SPASS Lab

Figure 13. AFIT Vacuum Chamber

Power Supplies

For the experimental setup of the BIT-1 ion thruster, three power supplies are required for thruster operation with one additional power supply needed for the cathode operation. The first power supply, Glassman High Voltage Inc. series EK, was attached

to the screen grid, providing positive power. The remaining two of the power supplies, both Standford Research Systems Inc. Model PS350/5000V-25W, which are toggled in-between, are connected to the acceleration grid. Figure 14, below, shows the power supplies and toggling box used in the experiment.

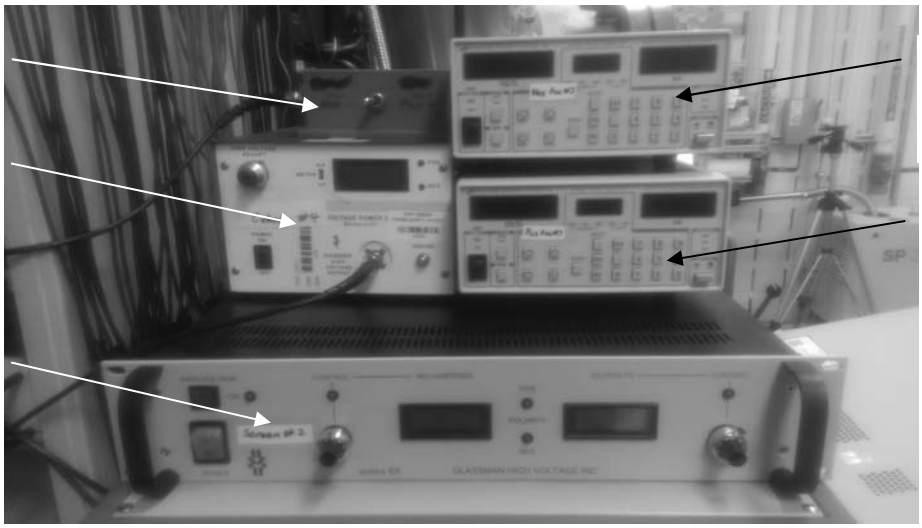

Figure 14. Power Supplies Used in the Experiment and the Custom Made Polarity Toggling Box

Each of the power supplies was connected through the vacuum chamber's walls to the thruster using Bayonet Neill–Concelman (BNC) cables. A wiring diagram of the experimental setup is shown in Figure 15

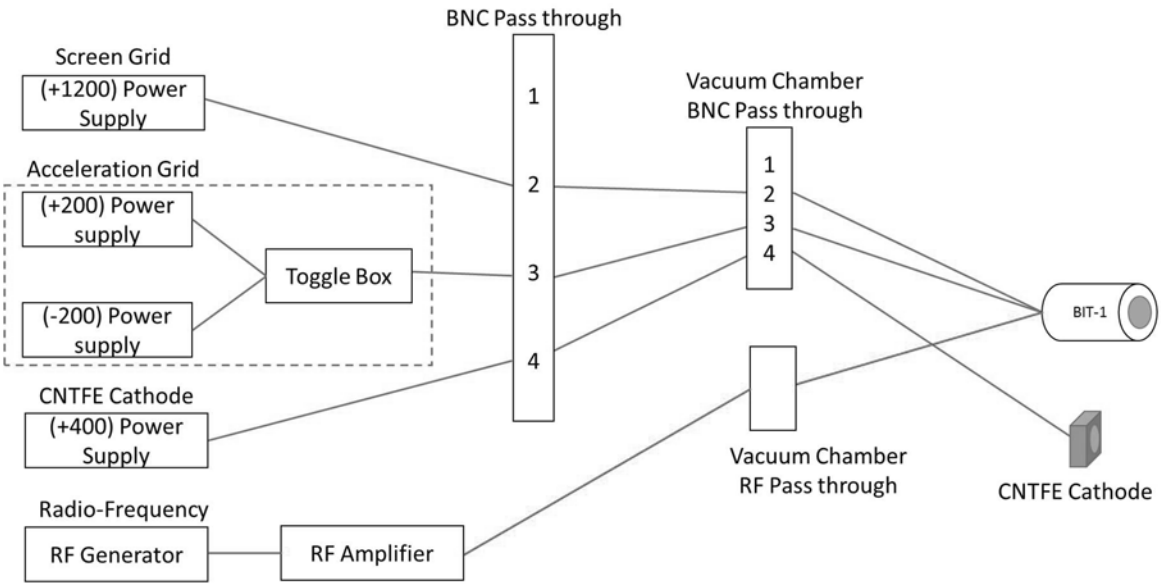

Figure 15. Wiring Diagram of Experimental Setup

In addition, the two acceleration grid power supplies are initially attached to the polarity toggling box. This box allows the power to be quickly switched between the two devices, transferring between the positive and negative power supplies. The negative voltage power supply was used during normal operations, and the positive voltage power supply was used during the start-up procedure to pull in seed elections to initialize the plasma generation. The internal configuration of the toggling box is shown in Figure 16 and a schematic of the switch is shown in Figure 17.

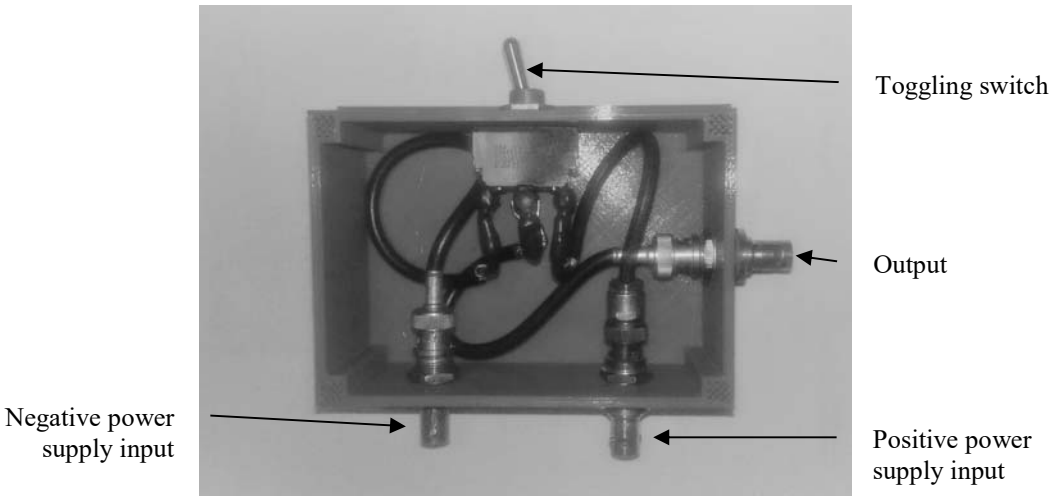

Figure 16. Internal Configuration of the Custom Made Toggling Box

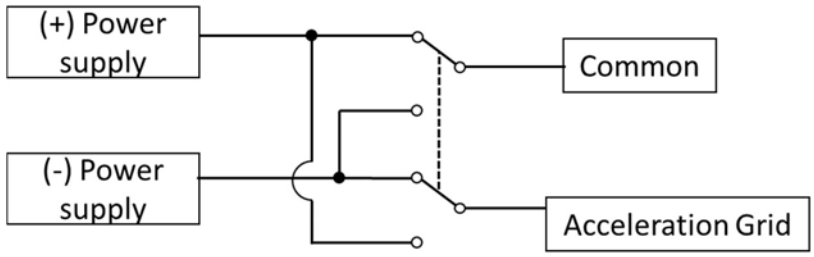

Figure 17. Schematic of the Toggle Switch

Radio Frequency Generation

The next component required was radio frequency generator. This experiment used a radio frequency analyzer, generator, and amplifier. Figure 18 shows the Agilent MXG Vector Signal Generator N5182B and Agilent Signal Analyzer E5062A utilized in the experiment.

Figure 18. Radio Frequency Generator (Top) and Radio Frequency Analyzer (Bottom)

RF ion thrusters require a particular amount of power to be transmitted to the electrons in the chamber at the correct frequency along with the lowest reflected power. This set of requirements occurs at the thruster's resonant frequency. Therefore, the preliminary step was to find the resonant frequency of the chamber using the RF analyzer. The RF analyzer was attached through the vacuum chamber wall to the thruster in order to simulate experimental operating conditions. Next, a signal was sent from the analyzer to the thruster where the signal reflected and then returned to the analyzer. The difference between sent and reflected signal was evaluated by the analyzer. From this signal difference, the resonant frequency was determined. A screen capture from the RF analyzer displaying the result is shown in Figure 19.

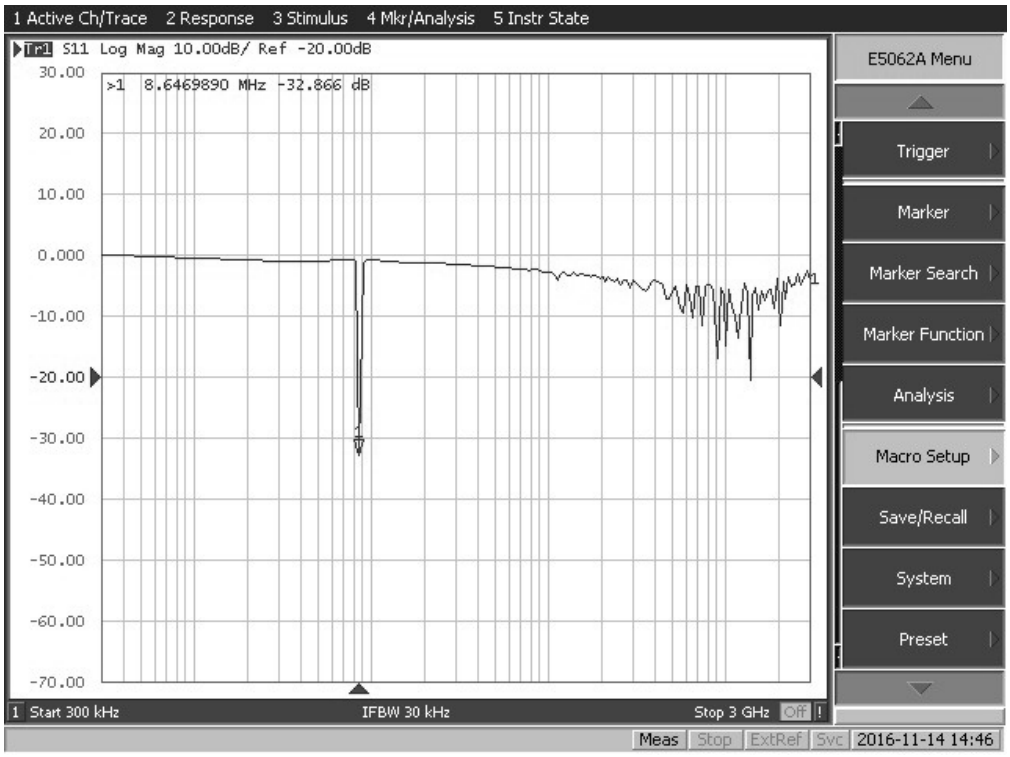

Figure 19. Screen Capture from the RF Analyzer Displaying the Resonant Frequency

The resultant resonant frequency, 8.646989 MHz, which represents the precision of the analyzer, was then input into the RF generator. However, the generator used in the experiment can provide a maximum of 1 W of power, which does not meet the range of power required by BIT-1 for operation. Therefore, the RF generator Electronics & Innovation 2100L was attached to a RF power amplifier, shown below in Figure 20.

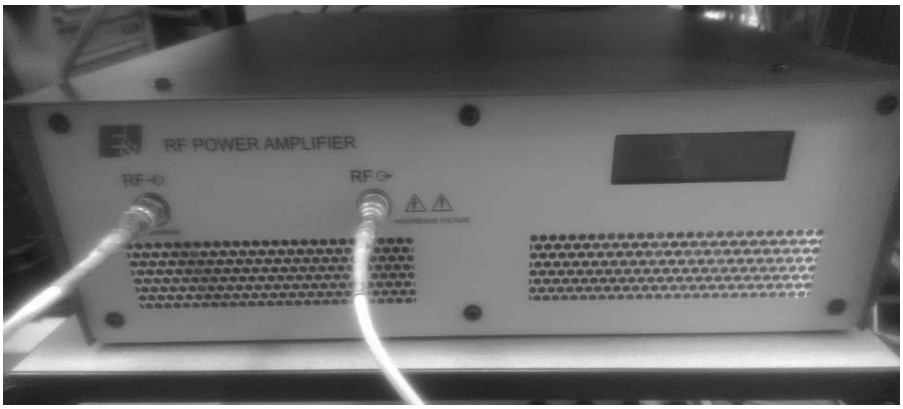

Figure 20. Radio Frequency Power Amplifier

The RF amplifier is a simple uncontrolled 100 W amplifier which was adjustable based on input power. A power input of 0.01 W, for example, results in a 1 W power output from the amplifier. Using the amplifier, the required variable power range of 5 to 10 W was achieved.

Flow Controller

The BIT-1 ion thruster requires a mean propellant flow of 0.06 sccm of xenon which is much less than the flowrate of larger ion thrusters. The Omega Mass Flow Controller, FMA-2601A, was chosen to regulate the propellant flow properly. The FMA-2601A flow controller is capable of a max input pressure of 145 pisg and a range of 0 to 0.5 sccm of propellant with an accuracy of ±(0.001 + 0.08% of the reading) sccm [18:56]. This indicates the mean propellant flow implemented in this research was 0.06 ±0.00148 sccm. The initial configuration of the flow controller is shown in Figure 21. A schematic of the full propellant path is shown in Figure 22.

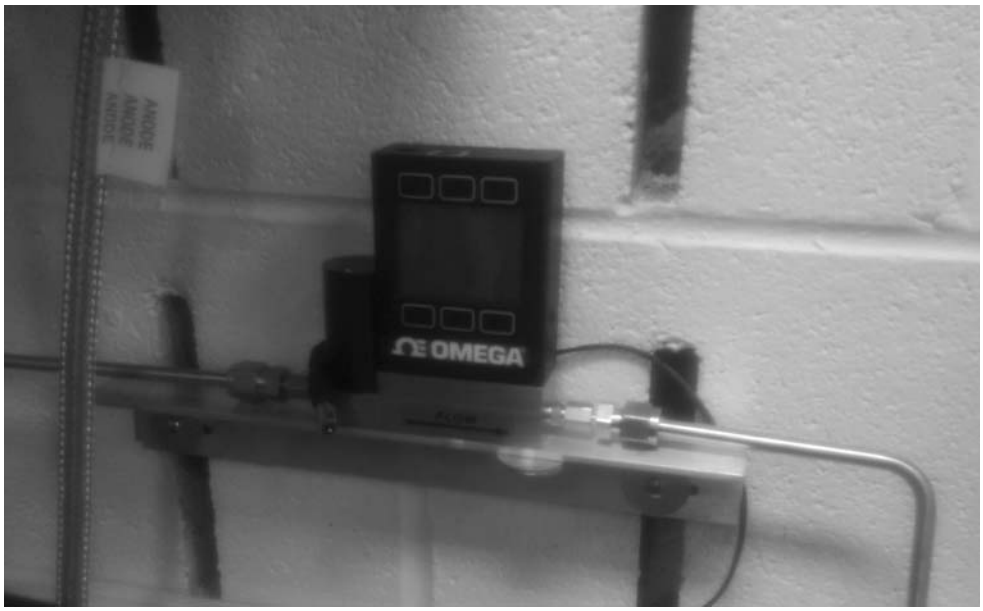

Figure 21. Initial Configuration for FMA-2601A Flow Controller

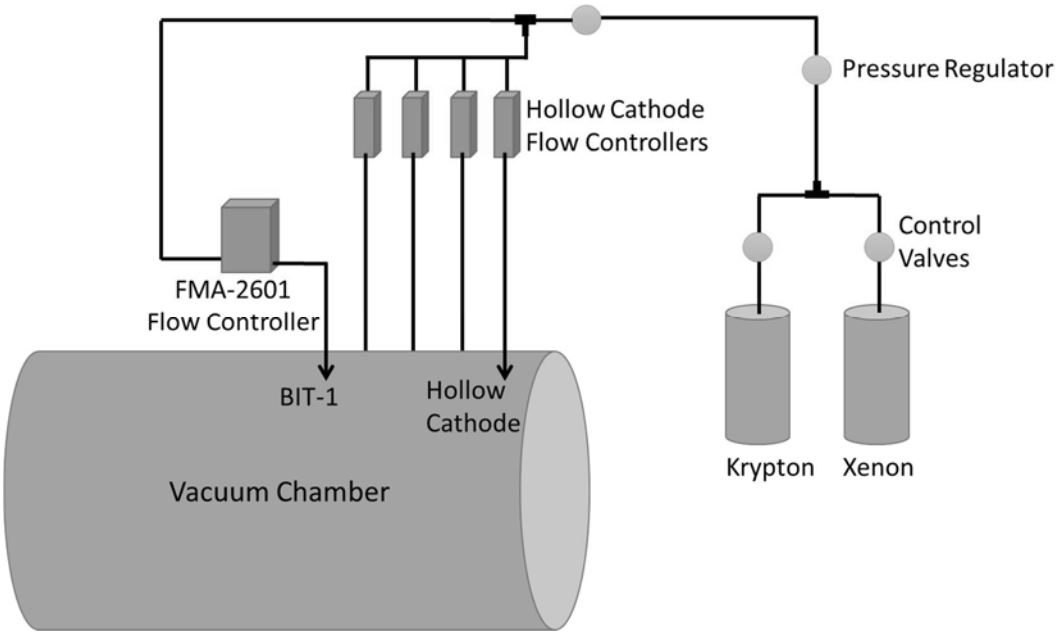

Figure 22. Propellant flow Configuration for the Experiment

Figure 24 shows 4 additional flow controllers which the vacuum chamber came equipped with. These are MKS Type 247 Flow controllers. One of these controlled the propellant flow to the hollow cathode during the experiment.

During the first test of the BIT-1 ion thruster in this research, the flow controller displayed a volumetric overrange (VOV) error. This means the measured volumetric propellant flow exceeded the range of the sensors on the flow controller. Through communications with an Omega technology representative, they concluded the flow controller was setup in the wrong configuration for vacuum testing [19]. There are two configurations the flow controller can be set up with, an upstream configuration and a downstream configuration, which change the location of the control valve. Figure 23 illustrates the two configurations.

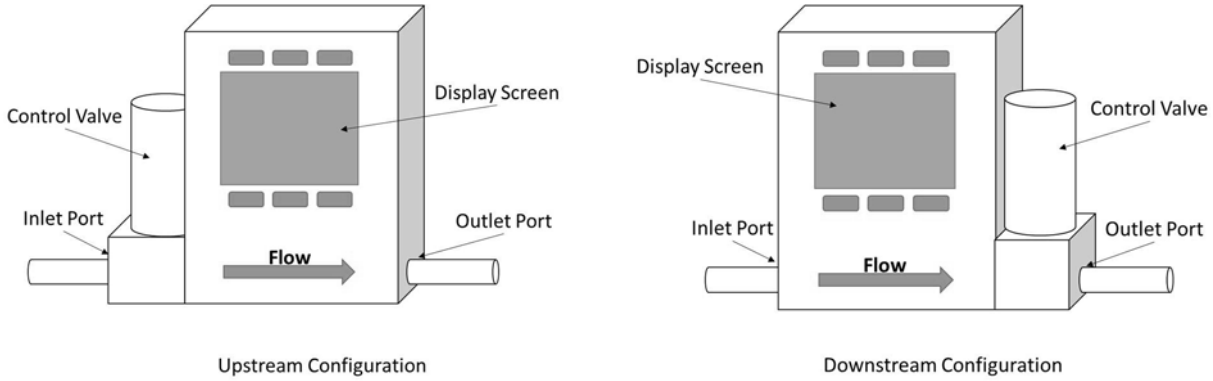

Figure 23. Illustration of the Two FMA-2601A Configurations

The initial configuration for the flow controller was upstream configuration. This means the outlet port was subject to the pressure suction of the vacuum chamber. Since the FMA-2601A uses the pressure difference between incoming flow and outgoing flow, the near vacuum pressure on the outlet port caused a VOV error to occur. Following this

conversation with the Omega technician, the FMA-2601A was reconfigured to a downstream setup. The second configuration of the flow controller is shown below in Figure 24.

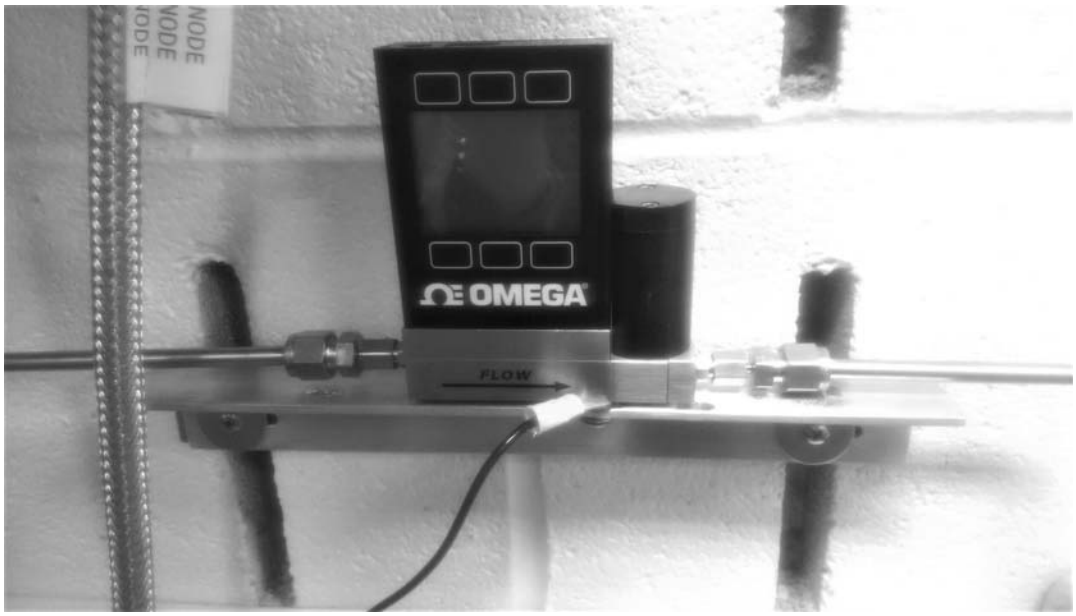

Figure 24. Second Configuration of the FMA-2601A Flow Controller

The reconfigured FMA-2601A allows the flow controller to properly read the pressure difference between the inlet and outlet ports. Throughout the remainder of the testing, the VOV error did not occur.

Hollow Cathode

Originally the BIT-1 was designed to start the plasma generation with the CNTFE Cathode. After several unsuccessful attempts to start the thruster at Busek, an addon plasma igniter was incorporated along with the thruster. For this experiment, the original

setup for the BIT-1 was tested. Therefore, a method of initiating plasma generation was required. During testing Busek developed the following concept:

> The initial theory was that these neutralizer electrons are too energetic (typically 400-600eV) to be drawn into the discharge chamber during the grid polarity reversal. To examine this theory, we placed the cathode pointing directly at the grids, but it still failed to ignite the plasma. This result led to the conclusion that the CNTFE cathode simply does not produce enough seed electrons to start the main discharge. [5:4]

Leveraging the above information, an initial theory for the requirement of successful plasma generation was to create a large population of low energy electrons near the grids of the thruster. Thus a second cathode was needed for starting the BIT-1.

The BHC-1500 hollow cathode was chosen for its availability and large output of low energy electrons. The BHC-1500 uses a porous tungsten hollow insert which is impregnated with a barium-calcium-aluminate mixture [20:1]. This cathode is designed to be used typically with Hall thrusters which are much larger than the BIT-1. Therefore the number of electrons produced was more than BIT-1 requires for the plasma generation and, thus, more than sufficient. Figure 25, below, shows the BHC-1500 hollow cathode used in this experiment.

Figure 25. BHC-1500 Hollow Cathode

Concurrently with this experiment, a 600W Hall thruster was being testing in the same vacuum chamber. This Hall thruster used the BHC-1500 for its plasma generation. The first experimental setup mounted the BIT-1 next to the Hall thruster and used the supports from the Hall thruster to hold the hollow cathode. Subsequently, the experimental setup was redesigned with the hollow cathode mounted overtop of BIT-1. The redesigned setup ensured enough electrons were available for the plasma generation. Further discussion of the redesigned setup will be addressed later.

CNTFE Cathode

To ensure a realistic test of the BIT-1, a cathode was required which would be similar to the one used on orbit in addition to the cathode required for starting the thruster. For this experiment, the Busek's Propellant-less Carbon Nanotube Field

Emission Cathode was chosen. This cathode incorporates multi-walled carbon-nanotubes developed and manufactured by Busek [20:3]. The CNTFE cathode is shown in Figure 26 in the next section.

Thruster and Cathode Mounts

To properly test the BIT-1, mounts were needed for both the BIT-1 and the CNTFE cathode. The mounts were required to attach to the vacuum chamber's 80/20 aluminum framework attached to a translation stand as well as the Busek thrust stand. Below, the BIT-1 ion thruster and the CNTFE cathode are shown in Figure 26 along with a ruler for scale.

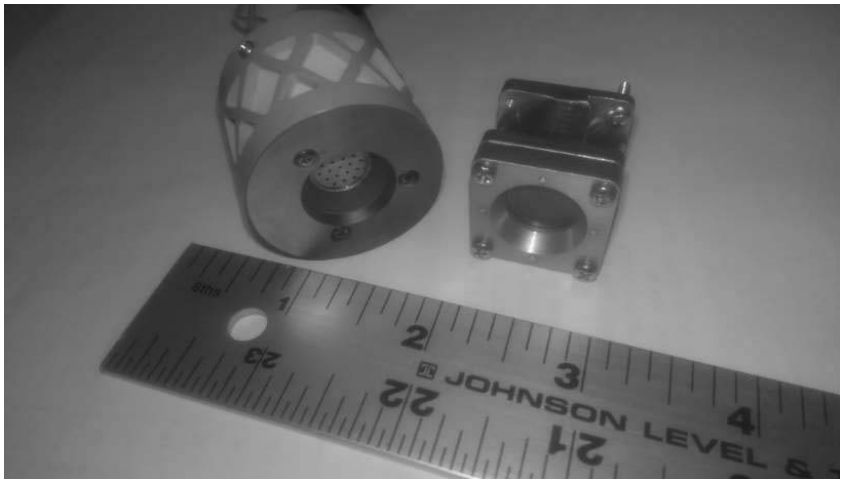

Figure 26. BIT-1 Ion Thruster (left) and CNTFE Cathode (right)

Previously, a mount was designed and fabricated for the BIT-1 for testing in the vacuum chamber and thrust stand. The mount was fabricated in-house at AFIT out of polyether ether ketone (PEEK) plastic [6:38]. This stand was designed to prevent any

unwanted rotation in the thruster with a single screw. For the CNTFE cathode, a mount was designed to support the three screws of the cathode and attach to an 80/20 aluminum L-bracket using a single screw. The bracket was designed in SolidWorks and built in-house out of aluminum. The L-bracket attachment side contains two holes for height adjustment. The cathode attachment side contains three holes for cathode mounting and a removed corner. The corner of the mount was cut off to make room for the CNTFE cathode's ground wire. Figure 27 shows the two mounts designed for the experiment.

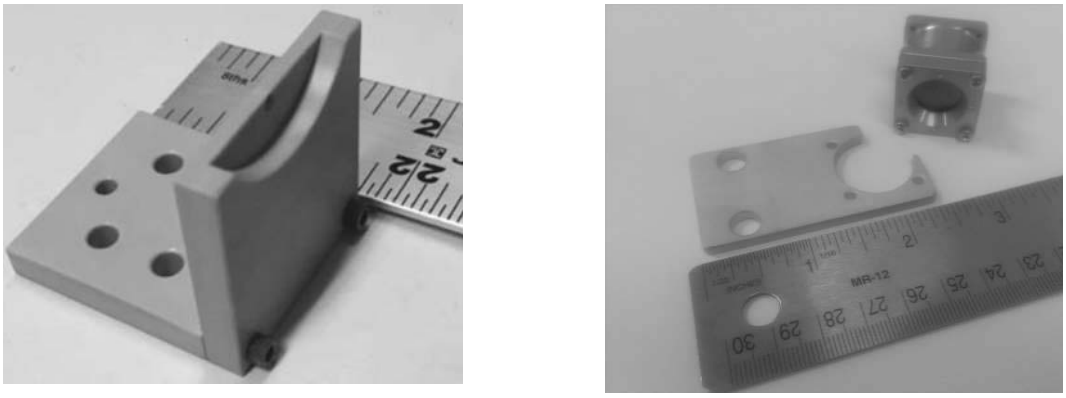

Figure 27. BIT-1 Ion Thruster Mount (left) and CNTFE Cathode Mount (right)

Initial Experimental Setup

Once the mounts were fabricated, the BIT-1 and CNTFE cathode were attached to the 80/20 aluminum translational stage. This translational stage allowed for three-axis adjustment for the thruster's placement inside the chamber. Therefore, during testing, the thruster was aligned horizontally and vertically with the instrument taking the data. The first experimental setup is shown in Figure 28, with the BIT-1 attached to the 80/20 aluminum using the PEEK plastic thruster mount. The CNTFE cathode was attached to

the aluminum mount, which in turn, was connected to the 80/20 aluminum via an L-bracket. Next, Figure 29 shows the wiring description for the experimental setup. Figure 30 shows the front view of the initial setup including the hollow cathode.

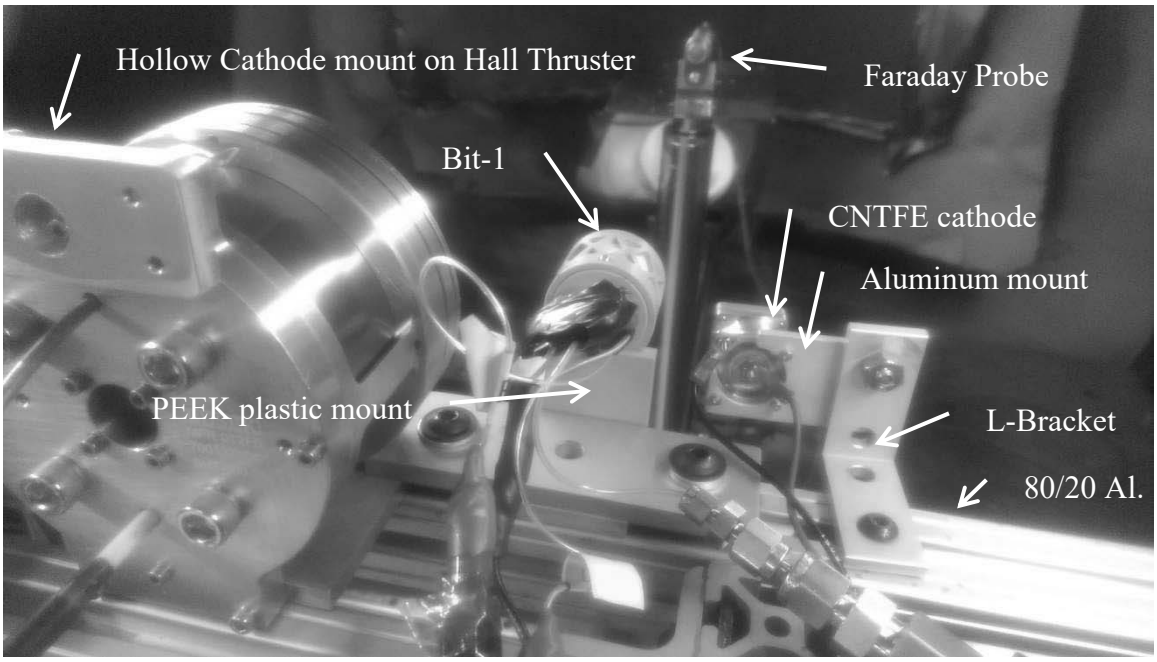

Figure 28. Initial BIT-1 Ion Thruster and CNTFE Cathode Experimental Setup

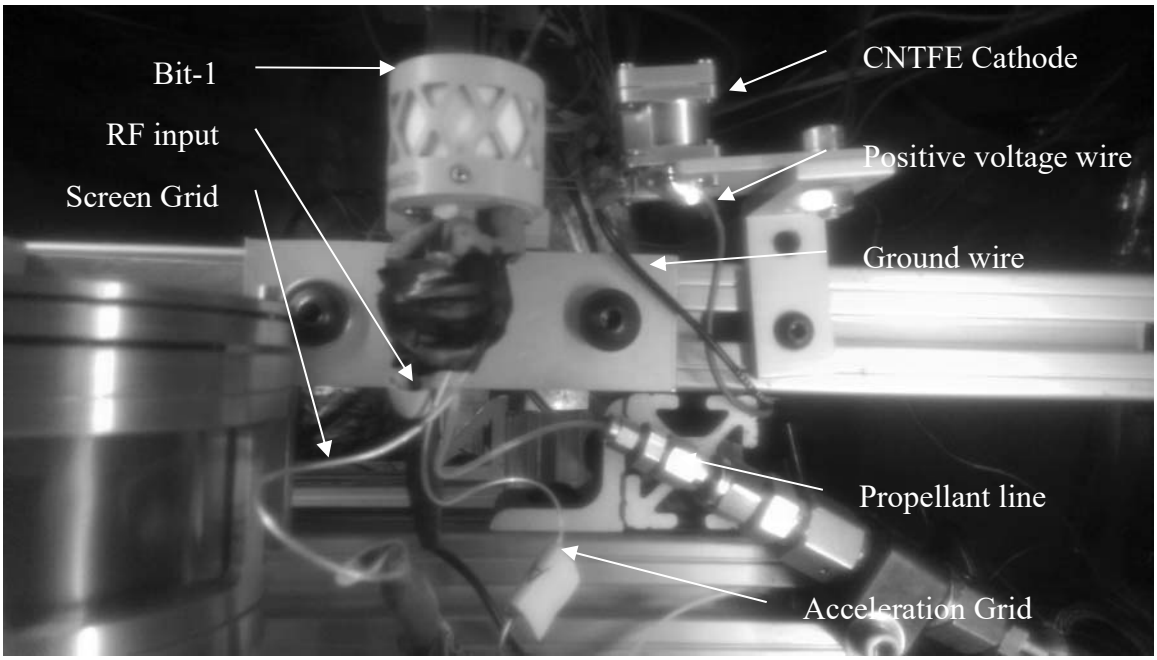

Figure 29. Top-down BIT-1 and Cathode Wiring Setup

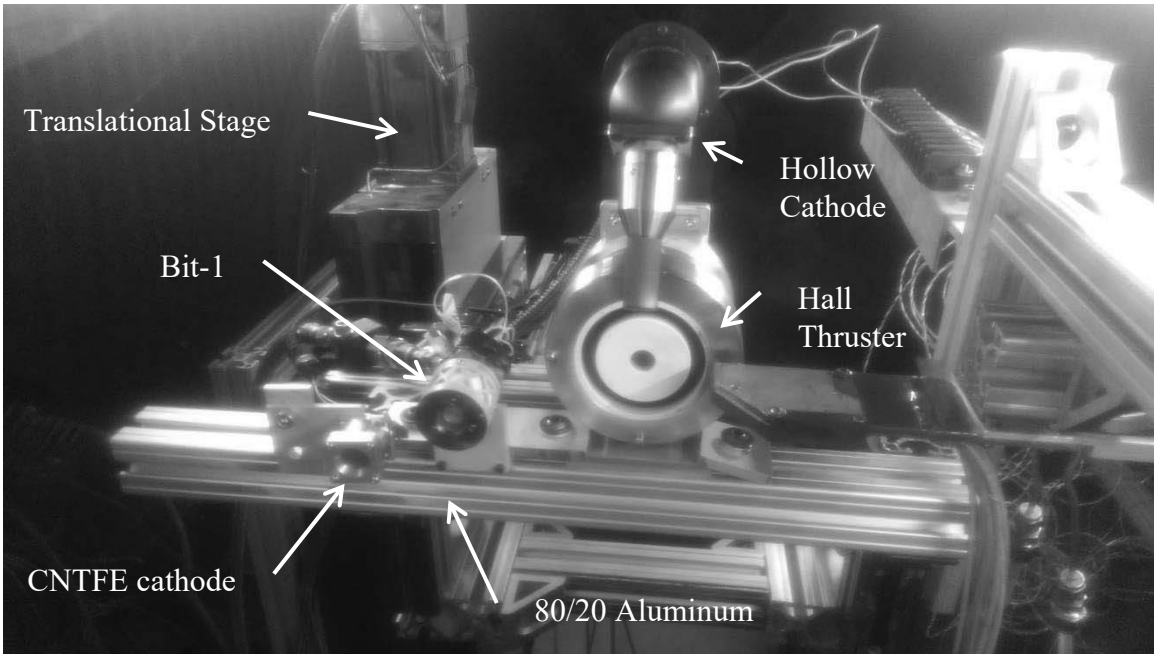

Figure 30. Initial Experimental Setup from the Front with Hollow Cathode

Intermediate Experimental Setup

In the initial experimental setup, the BIT-1 did not successfully start. The assessment was the BHC-1500 was too far away to draw sufficient electrons to start the plasma generation. Therefore, the experimental setup was redesigned. More details on the troubleshooting steps are discussed in the next chapter. The intermediate setup relocated the hollow cathode to directly above and in front of the BIT-1, about 2 inches away. Essentially, this change reduced the distance between the BIT-1's acceleration grid and the output of the hollow cathode. Consequentially, during the startup polarity switch of the acceleration grid, a larger quantity of seed electrons was pulled inside the chamber. The intermediate setup is shown in Figure 31.

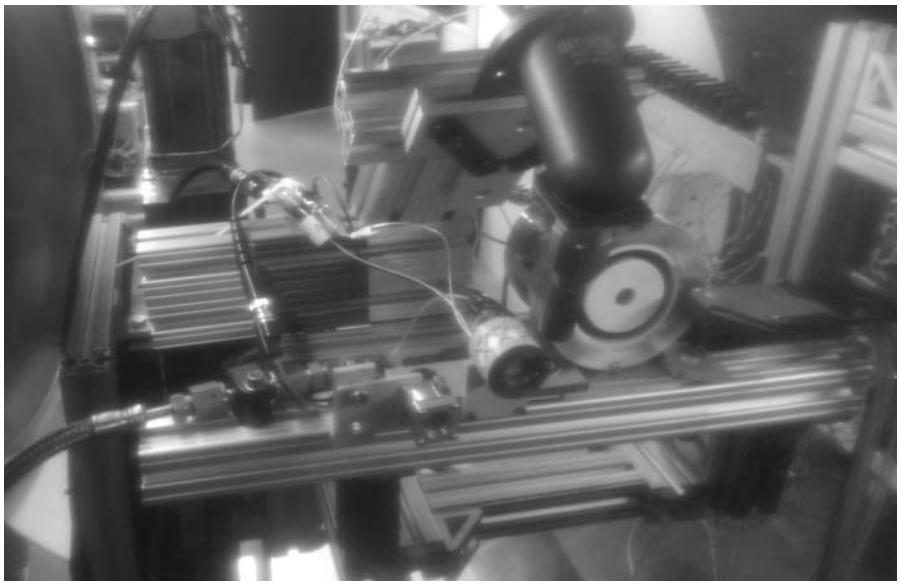

Figure 31. Intermediate Experimental Setup from the Front

Operating Requirements and Starting Procedure

In order to start and operate the thruster, the power supplies, RF generator, and the flow controller are required to be set to specific conditions. The *User Manual for Busek 1cm RF Ion Thruster BIT-1 System* provided the starting procedure and operational conditions using Busek's power-control tower [21]. From this manual, the generic operating requirements and startup procedure were extracted. Table 2, below, lists the starting and nominal operating conditions as well as the flight envelope which is the operational variable range of the thruster and cathode.

Table 2. Operational Power Requirements

						Flight Envelope - Operational Variable Range		
	Starting Conditions			Nominal Conditions		Min	Max	
RF		8.5	W	7.5	W	6	10	W
Cathode	+	400	V	400	V	400	600	V
Screen Grid	+	1200	V	1800	V	1500	1800	V
Accel Grid								
Pos	+	200	V					
Neg	-	200	V	-200	V	-100	-200	V
Prop Flow		0.08	sccm	0.04	sccm	0.04	0.08	sccm

The procedure for starting the thruster was also interpreted from the user manual. Additional steps were incorporated into the steps listed in the manual to compensate for the unique thruster experimental setup. Below are the final steps followed to start the BIT-1 thruster, specific to this experimental setup, after starting the hollow cathode:

1. Set flow controller to 0.6 sccm for 5 minutes.
2. After 5 minutes, reduce flow controller to 0.08 sccm.
3. Ensure polarity switch starts on negative power supply.
4. Turn on positive acceleration grid power supply (preset to +200 volts).
5. Turn on negative acceleration grid power supply (preset to -200 volts).

6. Turn on screen grid power supply (preset to +1200 volts).
7. Turn on radio frequency amplifier.
8. Turn on radio frequency generator and increase amplitude until output power equals 8 watts (preset to frequency 8.646989 MHz).
9. Turn on CNTFE cathode power supply (preset to +400 volts).
10. Use the polarity switch to flip from negative to positive power on the acceleration grid – remain for 1-2 seconds then return to negative power.
11. Check the BIT-1 for continued plasma generation inside grids, i.e. illumination from the grid holes.
12. Ensure BIT-1 remains active through steps 13-16, checking in-between each change.
13. Once plasma generation is achieved, increase screen grid from 1200 V to 1800 V in 50 V increments.
14. Reduce flow controller to 0.05 sccm.
15. Vary RF generator frequency to ensure 0 volts return power.
16. Reduce RF generator amplitude to 7.5 watts.

Faraday Probe

The first set of data recorded for the experiment measured ion current densities using a Faraday probe. The probe chosen was manufactured by Plasma Controls and came with the Faraday probe and an associated isolator mount. Figure 32 shows the Faraday probe used in the experiment.

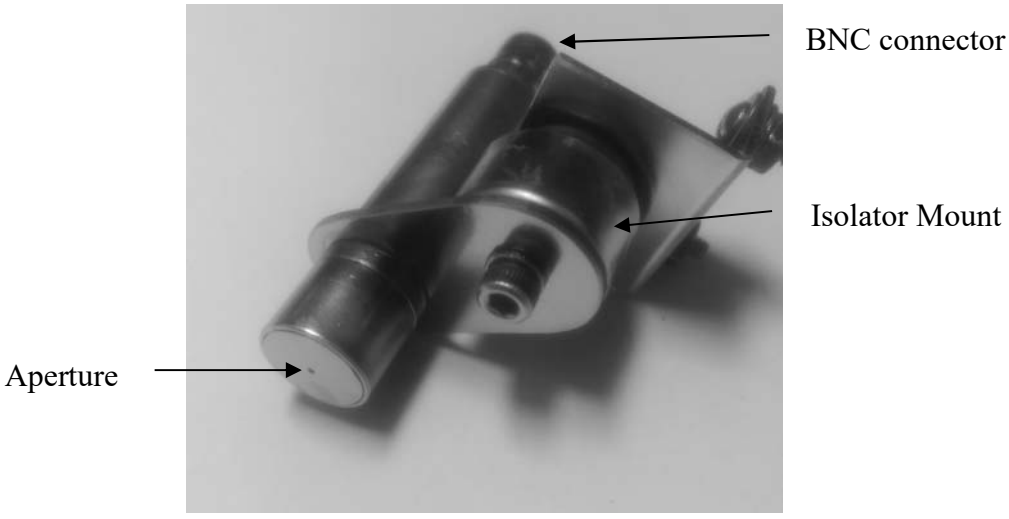

Figure 32. Faraday Probe with the Isolator Mount

The probe consists of a collector plate which completely shields the probe body, except for a 0.0381 cm aperture. The isolator mount electrically isolates the probe from the mounting surface. The collector plate inside was electrically connected to the center wire of the BNC and the outside body was electrically connected to the outside of the BNC cable. These separated connections allow the collector plate to be biased to positive 30 volts from ground and the probe body biased to negative 30 volts from ground. The two potientials enable the probe to repel any low energy charged exchange ions and repel the beam plasma electrons from reaching the collector plate, respectively. In addition, the duel opposite biases assist to minimize any secondary electrons produced from the ions striking the plate.

After the voltages are applied to the probe and during the thruster operations, ions from the plasma thrust plume will enter the probe body through the aperture and hit the collector plate. This imparts a current which was measured by reading the voltages across a resistor electrically placed between the collector disk and ground. Once voltages are recorded, the current density was found using the calculation:

$$J = \frac{V \cdot 1000}{R \cdot A} \tag{31}$$

where J is the current density in mA/cm^2, V is the recorded voltage in volts, R is the value of the resistor in ohms, and A is the area of the aperture [22]. For this experiment, the resistor used was 4.66 MΩ and the area of the aperture was 0.00114 cm^2. The full current map can be found using Equation 31.

In conjunction with the Faraday probe, a translational stage was used to gather the data. The translation stage, also manufactured by Plasma Controls, is capable of dual axis

translation and single-axis rotation. Figure 33 shows the translational stage inside the vacuum chamber along with the axis labels.

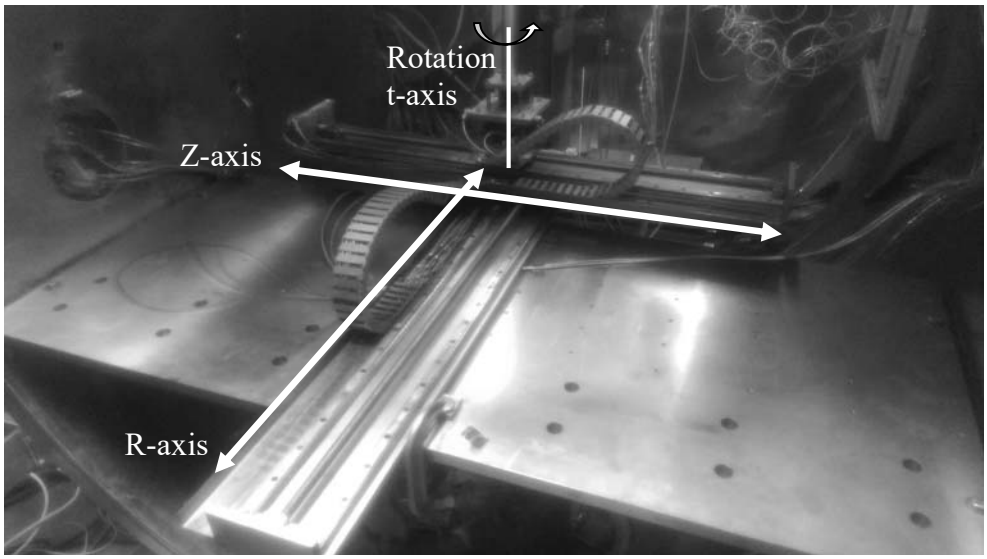

Figure 33. Translational Stage with Labeled Axes

To take data valuable for current mapping, the probe was required to point directly at the thruster and maintain a constant radial distance. One of the translational stand programs allows the stand to follow an arc around a chosen axis while rotating the t-axis to point at the same point in space. Therefore, the probe can trace an arc, equidistant to the ion thruster, and rotate to ensure highest current density was recorded. This was repeated at increasing distances from the thruster. Figure 34 shows a schematic of how the Faraday probe and the translational stage work in tandem to gather the data.

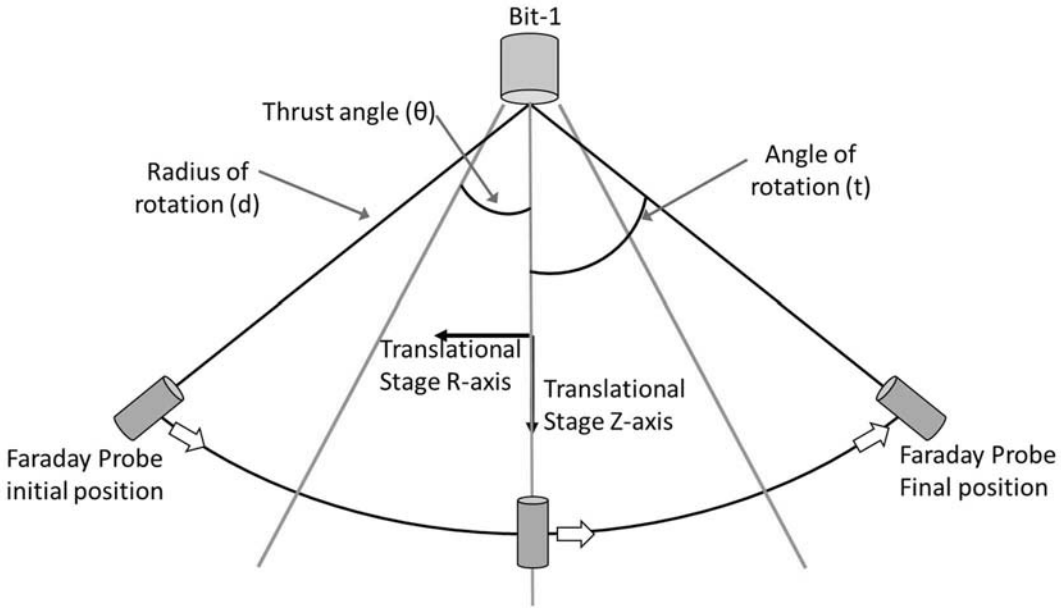

Figure 34. Schematic, Top-down, of the Translational Stage During Faraday Probe Operation

As the translational stage moves in the R- and Z-axes, keeping the Faraday probe at a constant radius, the stage also rotates the probe to always point towards the center of the BIT-1. The data gathered from the Faraday probe will produce a map of the current density.

ExB Probe

The second set of data collected was the species ionization using the ExB probe. The ExB probe used in the experiment was also manufactured by Plasma Controls and is shown in Figure 35.

Figure 35. Plasma Controls ExB probe.

The ExB probe was mounted to the translational stand and placed inside the thrust plume of the BIT-1. When taking measurements, the magnetic field in the probe and the plate separation distance were held constant while the plate voltage was swept from 20 to 60 volts. This caused the ions to be separated according to their respective masses and charge state. An example results graph from Plasma Engineering Laboratory is shown below in Figure 36 [23:4].

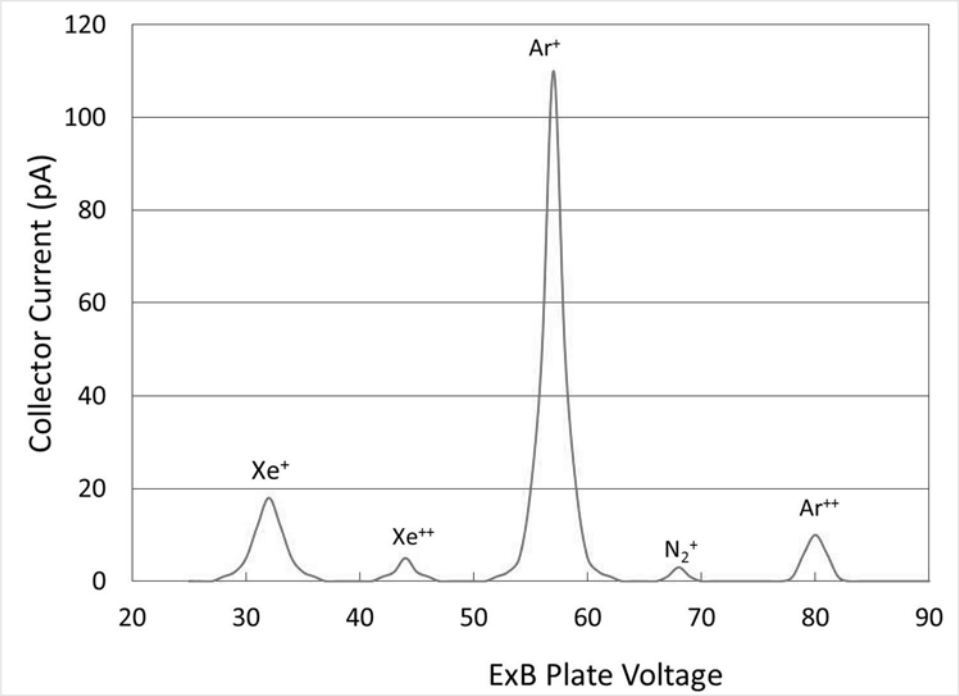

Figure 36. Plasma Engineering Laboratory's Example Data

The experimental results should show similar spikes near the 31 volt and 44 volt locations, associated with singly- and doubly-ionized xenon, respectively. Plotting the resultant current collected verse the voltage swept will illustrate the species ionization of the BIT-1.

Thrust Stand and Final Setup

The Busek torsional balance system was designed to accurately measure micro-newton forces. The BIT-1 ion thruster produces thrust inside the regime of micro-Newton and was, consequently, an excellent choice for accurate measurements. Figure 37 shows the Busek torsional balance system used in the experiment.

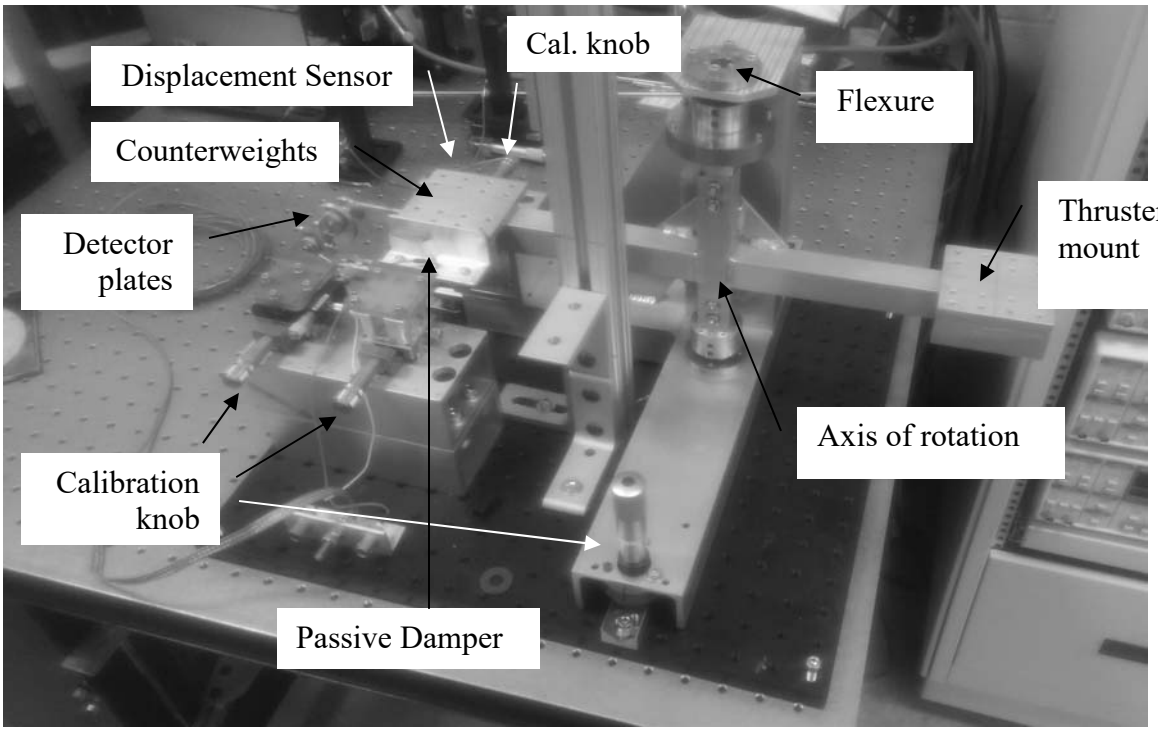

Figure 37. Busek Torsional Balance System

The thrust stand has two mount locations on either side of the rotation axis. One side was where the BIT-1 thruster was mounted and the other side holds the counter balance weights. The flexure, located on top of the axis of rotation, is a spring, linearly converting the applied load into a correlated motion of the stand. The passive damper dampens the movement of the system as a force is applied. The detector plates provide a measurement for the distance in the force calibration equation which is described below. Lastly, the laser displacement sensor measures the distance to a mirror attached to the torsional balance arm, preset to 1 mm for repeatable measurements.

Inside the vacuum chamber, the BIT-1 was attached without the CNTFE cathode to the Busek torsional balance system to gather accurate thrust data. The neutralizing

cathode was attached independently from the thruster as not to affect data collected yet close enough to neutralize the ion cloud.

Along with the thrust stand, Busek provided a calibration equation which relates an input voltage and associated displacement to the output thrust. This is shown below in Equation 32 and a graphical example, created from a Busek example case with a 1 mm separation between the detector plates, is shown in Figure 38,

$$F_{cal} = \frac{(1.262 * 10^{-9})(1 + 1.138.1 * \mathrm{d})V_{Cal}^2}{\mathrm{d}^2} \tag{32}$$

where F_{cal} is the calibration force in micro-newtons, V_{cal} is the voltage in volts, and d is the distance between the electrodes in meters.

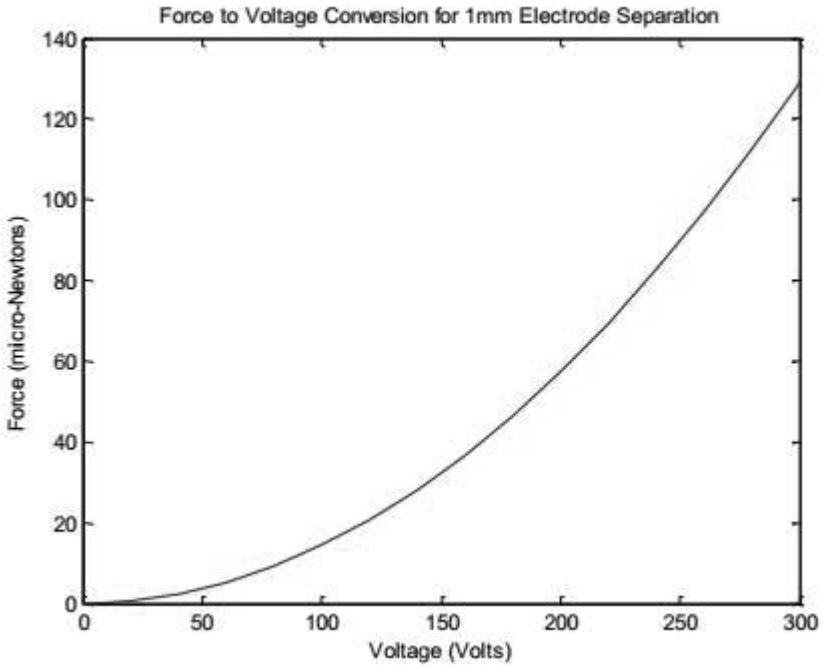

Figure 38. Relationship Between Voltage Output by the Thrust Stand and Corresponding Thrust from Busek's Example of 1 mm Separation [6:54]

IV. Troubleshooting

Chapter Overview

This chapter provides an overview of the experiment troubleshooting process for each of the tests up to successfully igniting the thruster. Several unrecorded tests are not discussed due to malfunctions occurring before any information could be gathered. These malfunctions include pressure leaks inside the vacuum chamber, electric arcing in-between the thruster BNC connecting wires, and miscellaneous malfunctions in the vacuum chamber operations. The thruster was successfully started twice through the entire course of testing. An image of the thruster working is shown below in Figure 39. Additionally, due to time constraints, the ExB probe was never used. The time instead was used for the thrust stand data collection.

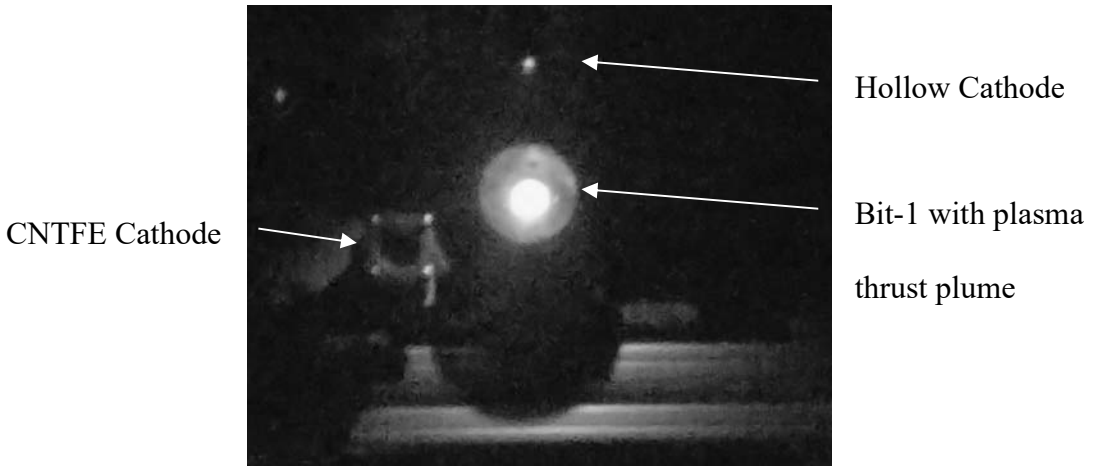

Figure 39. Image of BIT-1 Ion Thruster Operating in AFIT's Vacuum Chamber During the Sixth Test

Initial Experimental Setup, Tests One through Three

The initial experimental setup had numerous fundamental issues. Due to the nature of the issues and when they occurred, they had to be addressed one at a time.

First Experimental Test

The first experimental problem occurred during the first time the vacuum chamber was pumped down. The flow controller was set to 0.08 sccm and steps 3 through 10, from the Operating Requirements and Starting Procedure section of Chapter III were completed (Note: Steps 1 and 2 were added in a later test). No illumination was emanating from any component of the thruster. After watching the thruster for about 1 minute, a large blue flash (ionizing propellant) behind and above the thruster was noticed to occur occasionally at non-specific intervals. This flash was assumed to be caused by two issues. First, propellant had to be leaking from behind the thruster. Most likely, this was a result of pipe adapters incorrectly or insufficiently tightened. Second, the leaking propellant had to have an arcing source to light. The electric wires attached to the thruster were inspected for any damage or location in which electric discharge occurred. There were no visible scorch marks found. The propellant line issue was addressed by disassembling, inspecting, cleaning, and reassembling the propellant lines while ensuring proper tightness was applied to each component. Although no damage was found, the electric wires were wrapped in insulating Kapton tape to prevent unwanted discharge.

Second Experimental Test

During the second test, the thruster did not have issues similar to the first experiment. The modifications to the experimental setup appeared to have fixed the propellant leak issue, and no visible electric arcing occurred throughout the test. Similar

to the first test, the flow controller was set to 0.08 sccm, and the startup steps 3 through 10 were completed. For the period of the polarity switch in step 10, the acceleration grid holes dimly illuminated. This was assumed to be electrons colliding with propellant molecules as they were being pulled into the thrust chamber. After the polarity was returned to a negative voltage, the illumination immediately subsided, and the BIT-1 did not start. The two-second polarity switch was attempted several times with no changes but the BIT-1 never started.

All the equipment was checked for malfunctions or issues. The flow controller displayed a VOV error meaning propellant was flowing to the BIT-1, but the value displayed on the flow controller screen may not have been the value set [18]. Omega, the manufacture of the flow controller, was contacted for support. Their technician suggested the main issue to be the improper configuration of the flow controller for a vacuum application. The technician described the troubleshooting process required to fix the issue and also provided a link to a YouTube video by Alicat Scientific, Inc. [18]. The video illustrated the step-by-step procedure to disassemble and reassemble a similar flow controller into the proper vacuum application setup [24]. These procedures were followed and the reconfigured flow controller was reattached to the experimental setup.

Third Experimental Test

The third test, with the properly configured flow controller, resulted in a similar outcome to the second test. The acceleration grids showed illumination but the plasma generation of the BIT-1 did not activate. The equipment was then checked and found to be properly configured. The flow controller was tested to ensure the propellant was actually flowing by closing the xenon supply tank and observing the pressure dropping in

the supply line. This result implied the propellant was flowing into the vacuum chamber. Since the thruster did not ignite, it was theorized there was still a propellant leak inside either the propellant lines, the adapters, or the BIT-1 ion thruster.

The vacuum chamber was returned to normal atmospheric pressure and the vacuum propellant lines were checked for pressure leaks. This was accomplished by first removing the flow controller from the propellant lines as well as removing the adapter assembly from between the end propellant line and the thruster. Next, a pressure gauge was attached to the end of the propellant line and the line was pressurized with krypton gas. The gas was then shut off and the pressure gauge was observed for any decrease in pressure. No reduction of pressure was noted during a five-minute test. The adapter assembly, shown below in Figure 40, was disassembled and inspected for any joint or thread flaws.

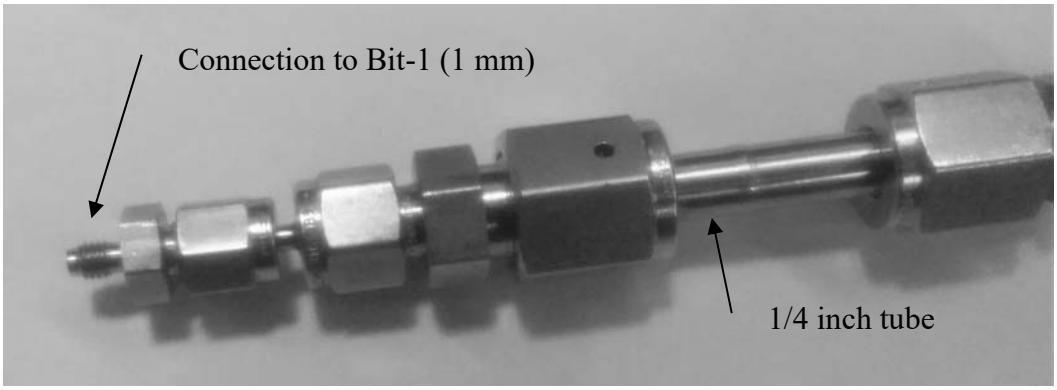

Figure 40. Propellant Tube Adapters between Propellant Line and Thruster Line

Each component appeared to be functioning properly. Small amounts of high vacuum silicon grease were applied to the outer threads to improve the pressure seal.

Intermediate Experimental Setup, Tests Four through Six

Prior to the fourth experimental test, Tsay, from Busek, was contacted for support in starting the BIT-1 Thruster. Tsay supplied several troubleshooting methods to implement. The first and easiest to address was associated with the acceleration grid's polarity switch. During the polarity switch, he explained, the acceleration grid's positive power supply should be displaying a current of 1 mA [25]. The current on the power supply changes based on how many seed electrons are attracted to the acceleration grid. Also, Tsay provided a picture taken at Busek's laboratory of the BIT-1 thruster during starting operations for reference. A similar image is shown in Figure 41 which was taken by Muilenburg during his research.

Figure 41. A BIT-1 Ion Thruster During Operation at Busek from Muilenburg [6:92]

Figure 41 shows the illumination of the sides of the BIT-1 resulting from the plasma generation inside. The picture from Tsay gave an illumination comparison point for reference during the experiment. Using recorded data from tests one through three, the power supply displayed 0.1 mA during each polarity switch. This meant the hollow cathode was not close enough to provide sufficient seed electrons for the plasma generation to start. As a result of this information, the experimental setup was reconfigured, transitioning the hollow cathode mount from the Hall thruster to directly above and in front of the BIT-1.

In addition to contacting Tsay, the procedure for starting the thruster was also evaluated. At this time, an assumption was made that the work to check and prevent any propellant leaks was successful. A new theory was developed regarding the way the propellant flowed inside the tubes after it left the flow controller. From the flow controller to the entrance to the BIT-1 is about 15 feet of 1/4 inch diameter tubing. Also, between the propellant line and the thruster are the propellant tube adapters which reduce the tubing diameter. For starting operations, the flow controller is set to the max BIT-1 operational setting of 0.08 sccm. The theory developed was the propellant needed an initial higher flow rate to overcome the length of propellant line and any pressure loss of the adapter diameter reduction. Therefore steps one and two were added to the starting procedure to allow propellant to fully populate the propellant line up to the thruster.

Forth Experimental Test

The reconfigured experimental setup was then tested a fourth time, proceeding through steps 1 through 9 of the startup procedure. During step 10, the current on the acceleration grid's positive power supply was noted to be between 1.3 and 3.0 mA,

stabilizing on 1.6 mA after one second. This signified the new configuration of the experimental setup successfully reached the 1 mA requirement to start the plasma generation. Then step 10 was repeated several times. Twice, step 1 was repeated to ensure propellant was sufficiently provided. The illumination inside the grids during step 10's polarity switch was brighter than the previous setup. However, the BIT-1 did not ignite.

Fifth Experimental Test

The next task was to eliminate the flow controller and propellant flow as the leading issue for the BIT-1. Further discussion with Tsay, led to a supplementary understanding of the BIT-1's operational range.. Tsay provided the maximum allowable propellant flow, 0.15 sccm. The fifth experiment started by progressing through the startup procedure, steps 1 through 10. After the polarity had been switched the first time, the amount of propellant was increased by 0.01 sccm after each polarity switch. In between the propellant flow increases, the thruster was checked for plasma generation. When the maximum flow was reached, the polarity switch was tried several times. Also, step 1 was repeated to ensure propellant was in the lines. Throughout the test, the thruster did not start and there was no additional illumination (signifying plasma generation).

After the propellant had been eliminated as an issue with the plasma generation, Tsay suggested disassembling the BIT-1 to inspect the internal components for damage. Figure 42 show the BIT-1 thruster before disassembly, inspection, and repair work.

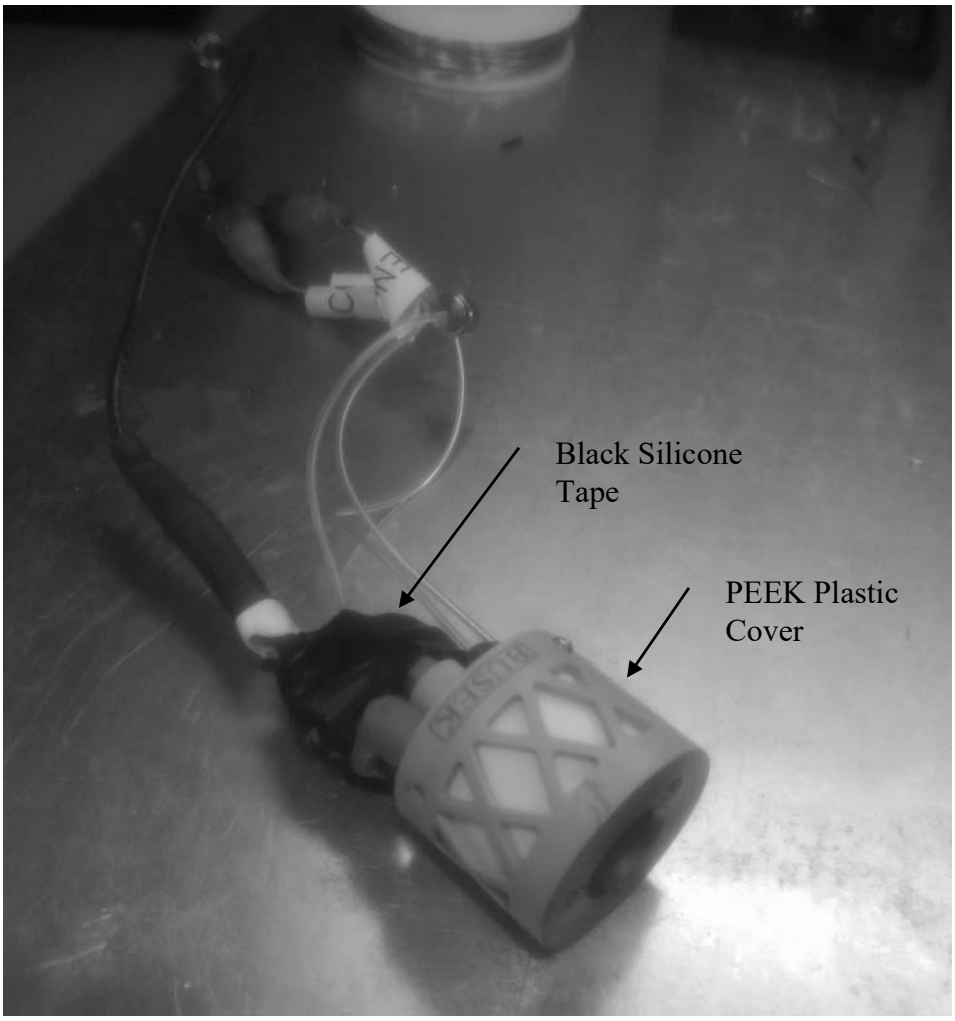

Figure 42. BIT-1 Ion Thruster Before Disassembly

The first step in the disassembly process was to remove the outer protective PEEK plastic cover. The BIT-1 with the cover removed is shown below in Figure 43.

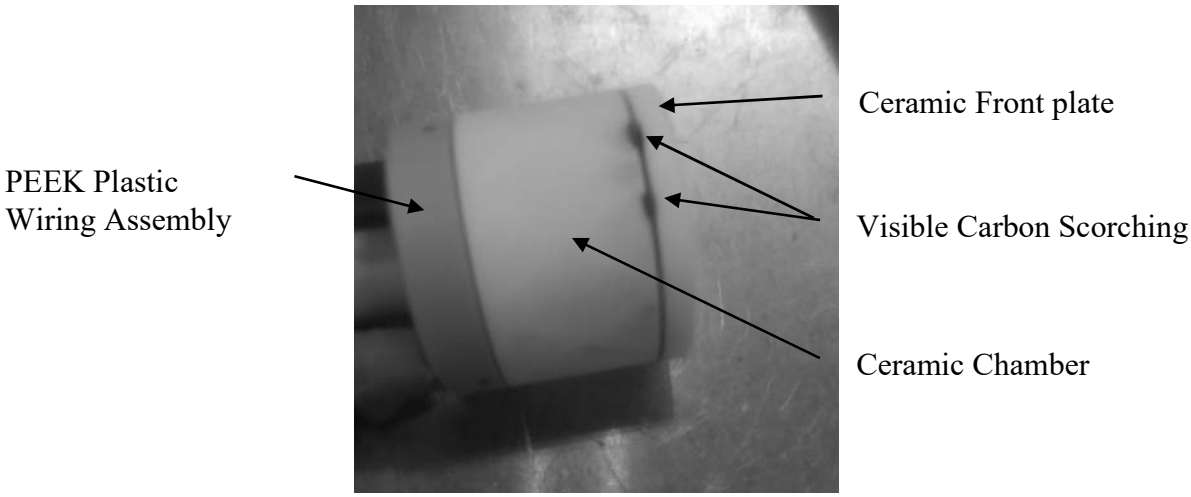

Figure 43. BIT-1 without PEEK Plastic Cover

Once the cover of the BIT-1 was removed, carbon scorching was clearly visible on the outside between ceramic front plate and the chamber. The next step was to remove the black silicone tape securing the wiring and propellant tube and then remove the propellant tube. Figure 44 and Figure 45 shows the BIT-1 with the silicone tape removed and the propellant tube with the internal gasket.

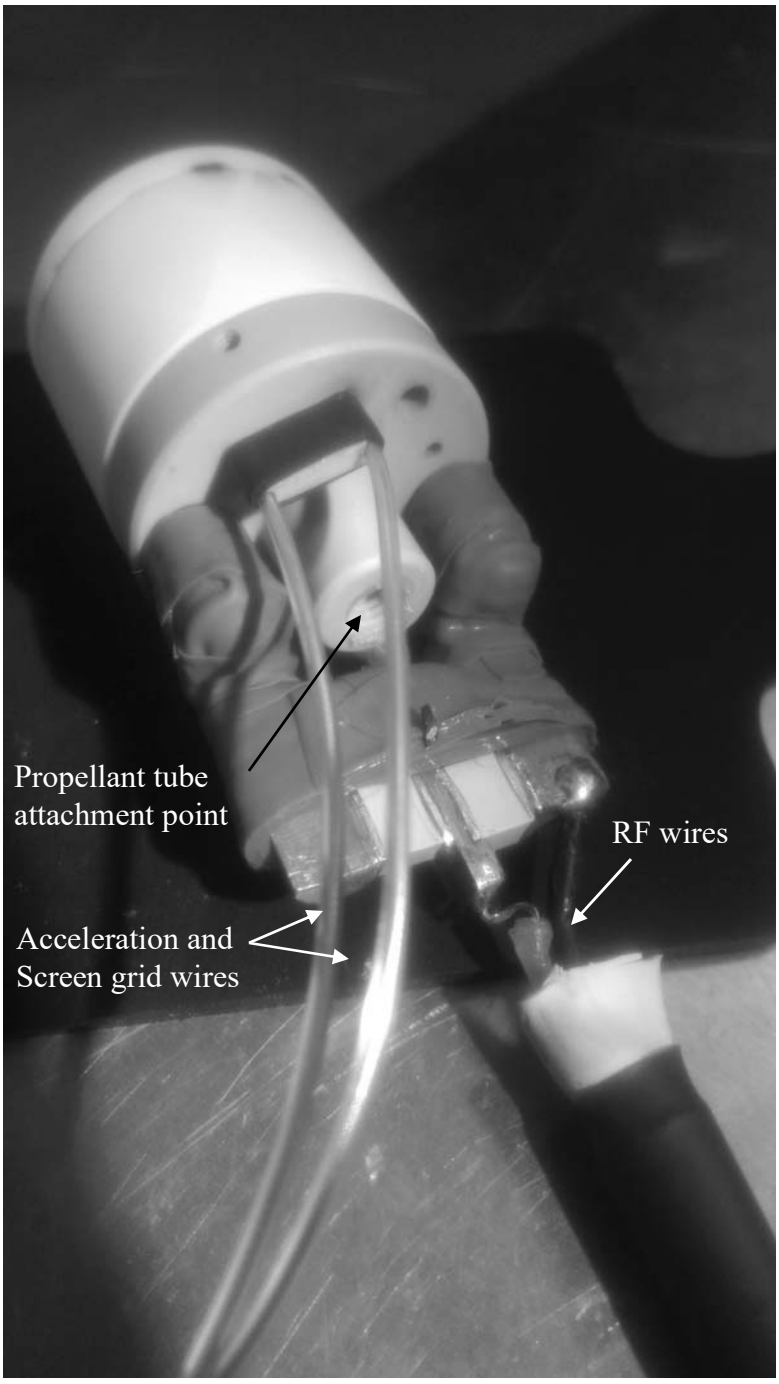

Figure 44. Back of the BIT-1 without Silicone Tape and the Propellant Tube

As seen Figure 45, the soldering points for the RF connection and grid wiring appeared to be in good condition. At this point when the BIT-1 was disassembled, all of the components and associated wiring was tested using a multimeter's continuity function. All the BIT-1's components showed good continuity to the connection wires and no cross-continuity in-between wires.

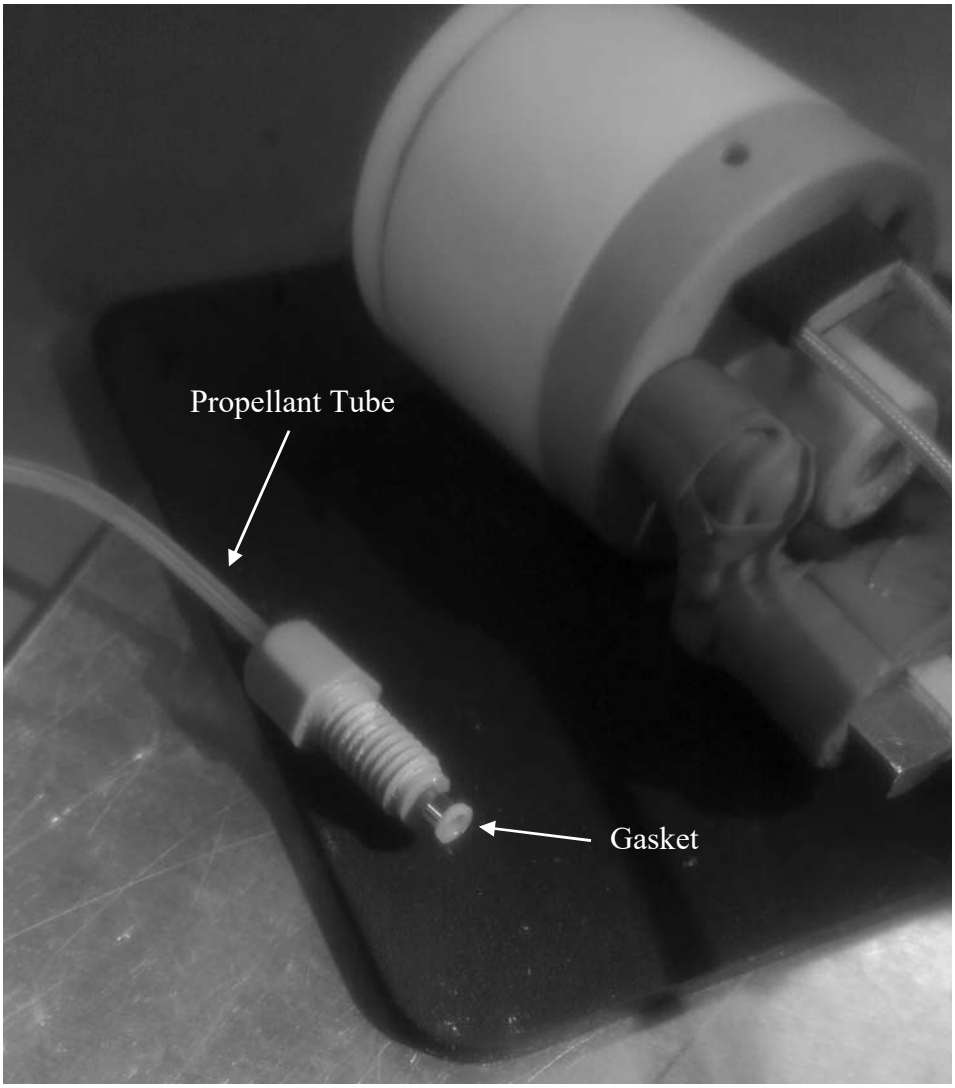

Figure 45. BIT-1's Propellant Tube and Gasket

One previous failure mode of other BIT-1 ion thruster's, mentioned by Tsay, was the gasket at the end of the propellant tube melting [25]. Any deformation of the gasket would cause propellant to flow improperly. After removal and inspection, as seen in the figure above, the propellant tube and the gasket from the BIT-1 appeared to be undamaged. After that, the next step was to remove the front ceramic plate and inspect the grids. Figure 46 shows the BIT-1 after the front ceramic plate was removed.

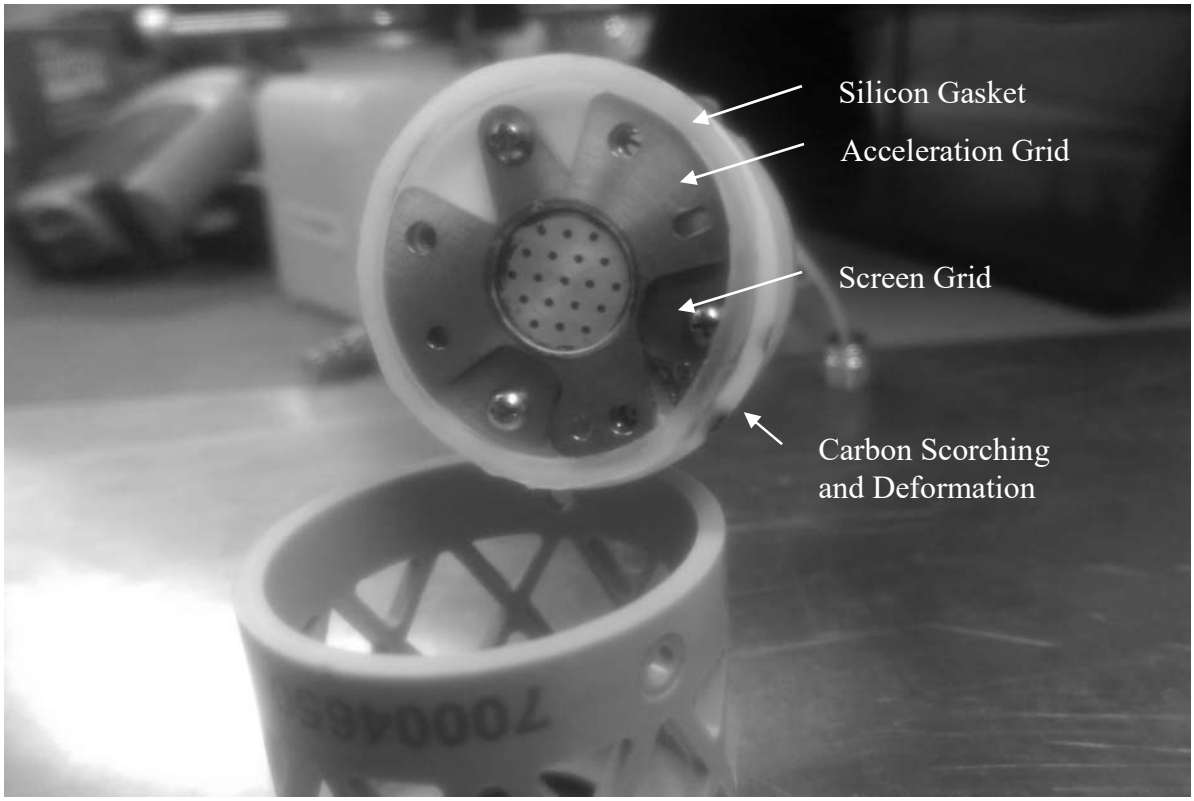

Figure 46. BIT-1's without the Front Ceramic Plate

Once the front plate was removed, internal damage to the BIT-1 was revealed. As seen in the figure above, internal carbon scorching is visible from the outer edge onto the screen grid. In addition, the internal silicone gasket was deformed, resulting in an

insufficient seal between the ceramic front plate and the chamber. A magnified image provides additional detail in Figure 47, with the acceleration grid rotated out of alignment.

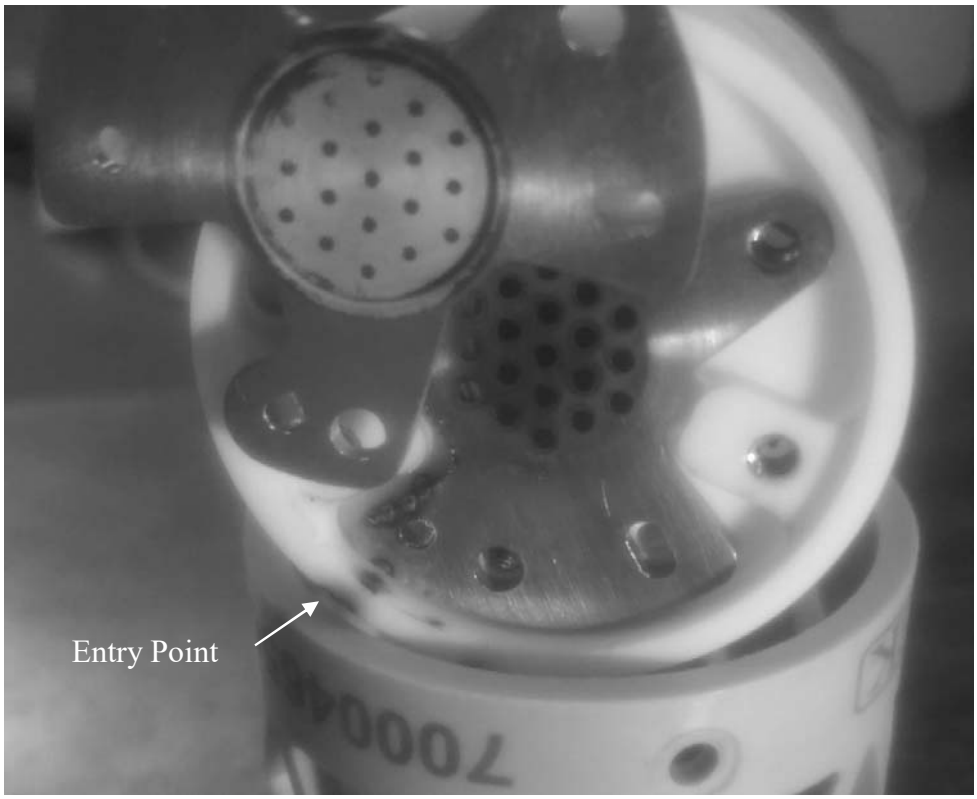

Figure 47. Magnified BIT-1 with a Rotated Acceleration Grid

The above figure shows the main malfunction point found during disassembly. Through discussion with Tsay, it was theorized the gasket did not seal properly which allowed an entry point for seed electrons. Typically, the seed electrons have to flow through the acceleration grid, which aligns them to flow into the chamber. This supplementary entry point for seed electrons allowed one of two possibilities to occur. The first theory is plasma was formed outside the chamber and protection of the radio

frequency generated an electromagnetic field. The second theory is the particle density between the grids increased from the seed electrons and was enough to allow the 2 KV potential to arc between the grids. In either case, the best option to prevent further problems is to inhibit the seed electrons from being pulled in improperly.

After the main problem was found, Tsay suggested removing the carbon scorching with sand paper [25]. Therefore, the BIT-1 was first externally cleaned with isopropyl alcohol and then the carbon deposits were meticulously removed with 1500 grit sand paper. Figure 48 shows the cleaned BIT-1.

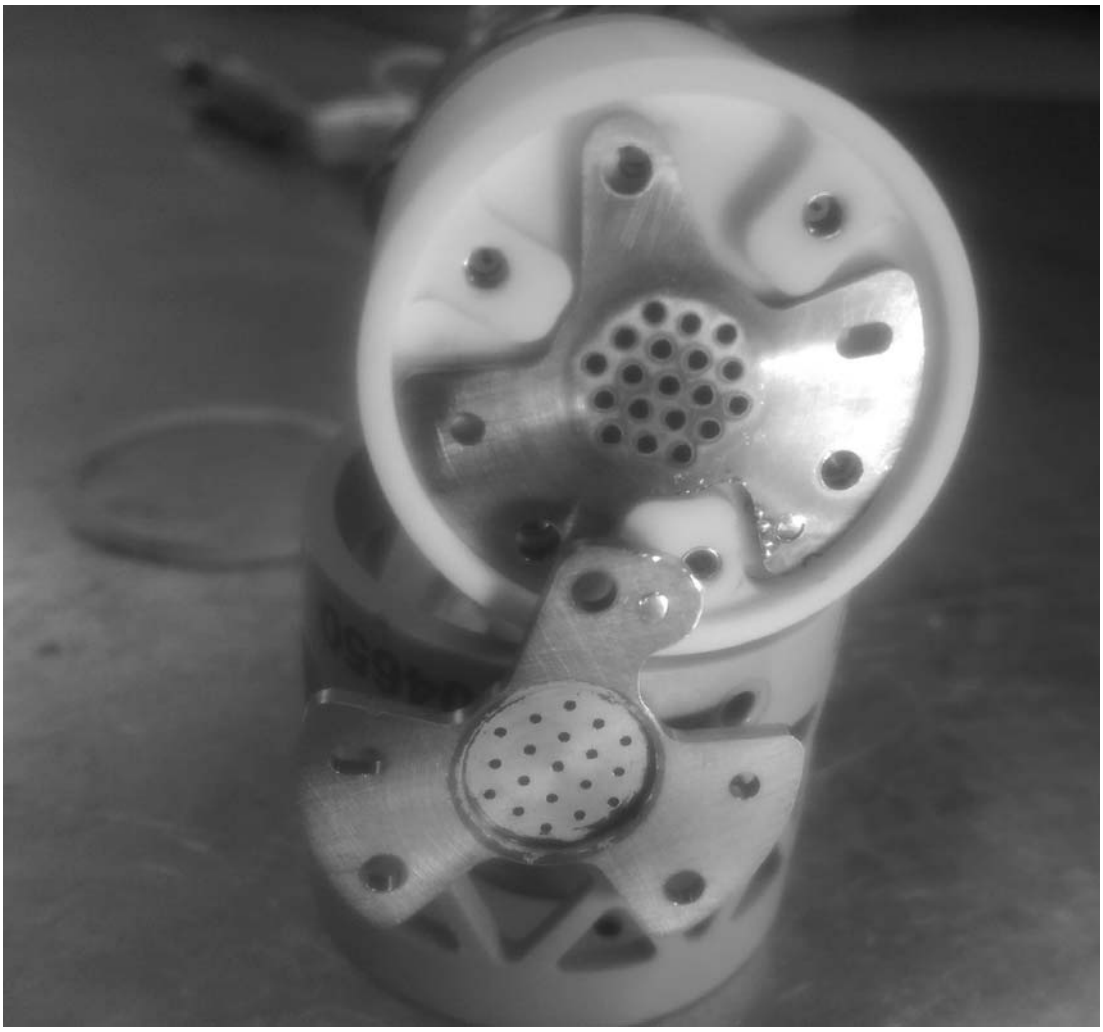

Figure 48. Cleaned BIT-1 Ion Thruster

The deformation in the silicone gasket, however, was unrepairable and due to time constraints could not be replaced. Tsay stated the gasket was custom made to fit the BIT-1 and therefore could not be directly ordered. Instead, to ensure this problem would not happen again, the reassembled thruster was wrapped in self-fusing silicone tape, thereby insulating the entire thruster. Below, in Figure 49, the BIT-1 ion thruster is shown wrapped in silicone tape.

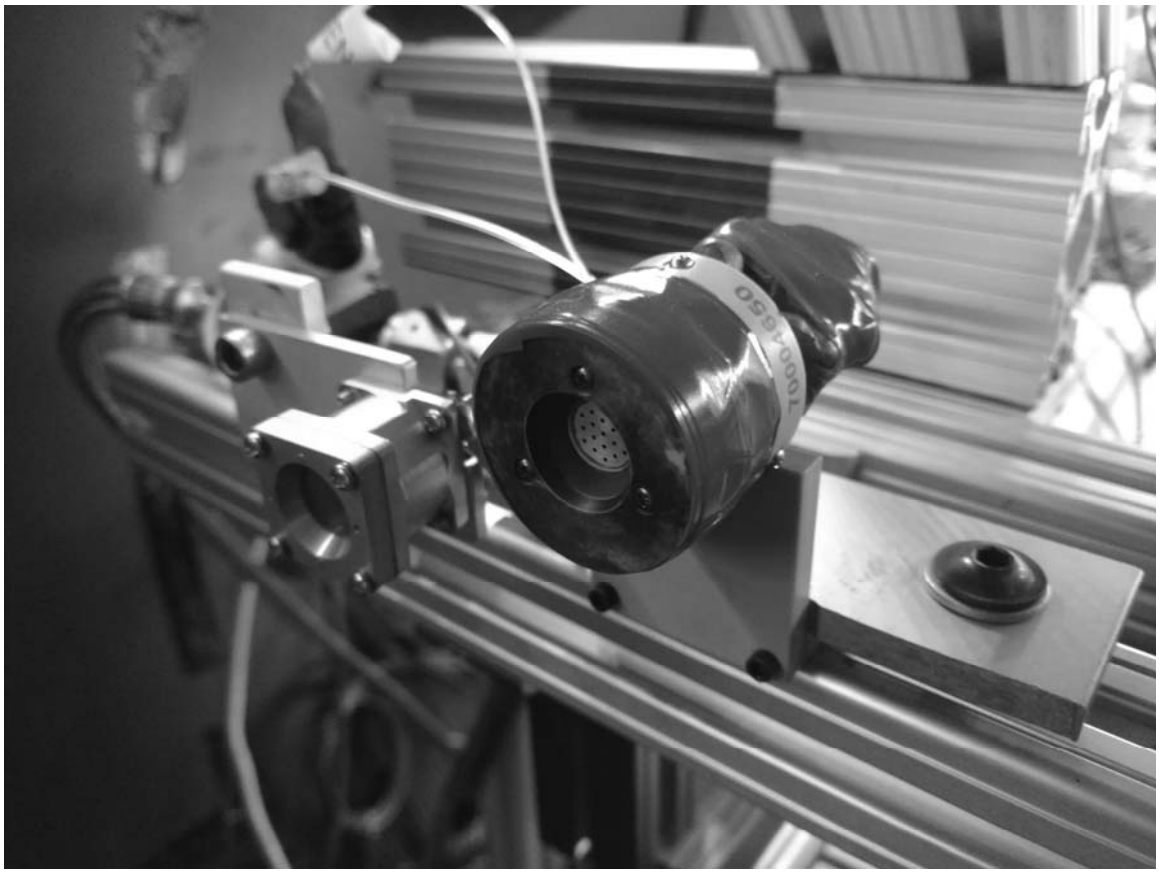

Figure 49. Repaired and Mounted BIT-1 Ion Thruster Wrapped in Silicone Tape

Sixth Experimental Test

Once the final repair work was completed, the thruster was tested a sixth time. The complete setup is shown below in Figure 50.

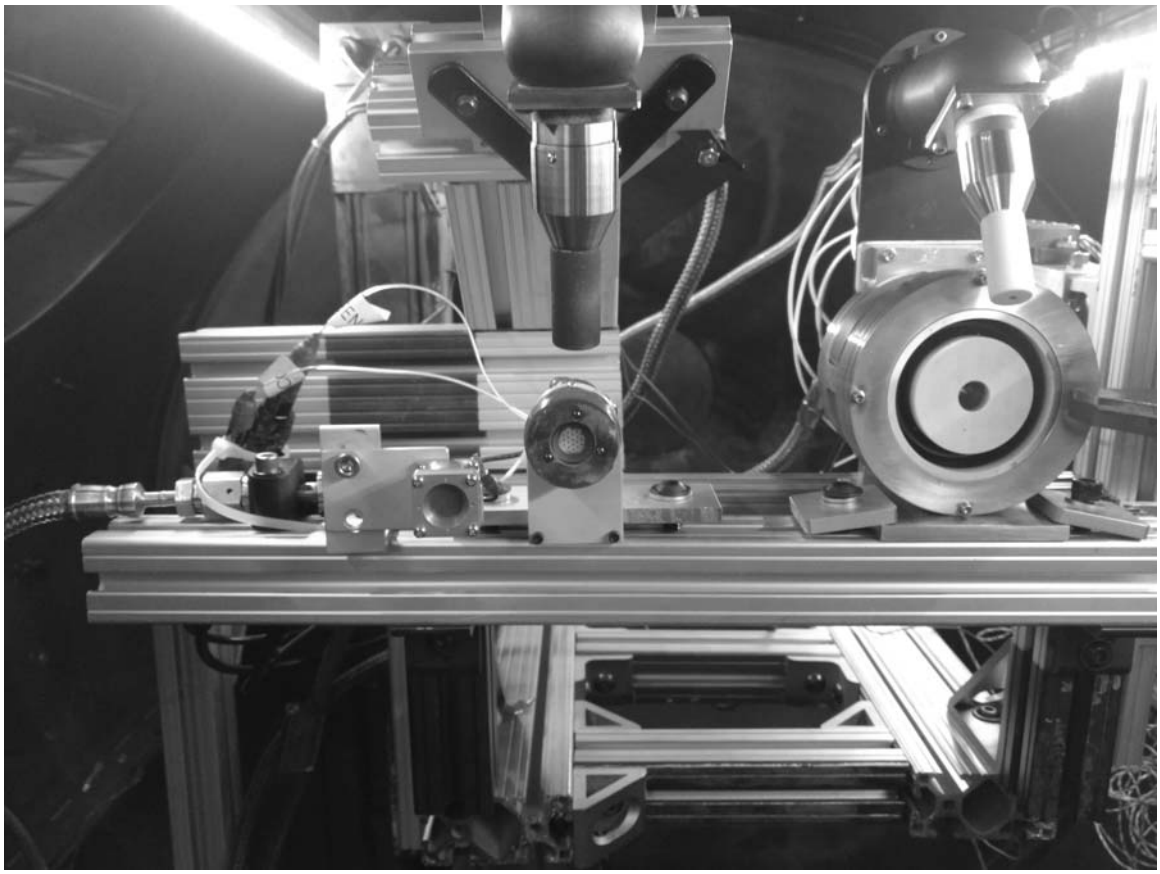

Figure 50. Sixth Experimental BIT-1 Ion Thruster Test Setup

The startup steps 1 through 10 were completed. Figure 51 shows a photo of the BIT-1 thruster taken during the polarity switch.

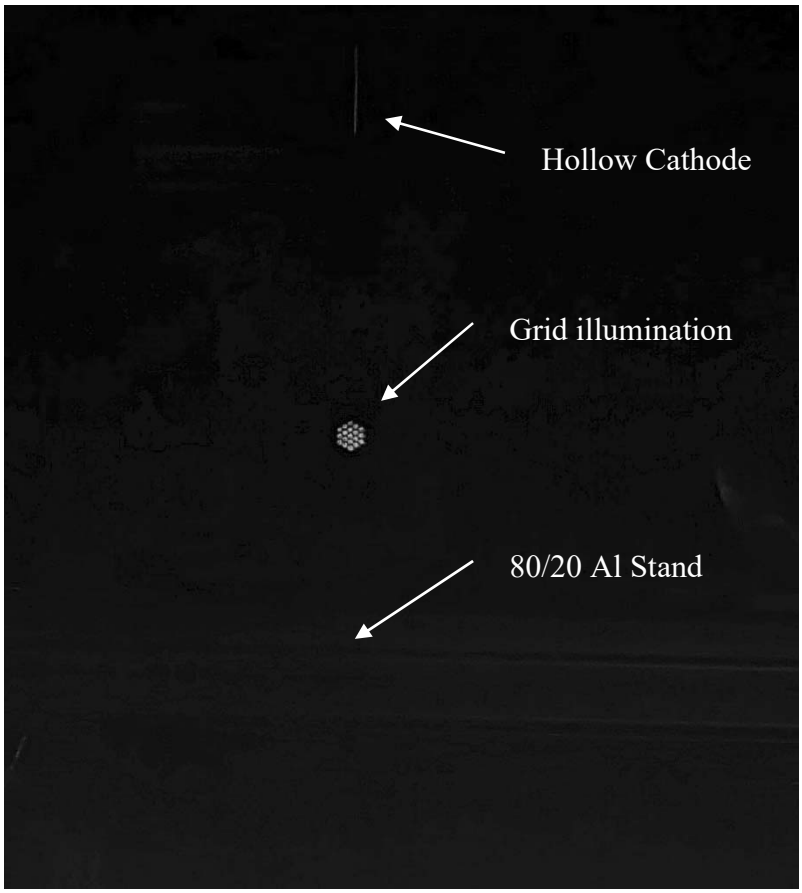

Figure 51. BIT-1 Grid Illumination Prior to Full Plasma Generation

The BIT-1 ion thruster successfully ignited after the polarity switch. Figure 52 shows the BIT-1 during operation.

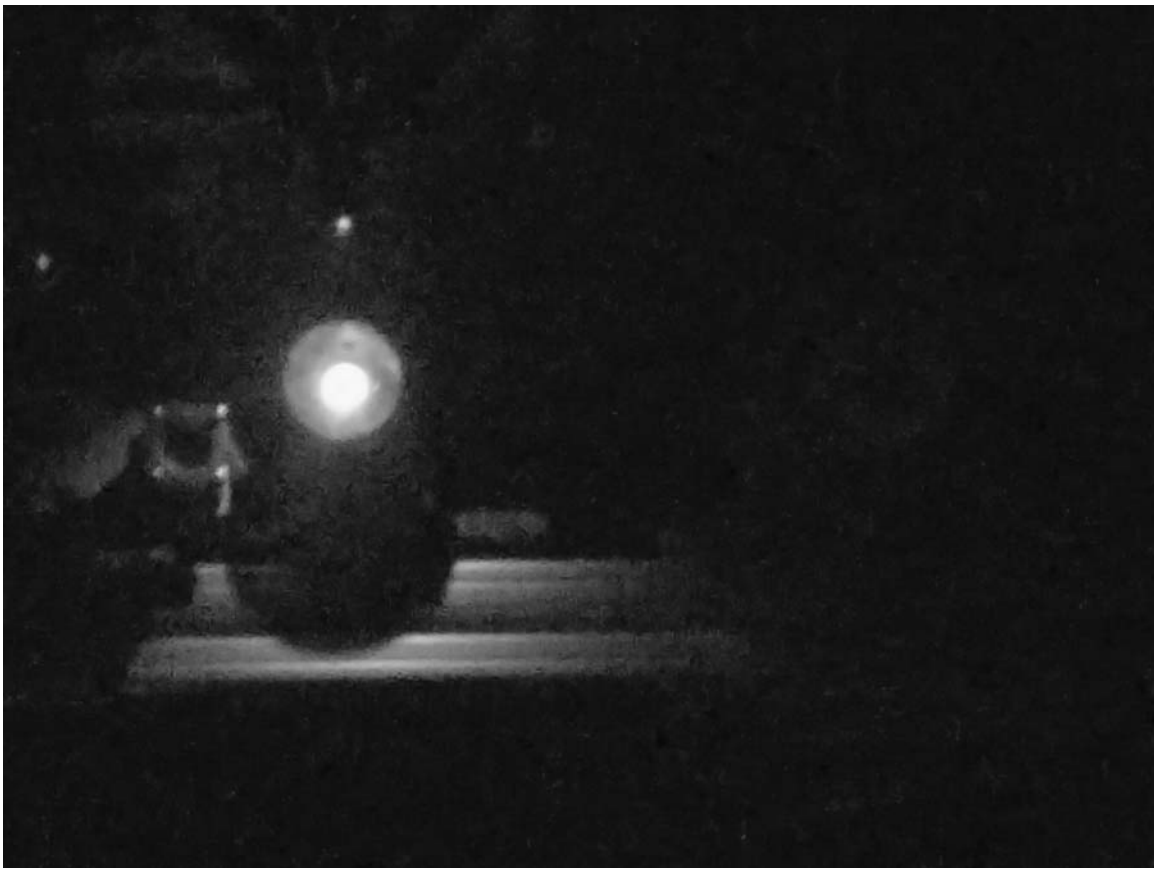

Figure 52. BIT-1 Ion Thruster During Operation at AFIT

The BIT-1 operated initially for approximately 4 minutes before unexpectedly turning off. After the BIT-1 had turned off, step 1 was repeated to refill the propellant lines. Then step 10 was repeated and the BIT-1 reignited. The second time, the BIT-1 operated approximately 10 minutes before again unexpectedly stopping, during which the Faraday probe data was collected. The theory for the BIT-1's short operational time was the propellant lines were too long.

After the sixth test, the propellant piping was reconfigured. The flow controller was attached as close as possible, approximately 1 foot, to the vacuum chamber. This

reduces the propellant line to the length of approximately 8 feet. This new flow controller setup was tested with seventh test.

Thrust Stand Experimental setup

The final stage of the research was setup along with the Busek's Torsional thrust stand. Three iterations of the torsional thrust stand experimental setup were required for recording thrust data.

Seventh Experimental Test

The seventh experimental setup test on the thrust stand was designed with the hollow cathode roughly 3 inches away and pointing down and away from the thruster at about a 45° angle. Figure 53 shows the seventh experimental setup.

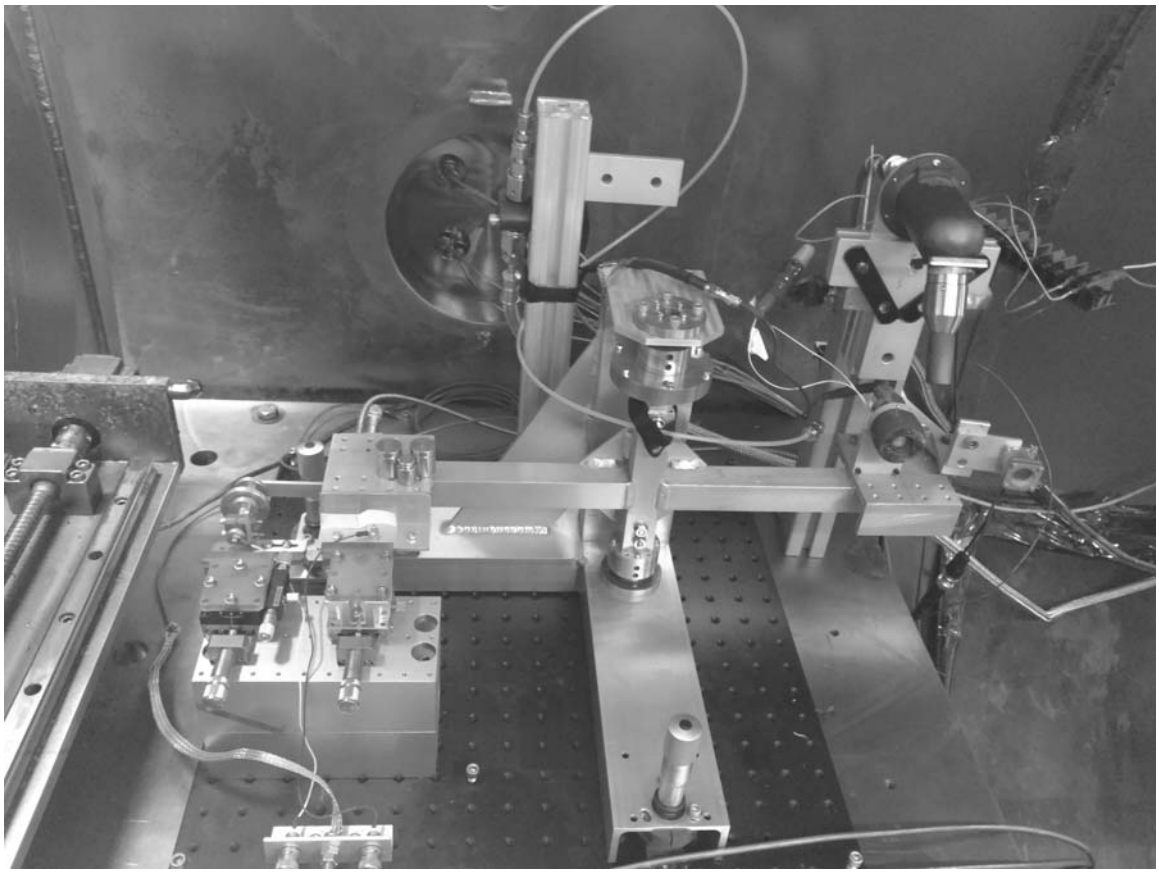

Figure 53. Preliminary Thrust Stand Experimental Setup

This setup proved to be faulty. Steps 1 through 10 were completed to start the thruster. During the polarity switch, the acceleration gird's positive power supply displayed 0.16 mA of current. The amount of seed electrons being pulled by the acceleration grid did not reach the 1 mA required to start the thruster. The hollow cathode was too far away and pointed away from the thruster. The experimental setup was then redesigned to be similar to the successful experimental setup.

Eighth Experimental Test

The eighth experimental setup replaced the hollow cathode mount to the same angled 80/20 aluminum component. This redesign allowed the thruster to be in nearly the

same height, angle, and distance away as the successful experimental setup. The second experimental setup on the thrust stand is shown below in Figure 54.

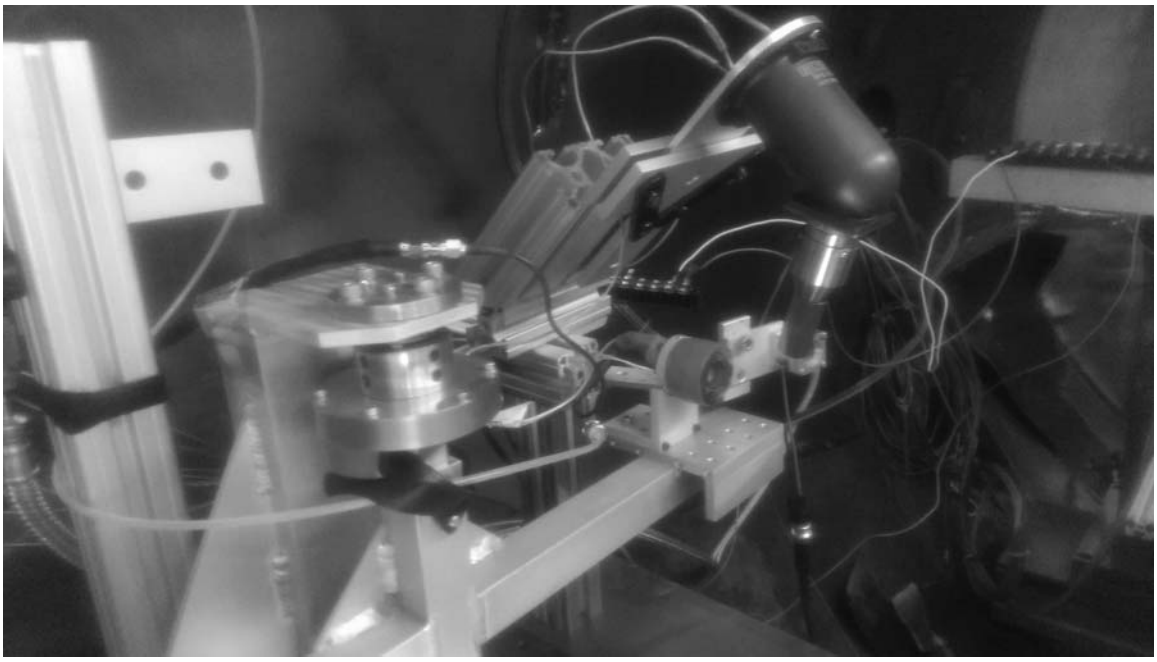

Figure 54. Second Iteration of the Thrust Stand Experimental Setup

For this test, the hollow cathode had issues starting and required an additional hour of heating to start. This setup was then tested and steps 1 through 10 were completed. During the polarity switch, the acceleration gird's positive power supply displayed only 0.6 mA of current. Again, this did not reach the minimum current of 1 mA to start the plasma generation. All the equipment was inspected for faults and errors. This experimental setup was very similar to the successful setup. Therefore, issues with the hollow cathode operation were the most likely cause of low grid current. Consequently, the test was stopped and the hollow cathode was left to sit inside the vacuum overnight. The additional time inside the vacuum chamber improves the function of the hollow

cathode by removing it from an oxygen environment, allowing any contaminants to be removed.

The setup was tested again the following day and the hollow cathode started quickly. Steps 1 through 10 were completed. Similarly, during the polarity switch, 0.6 mA of current was displayed. The most likely cause was reduced hollow cathode electron production. To counter the reduction of electrons, the experimental setup was redesigned.

Ninth Experimental Test

The ninth experimental setup on the thrust stand moved the hollow cathode to about 1 inch away from the thruster and pointing at the grids. Figure 55 shows the ninth and final experimental setup from the side.

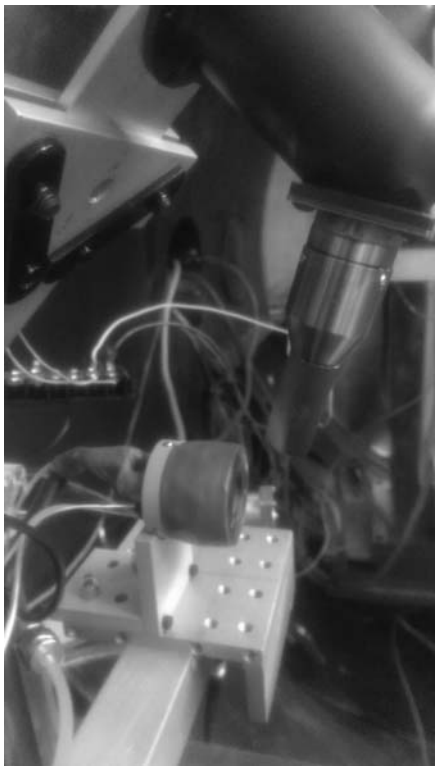

Figure 55. Successful Thrust Stand Experimental Setup

This redesign ensured the hollow cathode would be close enough to provide the required amount of seed electrons for plasma generation. The setup was then tested and steps 1 through 9 were completed. During the polarity switch of step 10, the power supply overloaded and "tripped" the internal circuit breaker to protect the circuit from excess current. This was a result of both the hollow cathode's close distance and the +200 volts being applied to the grids. The power supply voltage was adjusted and tested until a current of 1.6 mA (similar to the successful test) was reached. The appropriate voltage for this setup was found to be 75 volts which resulted in 1.7 mA during the polarity switch.

After the hollow cathode and the power supply voltage issues had been rectified, steps 1 through 10 were complete. The thruster did not start and grid illumination was present during the polarity switch. All the equipment was inspected for faults and errors. The startup procedure was attempted three more times, increasing the flow rate sequentially from 0.10, 0.12, and then 0.15 sccm. Grid illumination was present on each test. Despite this work, the thruster did not start.

The vacuum chamber was kept at vacuum pressures and the test was reattempted the following day. Prior to starting the thruster, all the equipment outside the vacuum chamber was inspected to confirm no errors were present. All non-essential vacuum chamber equipment were power cycled and reset to ensure a fresh starting point. Steps 1 through 10 were accomplished. During the polarity switch, grid illumination was present but the thruster did not start. Many attempts were then tried to start the thruster by varying the flowing list independently and in combinations:

- Flow rates: 0.08 to 0.15 sccm,

- Acceleration grid negative voltage: -50 to -200 v (steps of -50 v),
- Acceleration grid positive voltage: +25 to 100 v (steps of +25 v),
- Screen grid voltage: 900 to 1500 v (steps of +100 v), and
- High flow rate of 0.6 sccm for 5 minutes.

None of the attempts proved to be successful. Consequently, Tsay was contacted for support in troubleshooting the thruster.

Through the communications with Tsay, the most probable reason for the inability to start the thruster is a leak somewhere inside the propellant line. Before and after the testing, the BIT-1's propellant lines were checked to ensure a good connection. This means the most likely location for a leak is internal to the BIT-1. Tsay discussed several known issues Busek has found through their testing including melted plastic blocking the propellant line, clogged injector, and a loose compressive seal [25]. To troubleshoot these issues the BIT-1 would require another full disassembly and inspection. Due to time constraints, this cannot be accomplished. However, Tsay was able to provide replacement propellant lines and PEEK plastic fittings for future testing of the BIT-1 ion thruster.

IV. Analysis and Results

Chapter Overview

This chapter summarizes the data collected and the corresponding analysis completed during the research. The Faraday probe data, collected during the only operational window long enough for data collection, is discussed. Next, the thrust stand verification test is reviewed and the data collected is evaluated. In addition, the calibration equation for the torsional thrust stand is evaluated.

Faraday Probe Data

During the 10 minutes of operation of the sixth test, the Faraday probe data was collected at the starting operational conditions listed in the Operating Requirements and Starting Procedure section of Chapter III. Due to time constraints, the Faraday probe data was not taken at the nominal operating conditions. For this experiment, the radius of rotation chosen was from 40 and 80 cm and the angle of rotation was from -60 to 60 deg. The data was collected every 2.5 degrees through the 120-degree arc and increasing the radius by 10 cm each arc. Figure 56 below shows the path the translational stage took while rotating the Faraday probe. Each dot corresponds to a location of data collection.

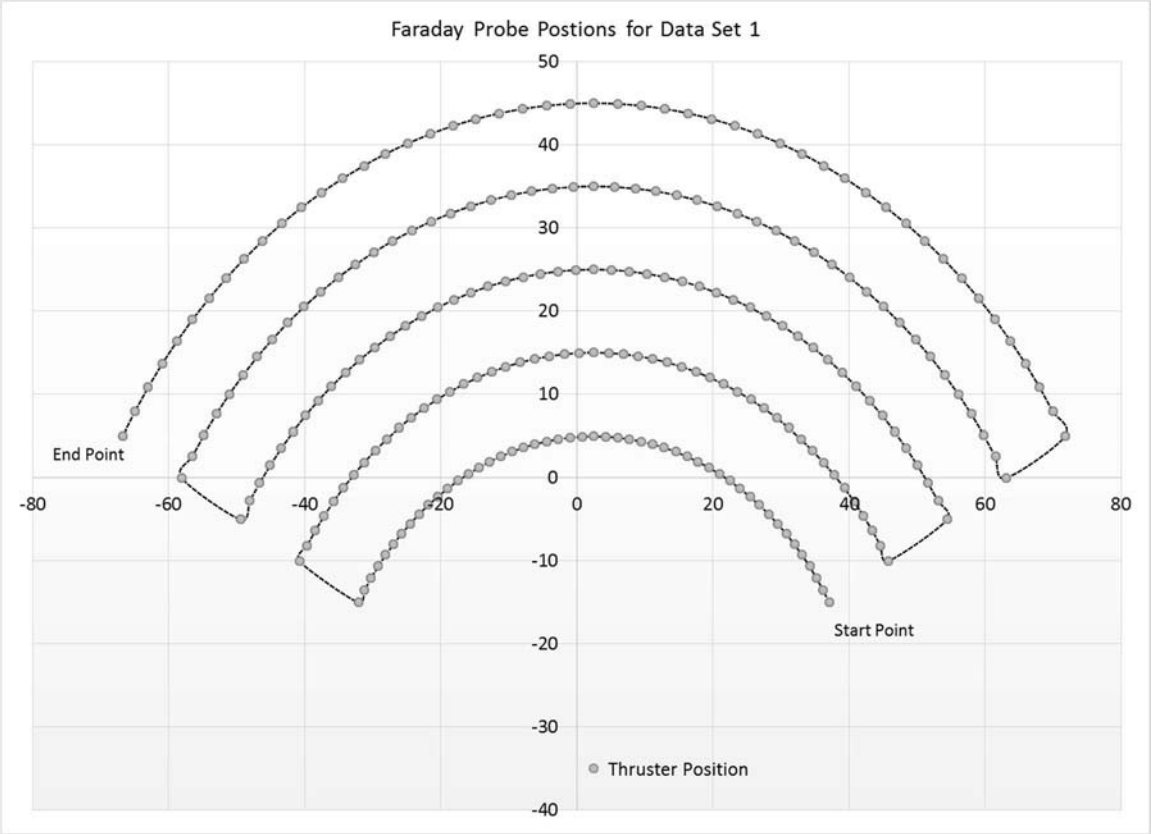

Figure 56. Faraday Probe's Path on the Translational Stage for the First Data Set

Two sets of data were recorded. The first set of data collection was through the full radius range of 40 to 80 cm. The second set of data collection was through the radius range of 40 to 60 cm. The second set of data is shown in Appendix A.

The Faraday probe data recorded was not as expected. Below, in Figure 57, the graph of the calculated current density versus the angle through each radius is shown.

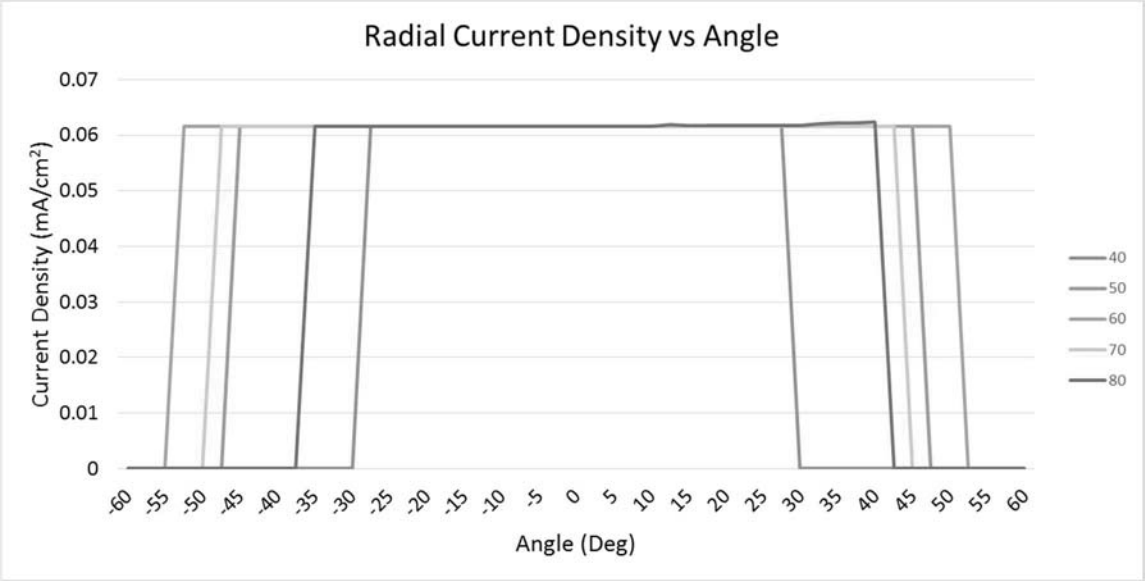

Figure 57. Calculated Radial Current Density Data

The current density was calculated using the probe data collected and Equation 31. Instead of an approximately Gaussian distribution curve centered in-line with the thruster, the values for the current density were almost constant or zero throughout the entire angle translation. Each radial distance also showed approximately equal current density. This is also unexpected because the magnitude of the current density should decrease as the radial distance increases. Figure 58 shows the data in a 3D current density map.

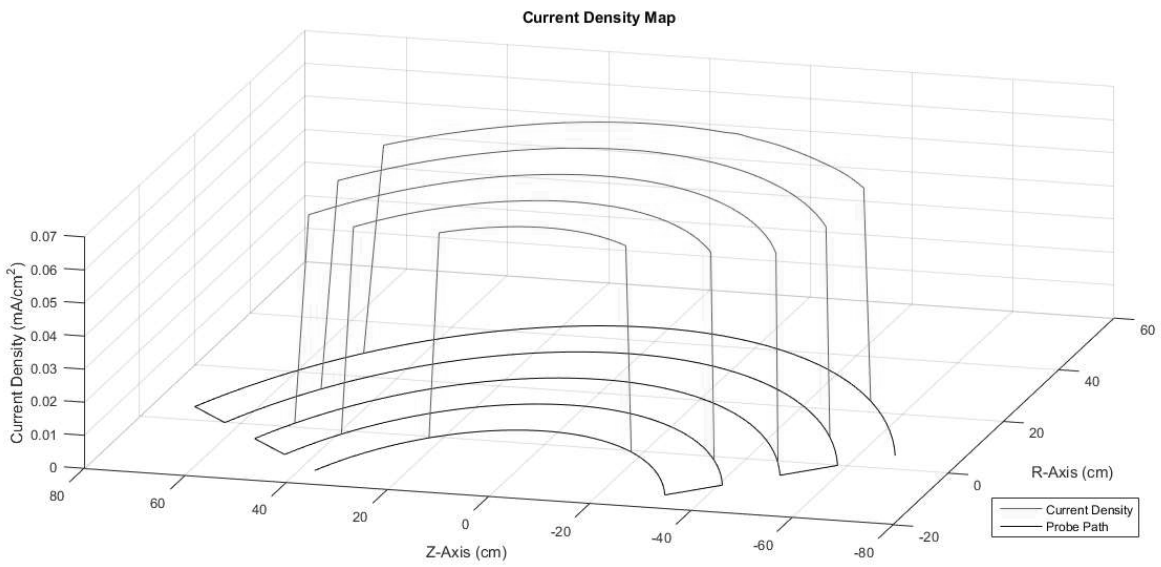

Figure 58. Calculated Radial Current Density Data 3D Plot

For a comparison to other Faraday probe current density data, Figure 59 shows data recorded from a 600W Hall thruster [26].

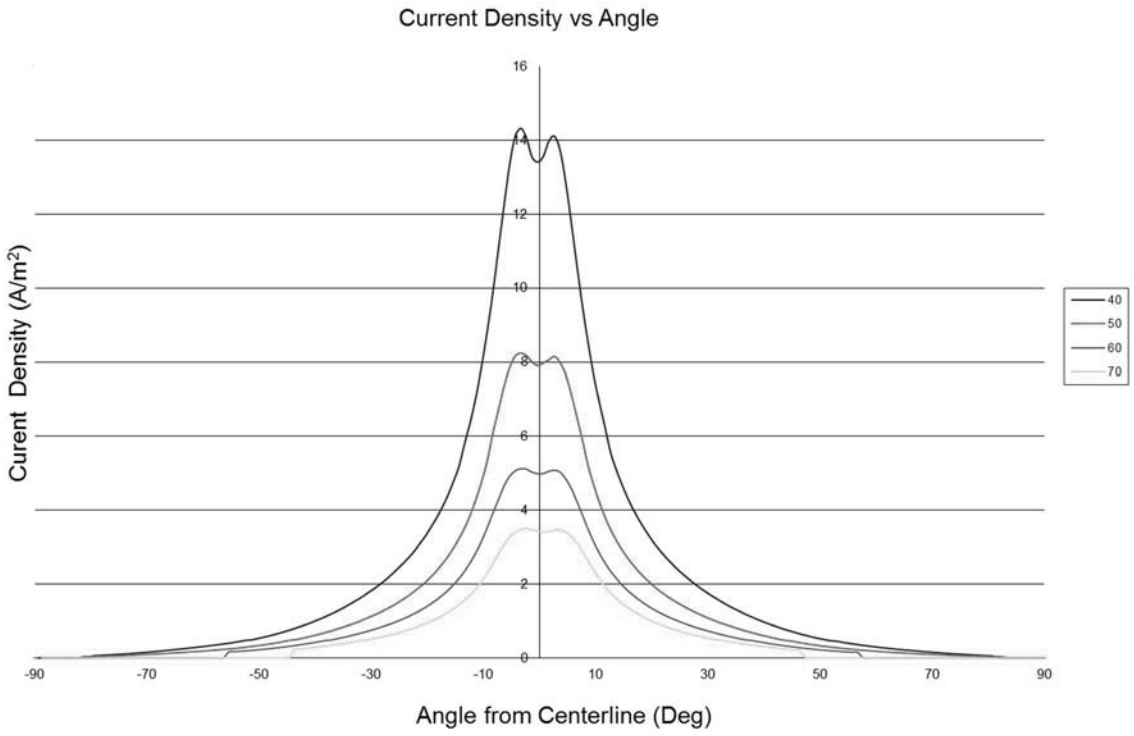

Figure 59. Calculated Radial Current Density Data for a 600W Hall Thruster

Figure 59 shows an expected approximately Gaussian distribution of data and a reduction of current density as the radius increases. These key aspects of Faraday probe data are not seen in the data recorded in this research. Overall, this means the data recorded is not directly the beam current density from the BIT-1 ion thruster and it is unknown what exactly was collected by the Faraday probe.

The data, despite not collecting the expected information, has distinct angle values located where the current density has a jump discontinuity. These angles can be compared to the divergence angle of the thrust plume. The values are shown below in Table 3.

Table 3. Faraday Probe Radius and Corresponding Angle

Radius (cm)	Angle (deg)
40	27.50
50	45.00
60	51.25
70	45.00
80	37.50

The angles appear to grow larger up to 60 cm away from the thruster, then start to reduce. These values can be explained by taking into account the reflection of particles. The further radii would allow the distance for reflected particles to impact other particles, thereby reducing the angle of recorded data. Due to not fully understand what type of data was recorded, the angles found can be distorted by particles reflecting off of any surface inside the chamber. Therefore, the most likely thrust angle would be the smallest angle and would probably decline as the Faraday probe records data closer to the thruster. However, as the data recorded does not contain current density information, no inferences can reliably concluded.

Thrust Stand Validation

To validate the thrust stand's equation and experimental setup for future projects, an experiment was performed. The thrust stand was setup with a small plastic pouch attached to the thruster mount location with a fishing line. The fishing line was placed around a small pipe just behind the thrust stand. This setup allowed for small weights with known masses to be easily placed inside. The displacement caused as each weight was added to the pouch was recorded. A picture of the setup is shown below in Figure 60.

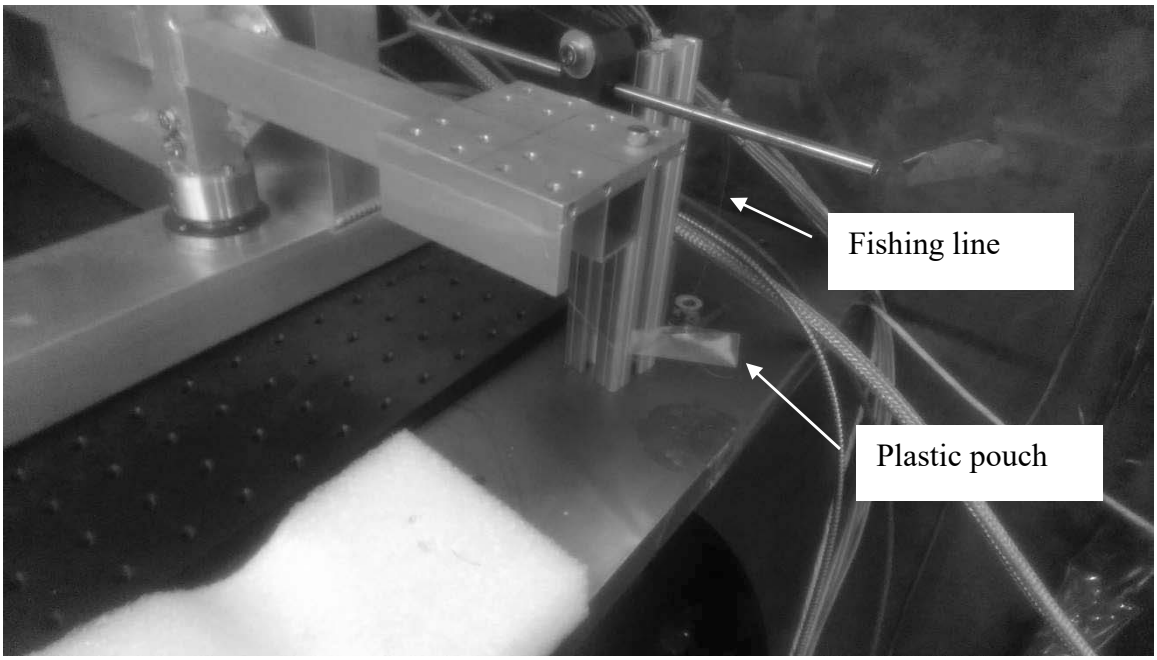

Figure 60. Thrust Stand Validation Experimental Setup

Before testing, the thrust stand was isolated from external air currents by closing one side of the vacuum chamber and applying a large plastic seal on the other. The experiment was started with a calibration test where 100, 200, and 300 volts were applied to the main detector plate. This imparted an electrostatic force between the detector plates, attracting the torsional stand to the main plate. Immediately after the voltage was removed and the thrust stand returned to the equilibrium location, the weights application test started. Three weights were added to the pouch in succession, allowing 5 to 10 seconds between applications for the thrust stand to damp to an equilibrium point. The displacement of the torsional stand was recorded through the calibration test and weights application test in one data set. The entire process was then repeated 3 times. The displacement data of each test is shown in Appendix B.

Using Equation 32, the force applied by each voltage was found using the voltage and distance data recorded for each of the calibrations tests. The force applied by each of the weights was found using the nominal value of Earth's gravity and the recorded mass of each weight. In addition, the distance of each applied force location was taken into account by finding the moment applied by each force about the axis of rotation. Figure 61 shows the comparison of the applied moment and the distance induced by the respective forces for the calibration test and the weights test.

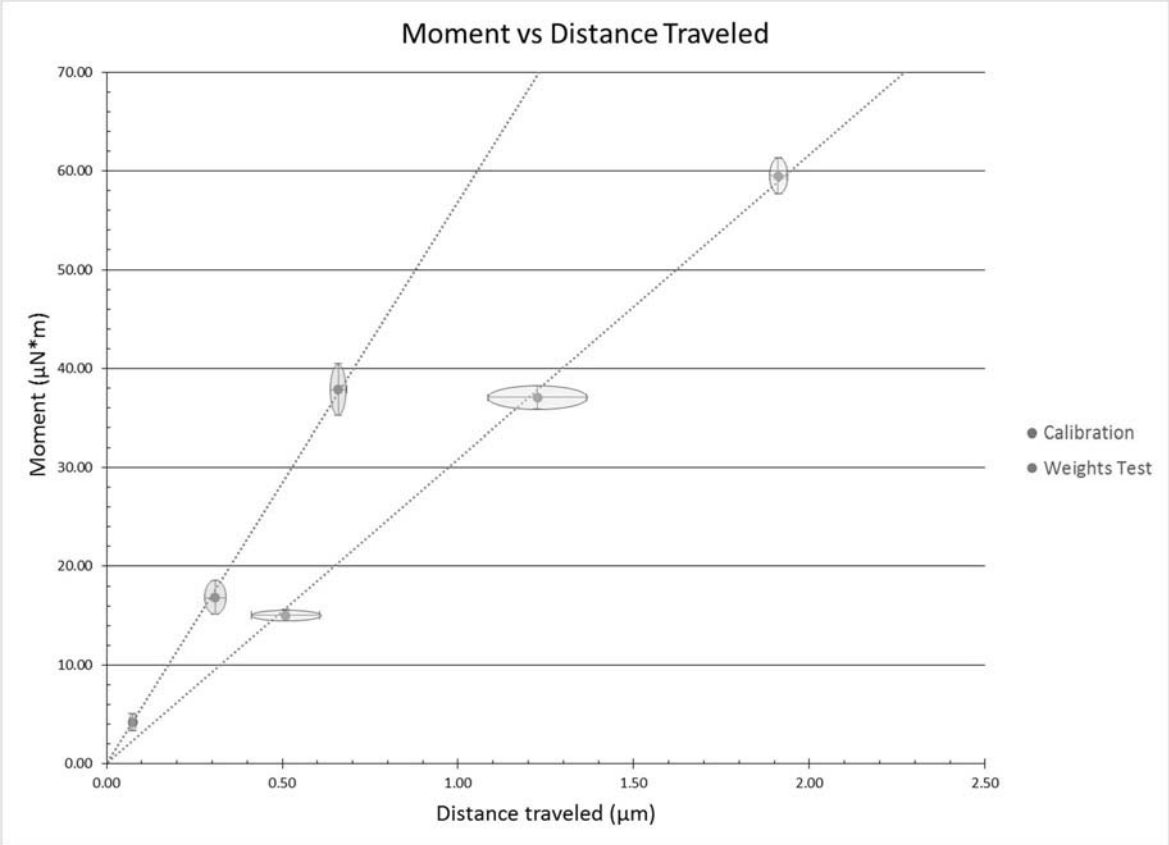

Figure 61. Moment vs Distance Traveled for Calibration and Weights Tests

As seen in the above figure, the ovals surrounding the points represents the standard deviation and error in data recorded and calculated. These errors were a combination of several errors including the input voltage, the mass of weights, the angle of the fishing line, the length of the moment arm, and standard deviation of displacement data. The error does not include measurement error from the laser displacement sensor because this verification required a secondary displacement sensor. Overall the trend lines added to the figure show a significant discontinuity between the weights test and the calibration equation. The calibration equation originated from Busek designed for a perfect factory built torsional thrust stand. Due to manufacturing defects, product age, and continued use, it is probable the original calibration equation requires adjustment.

Leveraging the data already recorded in this experiment, an adjusted calibration equation was developed. Equation 33 shows the new calibration equation.

$$F_{cal\_new} = 0.5415 * \frac{(1.262 * 10^{-9})(1 + 1.138.1 * \mathrm{d})V_{Cal}^2}{\mathrm{d}^2} \tag{33}$$

The only modification from the original equation was a multiplier value of 0.5415. This new equation results in values in line with the known mass force application. The forces due to the input voltage were re-calculated using the new equation. Figure 62, below, shows the graph of the moment versus distance traveled graph using the new equation.

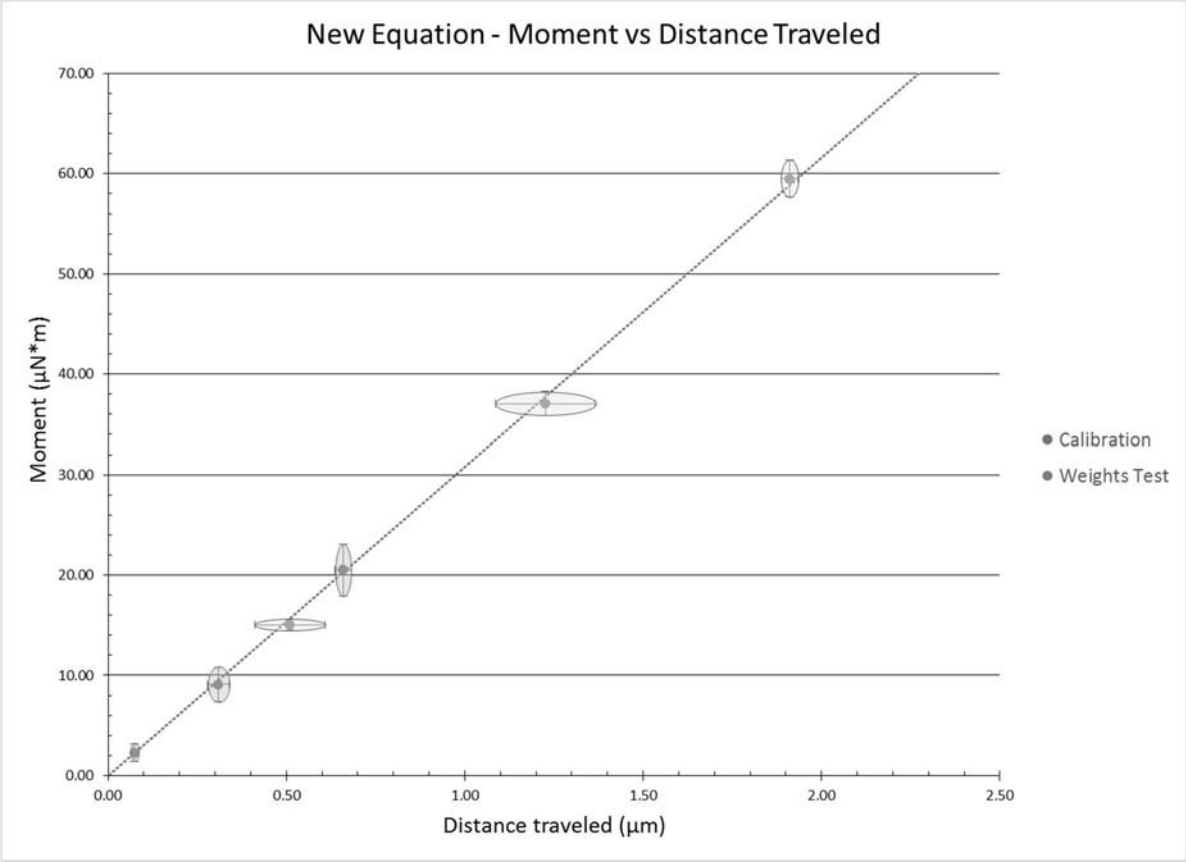

Figure 62. Moment Versus Distance Traveled for the Calibration and the Weights Tests Using the Modified Calibration Equation

As seen in Figure 62, the new equation allows the calibration data and the weights test data to match nearly perfectly. The real forces applied at each voltage were estimated to be 7.8 ± 2.8 μN, 31.1 ± 5.8 μN, and 70.1 ± 8.62 μN, respectively. Therefore, when this thrust stand is used in future experiments, the output forces from the voltages will be known resulting in more accurate thrust estimates to be calculated.

V. Conclusions and Recommendations

Conclusions of Research

As a result of the complications in testing, equipment malfunctions, and the initial state of the BIT-1 ion thruster, the research objectives were not met. The intent of this research was to fully characterize the BIT-1 ion thruster. First, using a Faraday probe, a map of the current density would be produced. This current map would be used to determine the divergence angle of the thrust plume and the total beam current. Next, using an ExB probe, the thruster's species distribution in the thrust plume was to be recorded. This would have provided the data to show the thrust's ionization efficiency. Lastly, and the most important objective of this research, was to record thrust data throughout the flight envelope using the Busek torsional thrust stand. This data would have provided the nominal operating conditions, the thrust range and the range of specific impulse throughout the operating conditions. Unfortunately, the thrust only operated for approximately 15 minutes through all the testing.

The only data which was successfully gathered using the Faraday probe was not the expected current density data. The data gathered did not have a Gaussian distribution nor a reduction of current density as the radius increased. Therefore, no inferences can reliably concluded.

Significance of Research

Despite none of the research objectives being meet and the thruster only operating 15 minutes, there were many lessons learned which can be passed on to future

researchers. In addition, several fundamental problems were overcome to allow for the operation of the BIT-1 ion thruster without the associated power-control tower and software from Busek in AFIT's vacuum chamber.

The first and most important conclusion which came from this research is the successful operation of the BIT-1 ion thruster for the first time at AFIT. Originally, this thruster was designed to be operated directly by the power-control tower and software. This in combination with the tower, the software allows the user to quickly and easily control the inputs to the thruster. Since the tower was damaged beyond repair in the previous experiment, the thruster operational requirements were met with several individual equipment components. Each component was independently controlled and adjusted through the testing process. The radio frequency generator often required adjustment to ensure the correct power level was supplied to the thruster. Once the thruster was repaired and insulated with silicone tape, the BIT-1 ion thruster was able to start and operate using the individual equipment components. Also, through this process, a basic starting procedure was created for the BIT-1 ion thruster without the Busek controller.

The second lesson learned through this experiment is regarding the length and diameter of the propellant tube. Through the troubleshooting process, it was theorized the BIT-1 thruster was not receiving the 0.08 sccm of propellant provided by the flow controller. With the exception of locations internal to the BIT-1, the entire propellant line was inspected for leaks. Positions where leaks were likely, small amounts of high vacuum silicone grease were applied as a preventative measure. However, at the end of the experiment, it was concluded there still had to be a leak somewhere in the system. At

this time, Tsay was contacted for information on Busek's BIT-1 experimental setup for the propellant tube. Tsay stated in Busek's experiment they typically use 5-ft of 1/8 inch diameter tubing on both the inside and outside of their vacuum chamber [25]. This results in about 1.47 cubic inches of tubing for the propellant to pass through. In this experiment, the shortest and last redesigned setup used about 8 feet of 1/4 inch tubing and 1 foot of 1/8 inch tubing. This results in about 4.86 cubic inches of tubing or more than 3 times the volume of Busek's propellant line. In addition, the large propellant line required several adapters to step down the diameter to the near 1mm propellant line on the BIT-1. Therefore, the large disparity in the propellant line volume may have contributed to the BIT-1 operational difficulties at AFIT.

Third, the importance of the hollow cathode's distance from the thruster was determined. Initially in the experiment, the BIT-1 was setup with the hollow cathode about 5 inches away. This setup did not work and did not provide enough seed electrons to start the plasma generation. Through discussion with Tsay, a minimum of 1 mA is required to start the plasma generation [25]. Subsequently, the experimental setup was redesigned with the hollow cathode about 1 inch away. This setup was successful and reached 1.6 mA during the polarity switch. In the last experimental setup on the thrust stand, more difficulty arose with the distance between the hollow cathode and the thruster. Again, when the hollow cathode was positioned close enough to the thruster, the required current to start the plasma generation was meet. Overall, it was found the hollow cathode is required to be inside a 2-inch radius and pointed at the BIT-1 thruster to ensure seed electrons are collected to start the plasma generation.

Finally, the thrust stand verification test showed the flaw of the original force equation. The equation provided by Busek was based off perfect factory manufactured thrust stand. Due to any manufacturing defects, product age, and the continued use of AFIT's torsional thrust stand, the equation did not match real data. A modification was added to the thrust stand's equation resulting in the data matching nearly perfectly to the real data. This change allowed the calibration forces applied to be found resulting in more accurate thrust estimates to be calculated in the future.

Recommendations for Future Research

Since this research did not result in any of the desired research objectives, it is suggested this research is attempted again. There were several significant issues which arose during the testing process which can be addressed before the start of future testing.

For future projects using this BIT-1, re-purchase and incorporate the BIT-1's associated power-control tower and software into the testing. Though this research has proved it is possible to operate the BIT-1 using several independently controlled devices, each device adds error to the measured data. The ability to control each input to the BIT-1 through a single user interface, with all the data located it one place is very important for error reduction. In addition, the BIT-1 software automatically adjusts the radio frequency generator's frequency and amplification allowing for a constant power output with the smallest reflected power.

During the thrust stand verification and attempting to record the BIT-1 thrust data, there were large oscillations present in the displacement data. The laser displacement sensor is extremely sensitive and continuously measures the displacement. Therefore any

vibrational input affects the data. The largest vibrational input was the vacuum chamber's cryogenic pumps. Additionally, vibrations from other sources were notable, such as nearby electric equipment and even closing doors. For future projects using this thrust stand, vibrational isolation should be used to reduce the outside effects on the thrust stand data collection. Once the thrust stand has been isolated from vibration, the torsional thrust stand verification should be accomplished again to validate the new equation developed for the Busek torsional thrust stand.

For the final recommendation, if possible, the thruster should be replaced with a newer model of the BIT-1 ion thruster. The newer models encompass different methods of starting the thruster without the use of an additional, very large, hollow cathode. The newer model will also allow for easy data collection on the thrust stand by reducing the required infrastructure.

Summary

The Busek 1cm radio frequency ion thruster tested in this experiment had several significant challenges to overcome in order to operate the thruster inside AFIT's vacuum chamber. Due to these challenges the BIT-1 was successfully operated for a total of 15 minutes, though no experimental thrust or species ionization data was recorded. Further testing is required to gather official thrust, divergence angle, and thruster efficiency. In addition, the Busek torsional thrust stand's calibration equation was evaluated. The calibration equation was found to overestimate applied forces. A modification was added to the thrust stand's equation resulting in calibration forces matching nearly perfectly to the real forces. This change resulted in more accurate thrust estimates to be calculated in

future experiments. The results from the research were inconclusive on whether thrusters of this size have potential in future micro-satellite missions. However, through the troubleshooting steps and the lessons learned, following researchers will be able to gather data quickly and easily on this BIT-1 ion thruster.

Appendix A. Faraday Probe Data

The results of the second Faraday probe data gathered is shown below. This data, similar to the first data set, shows constant current density values. This is not the expected Gaussian distribution of data and does not decrease in magnitude as the radius increases.

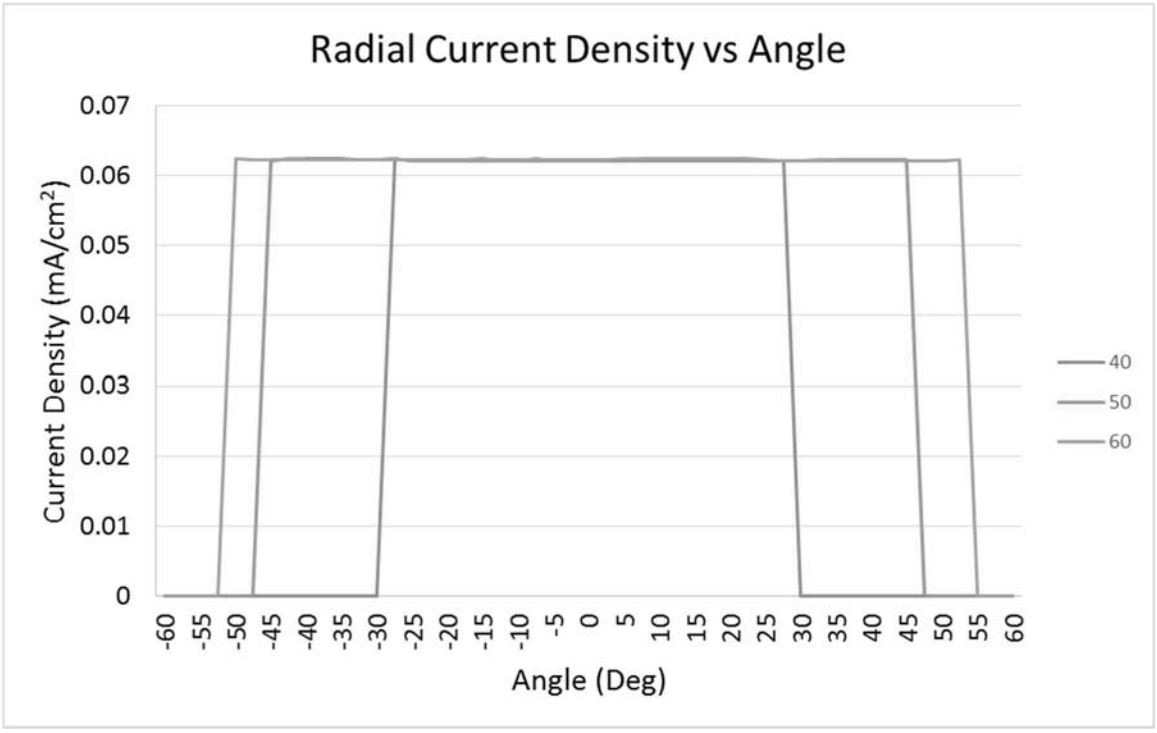

Figure 63. Calculated Radial Current Density Data

Appendix B. Torsional Thrust stand Calibration Data

The data recorded from the laser displacement sensor through the testing of the applied calibration voltages and weights test are shown below. The first set of oscillations is the result of the applied voltages in steps of 100 from 0 to 300 volts. The next set of oscillations is the application of the weights. Calibration test 4 is missing the last application of the final weight which is a results of dropping the final weight inside the vacuum chamber.

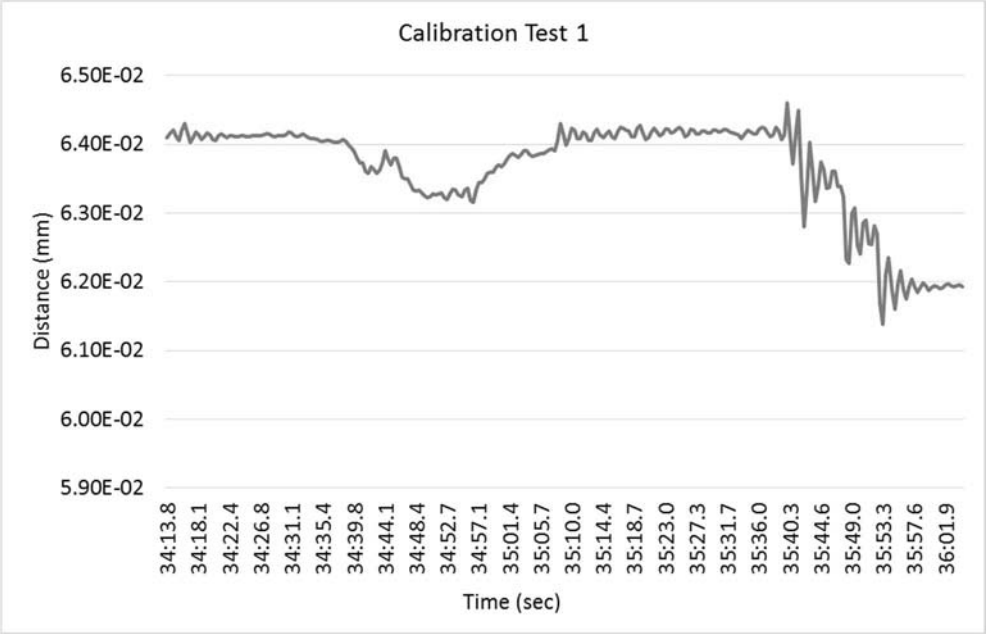

Figure 64. Calibration Test One

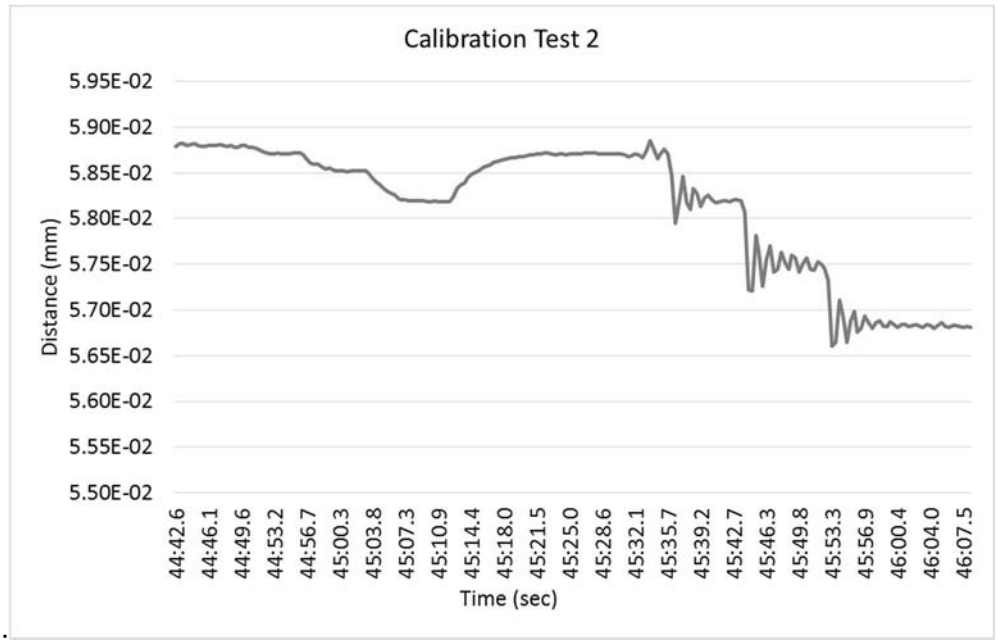

Figure 65. Calibration Test Two

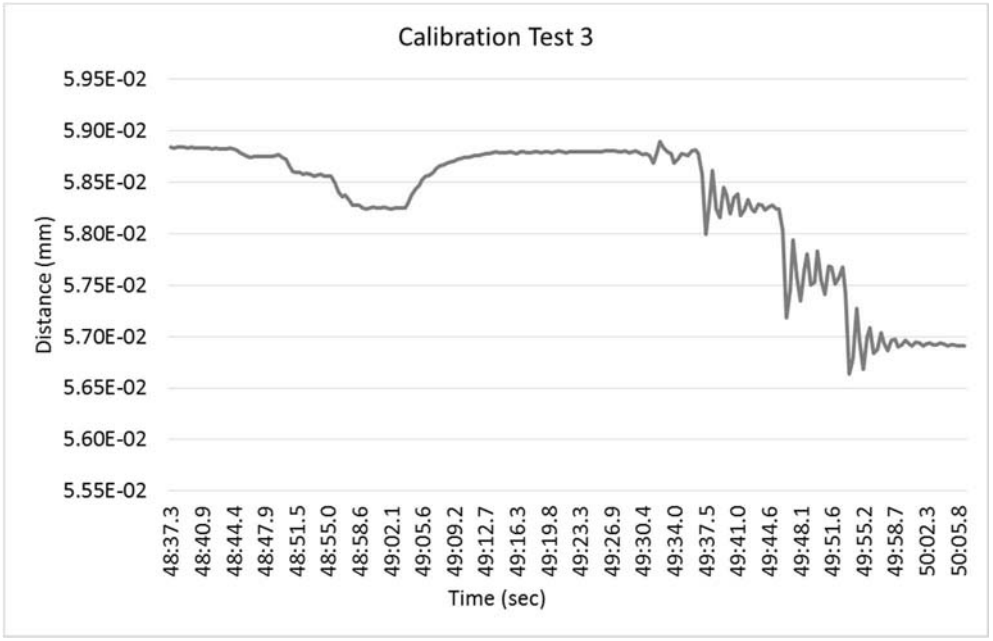

Figure 66. Calibration Test Three

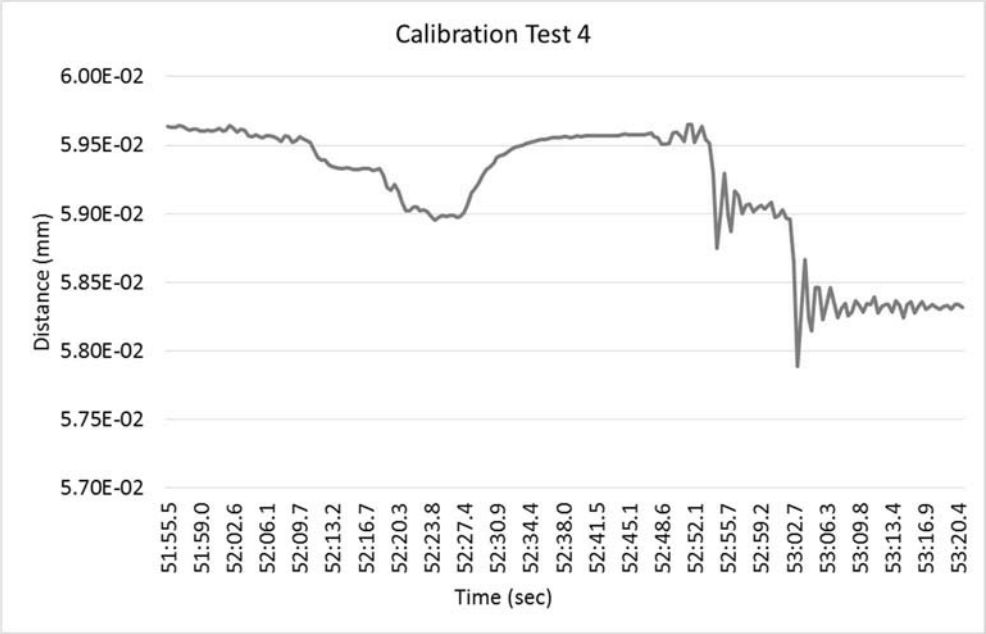

Figure 67. Calibration Test Four

Bibliography

[1] D. M. Goebel and I. Katz, *Fundamentals of Electric Propulsion: Ion and Hall Thrusters*. 2008.

[2] NASA, "Glenn Contributions to Deep Space 1," 21-May-2008. [Online]. Available: http://www.nasa.gov/centers/glenn/about/history/ds1.html. [Accessed: 03-May-2016].

[3] National Aeronautics and and Space Administration, "Ion Propulsion," 2016. [Online]. Available: http://www.nasa.gov/sites/default/files/atoms/files/ionpropfact_sheet_ps-01628.pdf. [Accessed: 14-Jul-2016].

[4] V. Khayms, "Advanced Propulsion for Microsatellites," Massachusetts Institute of Technology, 2000.

[5] M. Tsay, K. Hohman, N. Rosenblad, E. Ehrbar, M. Robin, and C. Farnell, "Micro Radio-Frequency Ion Propulsion System," in *48th AIAA/ASME/SAE/ASEE Joint Propulsion Conference & Exhibit*, 2012.

[6] C. L. Muilenburg, "Emperical Determination of Performance Characteristics For Busek 1CM Micro Radio-Frequency Ion Propulsion System," Air Force Institute of Technology, 2016.

[7] R. G. Jahn and E. Y. Choueiri, "Electric Propulsion," *Encycl. Phys. Sci. Technol.*, vol. 5, pp. 125–141, 2002.

[8] A. Shabshelowitz, "Study of RF Plasma Technology Applied to Air-Breathing Electric Propulsion," University of Michigan, 2013.

[9] H. Kuninaka and S. Satori, "Development and Demonstration of a Cathodeless Electron Cyclotron Resonance Ion Thruster," *J. Propuls. Power*, vol. 14, no. 6, pp. 1022–1026, Nov. 1998.

[10] M. M. Tsay and M. Martinez-sanchez, "Two-Dimensional Numerical Modeling of Radio-Frequency Ion," Massachusetts Institute of Technology, 2010.

[11] S. Nguyen, "Design of an EXB Probe," 2004. [Online]. Available: http://ntrs.nasa.gov/archive/nasa/casi.ntrs.nasa.gov/20050186785.pdf. [Accessed: 14-Jul-2016].

[12] D. J. Warner, "ADVANCED CATHODES FOR NEXT GENERATION ELECTRIC PROPULSION TECHNOLOGY," Air Force Institute of Technology, 2008.

[13] University of Michigan: Department of Aerospace Engineering, "Plasma

Diagnostics: Faraday Probe," 2010. [Online]. Available: http://pepl.engin.umich.edu/diagnostics/Faraday.html. [Accessed: 10-Oct-2016].

[14] M. L. R. Walker, R. R. Hofer, and A. D. Gallimore, "The Effects of Nude Faraday Probe Design and Vacuum Facility Backpressure on the Measured Ion Current Density Profile of Hall Thruster Plumes," *38th Annu. AIAA Jet Proplusion Conf.*, no. July, pp. 1–13, 2002.

[15] H. Jethani, "Electric Propulsion - Thruster Geometry," *The Colorado Center for Astrodynamics Research*, 2014. [Online]. Available: http://ccar.colorado.edu/asen5050/projects/projects_2014/Jethani_Henna/Thruster_Geometry.html. [Accessed: 15-Oct-2016].

[16] G. Bocharov and A. Eletskii, "Theory of Carbon Nanotube (CNT)-Based Electron Field Emitters," *Nanomaterials*, vol. 3, no. 3, pp. 393–442, 2013.

[17] Y. Ohkawa, K. Matsumoto, and S. Kitamura, "Field Emission Cathodes using Carbon Nanotubes," Japaon Aerospace Exploration Agency, 21st Microelectronics Workshop, Tsukuba Japan, Oct. 2008.

[18] Omega Engineering Inc., "FMA-2600A Series Mass Flow Controllers." [Online]. Available: https://www.omega.com/manuals/manualpdf/M3791.pdf.

[19] D. Frisby, *Personal Communications*. Omega, 2016. [Communicated: 20-Dec-2016]

[20] Busek Co. Inc., "Busek Hollow Cathode," 2013. [Online]. Available: http://www.busek.com/index_htm_files/70008509B.pdf.

[21] M. M. Tsay, "User Manual for Busek 1cm FR Ion Thruster BIT-1 System," Busek Co. Inc., Feb 2015.

[22] C. Farnell and J. D. Williams, "Faraday Probe Operating Manual," Ft. Collins.

[23] C. Farnell and J. D. Williams, "ExB Probe Operating Manual." Ft. Collins.

[24] Alicat Scientific Inc., "Changing valve position on any small valve Alicat controller," 2012. [Online]. Available: https://www.youtube.com/watch?v=giNALEDHej4. [Accessed: 20-Dec-2016].

[25] M. Tsay, *Personal Communications*. Busek Co. Inc., 2016. [Communicated: 22-Dec-2016]

[26] D. M. Bui, "Plume Characterization of Busek 600W Hall Thruster," Air Force Institute of Technology, 2005.

REPORT DOCUMENTATION PAGE

Form Approved
OMB No. 074-0188

1. REPORT DATE *(DD-MM-YYYY)*	2. REPORT TYPE	3. DATES COVERED *(From – To)*
22-03-2017	Master's Thesis	August 2015 – March 2017

TITLE AND SUBTITLE

Busek 1CM Micro Radio-Frequency Ion Thruster Empirical Performance Determination

5a. CONTRACT NUMBER

5b. GRANT NUMBER

5c. PROGRAM ELEMENT NUMBER

6. AUTHOR(S)

Couch, Brian D., Captain, USAF

5d. PROJECT NUMBER

5e. TASK NUMBER

5f. WORK UNIT NUMBER

7. PERFORMING ORGANIZATION NAMES(S) AND ADDRESS(S)

Air Force Institute of Technology
Graduate School of Engineering and Management (AFIT/ENY)
2950 Hobson Way, Building 640
Wright-Patterson AFB OH 45433-7765

8. PERFORMING ORGANIZATION REPORT NUMBER

AFIT-ENY-MS-17-M-253

9. SPONSORING/MONITORING AGENCY NAME(S) AND ADDRESS(ES)

Intentionally left blank

10. SPONSOR/MONITOR'S ACRONYM(S)

11. SPONSOR/MONITOR'S REPORT NUMBER(S)

12. DISTRIBUTION/AVAILABILITY STATEMENT

DISTRUBTION STATEMENT A. APPROVED FOR PUBLIC RELEASE; DISTRIBUTION UNLIMITED.

13. SUPPLEMENTARY NOTES

14. ABSTRACT

Empirical performance quantification was attempted on a Busek 1-centimeter Radio Frequency Ion Thruster (BIT-1) to characterize thruster performance across a full range of operating conditions. Several experimental setups were attempted in order to operate the specific thruster utilized for this experiment. All troubleshooting steps are documented leading up to successful operation of the BIT-1 for a total of 15 minutes. Further testing is required to fully quantify the BIT-1 thrust profile, exact divergence angle, and efficiency. In addition, the Busek torsional thrust stand's calibration force equation was evaluated. The current calibration equation was found to overestimate applied forces. A modification was added to the thrust stand's equation enabling more precise thrust measurements for future experiments.

15. SUBJECT TERMS

Radio Frequency Ion Thruster, Performance Determination

16. SECURITY CLASSIFICATION OF:			17. LIMITATION OF ABSTRACT	18. NUMBER OF PAGES	19a. NAME OF RESPONSIBLE PERSON
a. REPORT	b. ABSTRACT	c. THIS PAGE			Carl Hartsfield, AFIT/ENY
U	U	U	UU	125	19b. TELEPHONE NUMBER *(Include area code)* (937) 255-6565, ext 4667 Carl.Hartsfield@afit.edu

Standard Form 298 (Rev. 8-98)
Prescribed by ANSI Std. Z39-18